

Influence of Microstructure on Susceptibility to Weld Defects in Two High Strength Low Alloy Steels

by

Amir Keyvan EDALAT NOBARZAD

THESIS PRESENTED TO ÉCOLE DE TECHNOLOGIE SUPÉRIEURE
IN PARTIAL FULFILLMENT FOR A MASTER'S DEGREE WITH THESIS IN
MECHANICAL ENGINEERING
M.A.Sc.

MONTREAL, JULY 14th, 2017

ÉCOLE DE TECHNOLOGIE SUPÉRIEURE
UNIVERSITÉ DU QUÉBEC



Amir Keyvan Edalat Nobarzad, 2017



This Creative Commons licence allows readers to download this work and share it with others as long as the author is credited. The content of this work can't be modified in any way or used commercially.

BOARD OF EXAMINERS

THIS THESIS HAS BEEN EVALUATED

BY THE FOLLOWING BOARD OF EXAMINERS

Mr. Mohammad Jahazi, Thesis Supervisor
Department of mechanical engineering, École de technologie supérieure

Mr. Henri Champlaud, President of the Board of Examiners
Department of mechanical engineering, École de technologie supérieure

Mr. Than Pham, Member of the jury
Department of mechanical engineering, École de technologie supérieure

THIS THESIS WAS PRESENTED AND DEFENDED

IN THE PRESENCE OF A BOARD OF EXAMINERS AND PUBLIC

JUNE 21ST, 2017

AT ÉCOLE DE TECHNOLOGIE SUPÉRIEUR

ACKNOWLEDGMENT

I would like to take this opportunity to thank my supervisor, Professor Mohammad Jahazi for his full support, insightful advises and professional manner during my research project.

I take this opportunity to thank Mr. Alexandre Szymanski for all helps and support and providing useful comments during this research. I would like to thank also Mr. Gil Trigo for his useful advises.

I would like to acknowledge the endless support of my friends at ÉTS, specially Mr. Mohammad Saadati, Mr. Hadi Ghassemi, Mr. Hossein Monajati, Mr. Mahdi Massoumi Khalilabad, Mr. Abdelhalim Loucif, Mr. Samir Mourad Chentouf, Mr. Yasser Zidan, Mr. Heitham Touazine and Mr. Mario Corbin.

Finally, I would like to thank my lovely family. My wife, Ms. Shiva Moradi and my son, Alan Edalat Nobarzad without whom I would never finish this thesis.

L'INFLUENCE DE LA MICROSTRUCTURE SUR LA SUSCEPTIBILITÉ AUX DÉFAUTS DE SOUDAGE DANS DEUX ACIERS FAIBLEMENT ALLIÉS À HAUTE RÉSISTANCE MÉCANIQUE

Amir Keyvan EDALAT NOBARZAD

RÉSUMÉ

Les causes de fissuration à chaud dans les aciers faiblement alliés à haute résistance mécanique (HSLA) ont été étudiées et des solutions sont proposées. Les échantillons ont été soudés selon une configuration en T conservant les paramètres de soudage constants pour les métaux de base Gr.50 et Gr.80. Des études métallographiques ont été réalisées à l'aide de microscope optique et électronique. Les métaux de base, la soudure et la zone affectée thermiquement (HAZ) sont caractérisés et expliqués. Des changements chimiques locaux dans l'axe central de la soudure ont également été étudiés par analyse dispersive en énergie (EDS). Toutes les soudures de Gr.80 indiquent la fissuration à chaud dans l'axe central de la soudure, alors qu'aucune des soudures Gr.50 n'a été fissurée. Ceci peut être expliqué par l'effet de verrouillage des bras dendritiques secondaires (SDA) dans les métaux de base Gr.50 qui améliore la résistance de l'axe central de la soudure à la fissuration à chaud. Le SDA long est attribué à la plus grande taille des grains dans HAZ de Gr.50 comparativement à la taille de grain du Gr.80. Plus grande sera la largeur du bras dendritique primaire (PDA), plus un SDA sera long. Les SDA long peuvent se verrouiller facilement, ce qui améliore la résistance de l'axe central de la soudure contre la fissuration. Une forte contrainte résiduelle dans le métal de base Gr.80 est également détectée comme facteur contributif. L'existence d'inclusions nonmétalliques englobées par des porosités de gaz peut aussi faciliter la propagation des fissures. Enfin, des mesures correctives et préventives ont été suggérées pour éviter la formation de fissures à chaud.

Mots-clés : défaut de soudure, fissuration à chaud, fissuration lors de la solidification, HSLA, GMAW.

INFLUENCE OF MICROSTRUCTURE ON SUSCEPTIBILITY TO WELD DEFECTS IN TWO HIGH STRENGTH LOW ALLOY STEELS

Amir Keyvan EDALAT NOBARZAD

ABSTRACT

Hot cracking root causes in two HSLA welded steels were investigated and remedies were proposed to avoid hot cracking at centerline of the weld. The specimens were welded in T-joint configuration keeping the constant welding parameters for both investigated alloys: Gr.50 (with lower content of alloying elements and yield strength of 345 MPa) and Gr.80 (with higher content of alloying elements and yield strength of 550 MPa). Metallographic studies were performed using optical and electron microscopy. Base metal, weld and HAZ were all characterized and discussed. Local chemical changes in centerline of the weld were also investigated with Energy Dispersive X-ray spectroscopy (EDS). All welds of Gr.80 showed hot cracking at the centerline while none of the Gr.50 welds were cracked. This can be explained by interlocking effect of secondary dendrite arms (SDA) in Gr.50 welds which enhances the resistance of weld centerline to hot cracking. Longer SDA is attributed to larger size of grains in HAZ of Gr.50 compared to grain size in Gr.80. The larger is the grain size of HAZ, the larger will be the width of primary dendrite arm (PDA) which in turn induces longer SDA. High residual stresses in Gr.80 base metal are also detected as a contributing factor. Existence of nonmetallic inclusions engulfed by gas porosities can also ease the crack propagation. Finally remedies and preventive action have been suggested to avoid formation of hot cracks.

Keywords: weld defect, hot cracking, solidification cracking, HSLA, GMAW

TABLE OF CONTENTS

Page

INTRODUCTION	1
CHAPTER 1 LITERATURE REVIEW	3
1.1 HSLA steels	3
1.1.1 Microstructure of weld metal	9
1.1.2 Microstructure of heat affected zone	16
1.2 Weld defects.....	18
1.2.1 Cold cracking	18
1.2.2 Hot cracking	19
CHAPTER 2 MATERIALS AND METHODS	41
2.1 Base metals	41
2.1.1 ASTM A572 Gr.50.....	41
2.1.2 ASTM A656 Gr.80.....	42
2.2 Filler metals	42
2.2.1 ESAB S-6 (low nickel for both Gr.50 and Gr.80).....	43
2.2.2 Hobart Fabcor E80C-Ni1 H8 (medium nickel for Gr.50).....	44
2.2.3 Selectarc 80C Ni2 (high nickel for Gr.50)	45
2.2.4 BLUSHIELD LA 100C MG (medium nickel for Gr.80).....	45
2.2.5 Hobart Fabcor 80C-N2 (High nickel for Gr.80).....	46
2.3 Welding process.....	47
CHAPTER 3 RESULTS AND DISCUSSION.....	49
3.1 Characterization of the base metals	49
3.1.1 ASTM A572 Gr.50.....	49
3.1.2 ASTM A656 Gr.80.....	51
3.1.3 Physical properties	55
3.2 Welding of specimens.....	57
3.3 Characterization of the weld metal	59
3.3.1 Macroscopic studies on phase A welds	59
3.3.2 Macroscopic studies on phase B welds	64
3.3.3 Chemical composition.....	74
3.3.4 Microstructural studies on weld metal	77
3.3.5 Local chemical changes at centerline of the weld.....	90
3.4 Effect of heat affected zone on hot cracking	95
3.5 Remedies and preventive actions.....	105
CONCLUSION.....	111
RECOMMENDATIONS.....	113

LIST OF BIBLIOGRAPHICAL REFERENCES.....116

LIST OF TABLES

	Page
Table 1.1 A partial list of HSLA steels (ASTM classification).....	8
Table 1.2 Effect of chemical composition of inclusions on their potential for AF nucleation.	14
Table 1.3 Effect of alloying elements on acicular ferrite nucleation.....	15
Table 2.1 Mechanical properties of ASTM A572 Gr.50 [8].....	41
Table 2.2 Chemical composition of ASTM A572 Gr.50 (wt%).....	41
Table 2.3 Mechanical properties of ASTM A656 Gr. 80 [56].....	42
Table 2.4 Chemical composition of ASTM A656 Gr.80 (wt%).....	42
Table 2.5 Filler metals used for Gr.50 and Gr.80.	43
Table 2.6 Chemical composition of non-diluted weld for filler metal ESAB S-6 (wt%).....	43
Table 2.7 Mechanical properties of weld for ESAB S-6 welded using 75% Ar - 25% CO ₂	44
Table 2.8 Chemical composition of non-diluted weld for Hobart Fabcor E80C-Ni1 H8 (medium nickel for Gr.50) (wt%).	44
Table 2.9 Mechanical properties of weld for Hobart Fabcor E80C-Ni1 H8 welded using 95% Ar - 5% CO ₂	44
Table 2.10 Chemical composition of non-diluted weld for Selectarc 80CNi2 (wt%).....	45
Table 2.11 Mechanical properties of weld for selectarc 80C Ni2.	45
Table 2.12 Chemical composition of non-diluted weld for BLUSHIELD LA 100C MG (wt%).....	46
Table 2.13 Mechanical properties of weld for BLUSHIELD LA 100C MG.	46
Table 2.14 Chemical composition of non-diluted weld for Hobart Fabcor 80C-N2 (wt%).....	46

Table 2.15	Mechanical properties of weld for BLUSHIELD LA 100C MG.	47
Table 3.1	Welding parameters for phase A workpieces prepared by the industrial party.	58
Table 3.2	Welding parameters for phase B workpieces.	59
Table 3.3	Comparison of chemical composition of base, filler metal and weld for Gr.50 welds phase B (wt%).	75
Table 3.4	Comparison of chemical composition of base, filler metal and weld for Gr.80 welds phase B (wt%).	76
Table 3.5	Carbon equivalent calculations based on weld metals chemical compositions.	77
Table 3.6	Ni and Mo content in weld metals.	90
Table 3.7	Probability-impact matrix for weld cracking.	108
Table 3.8	Hot cracking root cause analysis. Remedies are categorized in two groups: Design related remedies (D) and Process related remedies (P).	109

LIST OF FIGURES

	Page
Figure 1.1 Microstructure of as rolled HSLA steel with equiaxed ferrite grains (white area) and pearlite bands (dark area).	4
Figure 1.2 Complex carbonitrides in Nb-Ti HSLA steel.....	5
Figure 1.3 Solution of carbides, nitrides and carbonitrides in austenite.....	5
Figure 1.4 Precipitation strengthening as a function of cooling rate in a HSLA steel with 0.15 wt% of Vanadium.....	6
Figure 1.5 Different morphologies for primary ferrite in HSLA X70 weld metal; a) continuous GBF nucleated from austenite grain boundary, b) allotriomorphic primary ferrite nucleated on austenite grain boundary, c) idiomorphic primary ferrite nucleated from nonmetallic inclusions, d) intragranular primary ferrite nucleated inside the austenite grain.	10
Figure 1.6 Different morphologies for Widmanstätten ferrite in HSLA X70 weld metal; a) primary Widmanstätten ferrite nucleated from austenite grain boundaries, b) secondary Widmanstätten ferrite nucleated from GBF, c) primary Widmanstätten ferrite nucleated from nonmetallic inclusion, d) intragranular Widmanstätten ferrite nucleated from idiomorphic ferrite.....	11
Figure 1.7 Acicular ferrite with high angle boundaries differentiated from other ferrite morphologies using EBSD.....	12
Figure 1.8 Different bainite morphologies in HSLA X70 weld metal; a) upper bainite with parallel ferrite and cementite layers, b) lower bainite with cementite distributed in ferrite lathes.....	12
Figure 1.9 TEM image of an inclusion which acicular ferrite nucleated on.....	13
Figure 1.10 Prediction of weld toughness at -40°C as a function of Ni and Mn content.	15
Figure 1.11 Microstructure of various HAZ sections in GMAW welded HSLA-100 steel a) 0.01 mm, b) 0.1 mm, c) 0.3 mm, d) 0.7 mm from fusion line.	17
Figure 1.12 Bainite packets in HAZ of a HSLA steel.	17
Figure 1.13 Commonly observed positions of cold cracking.	18

XVIII

Figure 1.14 Variation of hydrogen absorption in weld pool.....19

Figure 1.15 Restrain resulting from weld configuration Taken from Kou (2003, p.285).21

Figure 1.16 Residual stress distribution along X direction resulted from FEM analysis.22

Figure 1.17 Factors influencing stress concentration at weld centerline.....23

Figure 1.18 Comparison of the path of a cleavage crack in Widmanstätten ferrite and acicular ferrite.24

Figure 1.19 Microsegregation of Ti-riched phases in crack path in weld repair of a cast steel, a) crack path, b) EDS map for Ti.....25

Figure 1.20 Effect of surface tension on wet grain boundaries; a) comparison of angle between liquid and grain boundary in high, medium and low surface tension, b) effect of surface tension on formation of liquid film at grain boundary.....26

Figure 1.21 Base metal dilution in weld pool.....27

Figure 1.22 Schematic illustration of weld face for similar H, a) high speed and high Q, b) low speed and low Q.....28

Figure 1.23 Effect of temperature gradient and growth rate on solidification pattern.29

Figure 1.24 Schematic illustration of dendrites growth as a function of solidification time.....30

Figure 1.25 Examples of penetration measurement on T-joint welds31

Figure 1.26 Schematic illustration of susceptibility to hot cracking in high ratio of D/W....31

Figure 1.27 Schematic illustration of the technological strength theory.33

Figure 1.28 Schematic illustration of the rate of feeding-shrinkage theory.34

Figure 1.29 Schematic of hot cracking explained by Rappaz-Drezet theory.35

Figure 1.30 Effect of Mn/S ratio combined with effect of carbon in welding of carbon steels.....36

Figure 1.31 Susceptibility to hot cracking for different weld patterns a) tear-shaped weld pool with perpendicular dendrites, b) oval shaped weld pool with non perpendicular dendrites, c) equiaxed grains at centerline of the weld and d) effect of arc oscillation in crack propagation at centerline of the weld38

Figure 1.32 Effect of weld face geometry on stress concentration.....39

Figure 2.1	Gas Metal Arc Welding; a) overall process; b) enlarged welding area.....	48
Figure 3.1	Optical microstructure of as received ASTM A572 Gr.50; a) equiaxed ferrite coexisting with pearlitic bands (hot etched), b) complex carbonitride particle (as polished).	50
Figure 3.2	Thermodynamic calculation for equilibrium phases in Gr.50 base metal.	50
Figure 3.3	Thermodynamic calculation for equilibrium phases in Gr.50 base metal in high magnification to reveal low content phases.	51
Figure 3.4	Microstructure of Gr.80 base metal; a) ferrite grains with complex carbonitrides , b) SEM image of a complex carbonitride (hot etched).	52
Figure 3.5	EDS analysis on complex carbonitrides of Gr.80 base metal.	53
Figure 3.6	Thermodynamic calculation for equilibrium phases in Gr.80 base metal.	54
Figure 3.7	Thermodynamic calculation for Equilibrium phases in Gr.80 base metal in high magnification to reveal low content phases.	55
Figure 3.8	Calculation of base metals physical properties; a) linear expansion coefficient, b) thermal conductivity	56
Figure 3.9	Weld configuration for phase B, All dimensions are in mm.	58
Figure 3.10	Examples of macrographic observations in phase A; a) macrocracking in a Gr.80 back plate weld (specimen: BK2-1), b) macrocracking in a Gr.80 single bevel weld (specimen: L6), c) lack of penetration in a Gr.80 single bevel weld (specimen: L43) and d) centerline in a Gr.50 single bevel weld with no macrocracking (specimen: RC5), all specimens are hot etched.....	61
Figure 3.11	Schematic of relation between weld penetration and heat transfer directions resulted from welding angle. Heat transfer direction is illustrated by small arrows and welding angle is illustrated by big arrows; a) low penetration resulted from 45° welding angle, b) excessive penetration resulted from deviation in welding angle from 45°	62
Figure 3.12	Constitutive magnification of equiaxed grains at weld face form a to d (specimen: BK2-2, hot etched).....	63
Figure 3.13	Relation between heat transfer and equiaxed grains.	63
Figure 3.14	Macrography of the Gr.50 workpieces in three sections using: a) low (0.02 wt%), b) medium (1.09 wt%) and c) high (2.15 wt%) Ni content filler metals. Etched by Nital 4%.	66

Figure 3.15	Macrography of the Gr.80 workpieces in three sections using: a) low (0.02 wt%), b) medium (1.99 wt%) and c) high (2.39 wt%) Ni content filler metals. Etched by Nital 4%.....	67
Figure 3.16	Measurement of weld face height (H2), excessive penetration height (H1) and penetration length (L) for Gr.80 welds. All specimens are etched by Nital 4%.....	68
Figure 3.17	Relation between weld face height, excessive penetration height and susceptibility to hot cracking in Gr.80 weld metals.	69
Figure 3.18	Effect of shielding gas mixture on weld penetration.....	69
Figure 3.19	An example in specimen 80-1-1 illustrating the V-shape profile at both upper and lower sides in red dash lines. The distances between centerline and weld-base borders are illustrated by arrows.	70
Figure 3.20	Schematic illustration of the time needed for completion of dendrite growth depending the width of the fusion zone.	71
Figure 3.21	Schematic illustration of nucleation of a hot cracking at centerline; a) liquid before starting the solidification. b) nucleation and growth of dendrites, c) dendrites of V-shape area meet at centerline. d) dendrites which meet in stage c are being contracted and at the same time adjacent dendrites are developing and meeting each other blocking the liquid feeding path to narrow V-shape area which forms the first void.	72
Figure 3.22	Consecutive images from equiaxed grains at weld face from a to d and their effect on crack stoppage (specimen: 80-1-1, hot etched).....	73
Figure 3.23	Dendrites with well developed secondary arms in Gr.50 (specimen: 50-1-3, hot etched).....	78
Figure 3.24	Centerline of the weld metal; a) sound centerline in Gr.50 specimen. b) the same zone in higher magnification (specimen:50-4-3, etched by Nital 4%). ...	79
Figure 3.25	Dendrites with short secondary arms in Gr.80 (specimen: 80-4-3, hot etched).....	79
Figure 3.26	Long secondary dendrite arms in Gr.50 in a) low and b) high magnification. SDA tips are shown by arrows (specimen: 50-4-3, hot etched).....	80
Figure 3.27	Short secondary dendrite arms in Gr.80 in a) lower and b) higher magnification (specimen: 80-4-3, hot etched).....	80
Figure 3.28	Evolution of solidification mode by increase in constitutional supercooling. ...	81

Figure 3.29	Comparison of grain size in HAZ of a) Gr.50 and b) Gr. 80 adjacent to the weld.	82
Figure 3.30	Schematic representation of epitaxial fusion line ABC proposed by	82
Figure 3.31	Centerline of the weld where hot cracking follows the inclusions engulfed with gas porosities (specimen BK2-1, hot etched).....	83
Figure 3.32	Acicular ferrite nucleated from inclusions; a) Gr.80 (specimen: K03-1, hot etched) b) Gr.50 (specimen: 50-1-1, hot etched).	84
Figure 3.33	Morphologies of different types of inclusions in weld metal observed by FEG-SEM (specimen:80-4-3, hot etched).....	85
Figure 3.34	EDS mapping on weld metal showing the existence of Al,V and Ti in inclusions (specimen: 80-4-3, hot etched).....	86
Figure 3.35	Inclusions in as polished weld metal (specimen: 80-4-3).	86
Figure 3.36	Microstructure of Gr.50 welds containing acicular ferrite (AF), Widmanstätten (WF) and allotriomorphic ferrite (Allot) welded by filler containing a) low Ni, b) medium Ni, c) high Ni (all specimens are etched by Nital 4%).	88
Figure 3.37	Microstructure of Gr.80 welds containing acicular ferrite (AF), Widmanstätten (WF), allotriomorphic (Allot) welded by filler containing a) low Ni, b) medium Ni, and c) high Ni (all specimens are etched by Nital 4%).	88
Figure 3.38	Illustration of allotriomorphic ferrite in dendrite boundary. Arrows illustrate the boundaries between ferrites (specimen: 50-1-1, hot etched).....	89
Figure 3.39	Allotriomorphic ferrites in equiaxed grain boundaries with Widmanstätten ferrite nucleated from the allotriomorphies (specimen 50-1-3 etched by Nital 4%).	89
Figure 3.40	EDS mapping showing microsegregation of components at centerline of Gr.80 weld (specimen: 80-4-3, hot etched).....	92
Figure 3.41	EDS mapping showing microsegregation of components at centerline of Gr.50 weld (specimens:50-4-3, hot etched).	93
Figure 3.42	Comparison of solidification range calculated for weld specimens at cooling rate of 100°C/s.....	94
Figure 3.43	Comparison of solidification range calculated for weld specimens at Equilibrium cooling rate.	94

Figure 3.44	CCT diagram calculated for HAZ of Gr.50 welds.	95
Figure 3.45	Microstructure evolution in HAZ of a Gr.50 weld locations a to f (specimen: 50-4-3, hot etched).locations g to l (specimen: 50-4-3, hot etched).....	97
Figure 3.46	Hardness variation from base metal to the weld in Gr.50 (specimen: 50-4-3, hot etched).	99
Figure 3.47	CCT diagram calculated for HAZ of Gr.80 welds.	100
Figure 3.48	Microstructure evolution in HAZ of a Gr.80 weld, from a to d (specimen: 80-4-3, hot etched).	102
Figure 3.49	Evolution of average grain size in HAZ of Gr80 as a function of distance from the weld (specimen: 80-4-3).	103
Figure 3.50	Hardness variation from base metal to the weld of Gr.80 (specimen: 80-4-3).	103
Figure 3.51	EDS analysis on complex carbonitrides of Gr.80 HAZ (specimen: BK2-2, hot etched).	104
Figure 3.52	Complex carbonitrides distributed in HAZ of Gr.80 (specimen: BK2-2, hot etched).	105

LIST OF ABBREVIATIONS

AF	Acicular Ferrite
Allot	Allotriomorphic ferrite
ASTM	American Society for Testing and Materials
AWS	American Welding Society
BCC	Body Centered Cubic
BCT	Base Centered Tetragonal
BK	Back Plate
BRT	Brittle Temperature Range
CE	Carbon Equivalent
DAS	Dendrite Arm Spacing
DC	Direct Current
DDC	Ductility Dip Cracking
EBS	Electron Backscatter Diffraction
EDS	Energy-Dispersive X-ray Spectroscopy
EP	Electrode Positive
FATT	Fracture Appearance Transition Temperature
FCAW	Flux-cored Arc Welding
FCC	Face Centered Cubic
FEG	Field Emission Gun
FEM	Finite Element Method
FPI	Fluorescent Penetrant Inspection
GBF	Grain Boundary Ferrite
GMAW	Gas Metal Arc Welding
HAZ	Heat Affected Zone
HSLA	High Strength Low Alloy
MMAW	Manual Metal Arc Welding
M _s	Martensite Start
PDA	Primary Dendrite Arm

XXIV

PMZ	Partially Melted Zone
ppm	Part per million
SAE	Society of Automotive Engineers
SAW	Submerge Arc Welding
SB	Single bevel
SDA	Secondary Dendrite Arm
SDAS	Secondary Dendrite Arm Spacing
SEM	Scanning Electron Microscope
TEM	Transmission Electron Microscopy
TIG	Tungsten Inert Gas
W.S	Welding speed
WF	Widmanstätten ferrite

LIST OF SYMBOLS

°C	Degree Celsius
μm	Micrometer
A	Amperage
A%	Total elongation percentage
A ₃	Equilibrium temperature for α+γ/γ phases
cm	Centimeter
D	Depth
DI	Dilution
dia	Diameter
ε _{ext}	External strain
ε _{int}	Internal strain
ε _{red}	Safety margine
F	Fahrenheit
ft.lbf	Foot. pound force
G	Temperature gradient
γ	Austenite
H	Heat input per unit length (KJ/cm)
h	Height
H1	Excessive penetration height
H2	Weld face height
In	Inch
In/min	Inch per minute
KJ	Kilo joule
Ksi	Kilo pound per inch
L	Penetration length
mm	millimeter
MPa	Mega Pascal
nm	Nanometer

Q	Heat input (KJ)
R	Movement rate of the solidification front
R _e	Ultimate tensile strength
R _p	Yield strength
T	Temperature
t	Time
t _r	Solidification elapsed time
V	Voltage
W	Width
W/(mK)	Watts per meter-kelvin
Wt%	Weight percent

INTRODUCTION

High strength low alloy (HSLA) steels are widely used in transportation industry. Although the microstructure of weld metal of HSLA steels is well-known for its crack resisting nature but welding of HSLA steels is still challenging. This research is investigating the main phenomena contributing to hot cracking during welding of HSLA steels. Although many academic researches have been accomplished on hot cracking, limited number of studies have focused on a specific type of steel. Most of the root causes and proposed remedies for hot cracking are stated generally for all types of metals regardless of the nature of the investigated alloy. The aim of current research is to identify the link between microstructure, mechanical and physical properties of weld, HAZ and base metal of two grades of HSLA steels (ASTM A656 Gr.80 and ASTM A572 Gr.50). The research is based on metallographic results accompanied with chemical analysis and microhardness lines. The phase transformation and physical properties calculated by JMatPro software are also employed to explain the results. After investigation of root causes, remedies are proposed to avoid hot cracking during the welding of these alloys. The scope of the current work is limited to solidification hot cracking in weld metal of HSLA steels welded by Gas Metal Arc Welding (GMAW). Other types of weld defects such as cold cracking and cracks in partially melted zone (PMZ) are not part of the current research. In addition to investigation of hot cracking root causes, the microstructure of base metal, weld and heat affected zone (HAZ) is characterized and discussed.

CHAPTER 1

LITERATURE REVIEW

1.1 HSLA steels

High strength low alloy (HSLA) steels have been developed to provide a high level of strength and toughness and better atmospheric corrosion resistance compared to carbon steels. Carbon content of HSLA steels is usually kept in the range of 0.05-0.25 wt%. The low amount of carbon substantially increases the formability of this type of steels. Strength reduction due to low carbon content is compensated by the effect of microalloying elements [1]. Although the sum of microalloying elements (Nb, V and Ti) in HSLA steels usually does not exceed 0.2 wt%, they have an important increasing effect on strength and toughness. The yield strength of HSLA steels is usually over 345 MPa and due to extremely low amount of alloying elements, the use of HSLA in industrial designs is economically preferred. Elimination of heat treatment cost without adding a high amount of alloying elements and at the same time benefiting the desired mechanical properties encourages the designers to use HSLA steels [2-4]. Oil and gas pipelines, construction and farm machinery, rail vehicles, heavy duty vehicles, storage tanks, snowmobiles, off-shore structures and power transmission towers are some examples of HSLA steels application [5]. Depending on the applications, loading conditions and environmental requirements, different grades of HSLA steels are being used by design engineers.

Different microstructures are possible for HSLA steels depending on the chemical composition and manufacturing technics. Ferrite-pearlite is a conventional microstructure, however HSLA steels with acicular ferrite microstructure are being used due to excellent strength, weldability and toughness. Dual phase steels which contain martensite dispersed in a ferrite matrix is another possible microstructure in HSLA steels which provide a good combination of tensile strength and ductility. Adding small amounts of Zr, Ca or rare earth elements to HSLA steels may change the shape of sulfide inclusions from elongated stringers to spherical globules and therefore improve the ductility. Figure 1.1 shows the microstructure

of a HSLA steel with yield strength of 450 MPa including ferrite grains and pearlite bands [5].

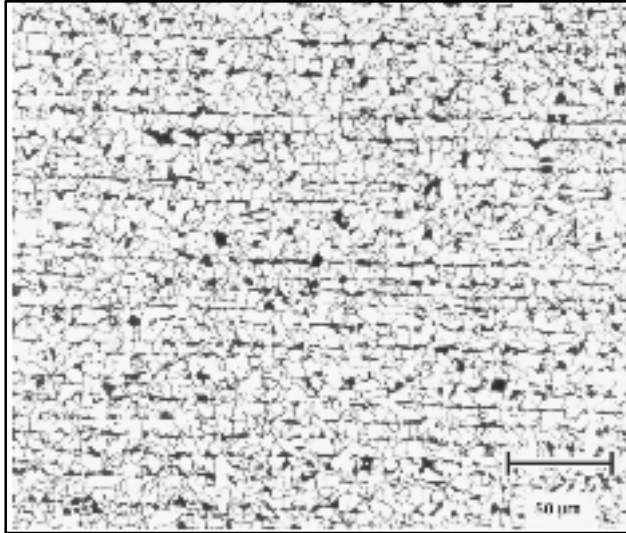


Figure 1.1 Microstructure of as rolled HSLA steel with equiaxed ferrite grains (white area) and pearlite bands (dark area).
Taken from ASM handbook Vol. 9 (2004, p.609)

All three microalloying elements (Nb, V and Ti) are strong carbide and nitride formers [53]. Therefore, the microstructure of HSLA steels contains a fine dispersion of carbonitrides. Figure 1.2 shows the complex carbonitrides in a Nb-Ti HSLA steel [8]. Carbides, nitrides and carbonitrides act with both grain refinement and precipitation mechanisms. The effectiveness of these particles depends on their solubility in austenite. Figure 1.3 compares the solubility of carbides, nitrides and carbonitrides of Nb, V and Ti in austenite. Vanadium carbides are soluble in austenite at relatively high temperature, therefore they contribute mostly by precipitation mechanism. Vanadium carbonitrides are reported to be 5-100 nm in size. The strengthening effect of Vanadium is reported to be 0.7 to 2 Ksi (5 to 14 MPa) per 0.01 wt% of Vanadium [5].

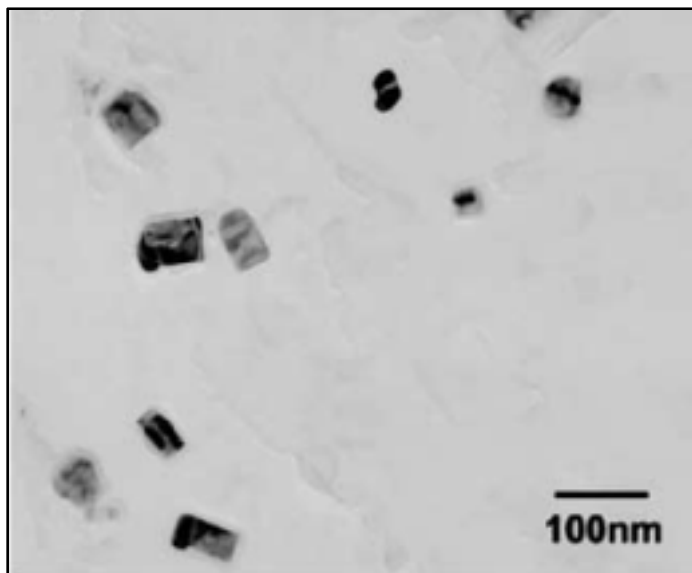


Figure 1.2 Complex carbonitrides in Nb-Ti HSLA steel.
Taken from Hong et al. (2002, p.166)

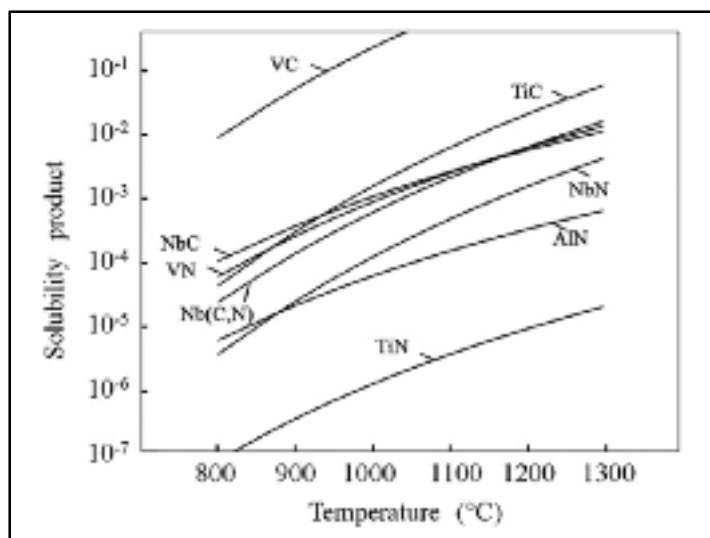


Figure 1.3 Solution of carbides, nitrides and carbonitrides in austenite.
Taken from Russo Spena et al.(2013, p.213)

As Vanadium carbonitrides are not stable at normal hot rolling temperature, their formation depends on the cooling rate. As shown in Figure 1.4, an optimum cooling rate can be proposed to have the most effective strengthening. Cooling rate higher than critical value leads the Vanadium carbonitrides to remain in solution and loss of strengthening effect. On the other hand, a lower cooling rate may coarsen the carbonitrides and decrease their effectiveness [5].

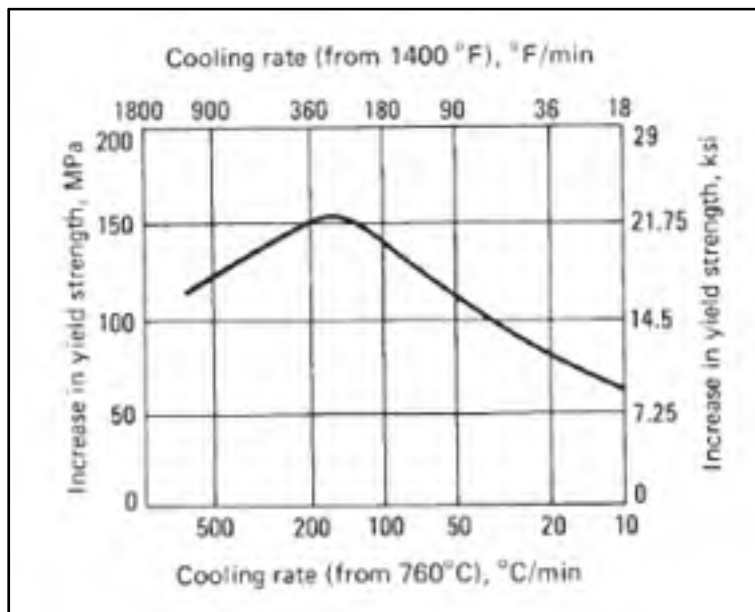


Figure 1.4 Precipitation strengthening as a function of cooling rate in a HSLA steel with 0.15 wt% of Vanadium. Taken from Davis (2001, p.200)

Due to higher stability of niobium carbides in austenite, the grain refinement by niobium is more effective compared to vanadium. However, niobium strengthens the alloy also by precipitation hardening. The strengthening effect of Niobium is reported to be 5 to 6 Ksi (35 to 40 MPa) per 0.01 wt% of Niobium [5].

The most effective particles which prevent the grain growth are TiN as they are the most stable particles among the carbides and nitrides of Vanadium, Niobium and Titanium [9].

The carbonitrides which are nucleated at higher temperatures have been reported to be rich in Titanium and Nitrogen and contain low amount of Carbon. By decreasing the temperature, further Ti(C,N) layers are formed on the previously formed Ti-N rich carbonitrides. Continuing temperature decrease, the Carbon content of carbonitrides is increased and eventually Nitrogen maybe exhausted from the matrix. Niobium starts to precipitate on outer layers of the particle by decreasing the temperature. After exhausting Nitrogen, another set of (Ti,Nb)C will be formed. The larger is the complex carbonitrides, the more will be the Niobium content. This has been related to the nucleation of the first particles in higher temperature which act as potential site for nucleation of Niobium rich phases at lower temperature. Nucleation of Niobium rich phases on early formed carbonitrides leads to removal of Niobium from the matrix and therefore formation of small carbonitrides containing less amounts of Niobium in the last stages of cooling [10].

HSLA steels are classified by ASTM according to chemical composition, required mechanical properties and applications. Table 1.1 shows a partial list of this classification. Each group of ASTM classified HSLA steels is available in different grades. For example, four grades are introduced for ASTM A572 as Gr.42, Gr.50, Gr.60 and Gr.65 where the last two characters represent the yield strength of the steel in Ksi.

SAE (Society of Automotive Engineers) also proposes another common classification. In SAE classification, three first digits indicate the minimum yield strength in Ksi followed by one or more letters indicating carbon level, chemical composition or deoxidation process. As an example killed steel (K), low carbon (L), low alloy (X), not killed steel (O) and killed plus inclusion control (F). For example, a steel coded as SAE 050XLK is a low carbon, low alloy killed steel with a minimum yield strength of 50 Ksi (345 MPa) [4]. However, some commercial names are also used for HSLA steels. For example, HSLA 80 and HSLA 100 are the HSLA steels with a yield strength of 80 Ksi (552 MPa) and 100 Ksi (689 MPa), respectively [4].

HSLA steels show a proper weldability due to the low amount of carbon and alloying elements. This leads to a low level of carbon equivalent (CE) in HSLA steels and therefore low susceptibility to cold cracking in HAZ [5]. Microstructure of HSLA steel welds is reported to have a proper resistance to crack growth. However, challenges are still present in welding of HSLA steels. Primary manufacturing processes of the base metal and large size of welds in industrial structures enhance the susceptibility of HSLA steel welded structures to hot cracking. Generally, preheating and high inter-pass temperature dramatically lower the cooling rate. Decreasing the cooling rate reduces the susceptibility to cracking. Due to the application of HSLA steels in transportation vehicle and pipelines, the welded structures are usually very large which makes the preheating process difficult. On the other hand, inter-pass temperature is usually low during welding of large workpieces of HSLA steels which increases the susceptibility to hot cracking [9].

Table 1.1 A partial list of HSLA steels (ASTM classification).
Taken from Bramfitt et al. (2002, p.8)

ASTM designation	Type of steel
ASTM A242	HSLA structural steel
ASTM A572	HSLA Nb-V structural steel
ASTM A588	HSLA structural steel with 350 MPa minimum yield strength
ASTM A656	HSLA hot rolled structural V-Al-N and Ti-Al steel
ASTM A714	HSLA welded and seamless steel pipe
ASTM A715	HSLA hot rolled and strip, and sheet steel, cold rolled high strength, low alloy with improved formability
ASTM A808	HSLA with improved notch toughness
ASTM A871	HSLA steel with atmospheric corrosion resistance

1.1.1 Microstructure of weld metal

The final microstructure of HSLA steel weld metal depends on chemical composition and cooling rate. The common microstructure for HSLA steel is acicular ferrite (AF) which nucleates heterogeneously from nonmetallic inclusions. However, various ferrite morphologies have been reported [11, 12]. Figure 1.5 shows different morphologies of primary ferrite observed in a HSLA steel weld metal. As shown in Figure 1.5 a and b, continuous and allotriomorphic grain boundary primary ferrites (GBF) have been reported to nucleate on primary austenite grain boundaries [11]. Two other morphologies have been classified under the primary ferrite: idiomorphic primary ferrite, nucleated from nonmetallic inclusions and intragranular primary ferrite, nucleated inside the austenite grain as showed in Figure 1.5c and d. Widmanstätten ferrite nucleates from GBF (Figure 1.6b) or non-metallic inclusions (Figure 1.6c). However, in the absence of GBF, Widmanstätten ferrite can also nucleate directly from austenite grain boundaries (Figure 1.6a) or even intragranularly inside the austenite grain (Figure 1.6d). Widmanstätten ferrite which nucleates directly from austenite grain boundaries can be also classified under primary ferrite morphologies and can be named as primary Widmanstätten ferrite [11]. Distinguishing between acicular, idiomorphic and Widmanstätten ferrite is often challenging as all three types can nucleate from nonmetallic inclusions. As a general rule, the ratio of length to width is used as a criterion to differentiate acicular ferrite blades from intragranular Widmanstätten ferrite. Blades with length to width ratio lower than 4 are classified as acicular ferrite, otherwise identified as Widmanstätten ferrite. Difference between acicular ferrite and idiomorphic ferrite is determined by blade width. Acicular ferrite blade has typically a width equal or less than 5 μm while the width of idiomorphic primary ferrite blade is higher than 5 μm . Furthermore, a unique aspect of acicular ferrite which helps to differentiate it from other morphologies is high angle boundary. Acicular ferrite blades are separated by high angle boundaries while Widmanstätten and GBF are low angle boundary phases [11]. The volume fraction of acicular ferrite in a weld metal containing different ferrite morphologies have been determined based on boundaries' angle by Ghomashchi, et al. using EBSD as shown in Figure 1.7 [11].

In case of hardenability increase, existence of bainite and low carbon martensite is also probable [13]. As shown in Figure 1.8 both upper (parallel layers of ferrite and cementite) and lower bainite (ferrite laths with cementite distributed inside them) have been observed in HSLA steel weld metal [11].

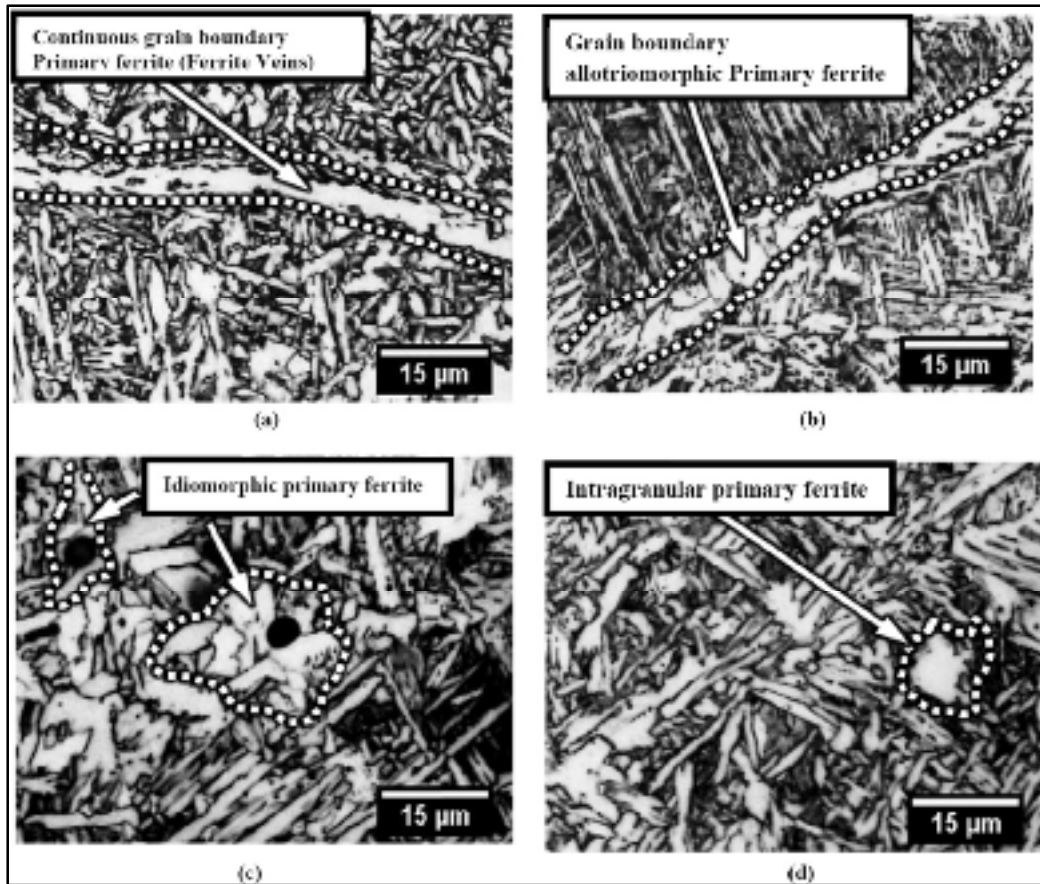


Figure 1.5 Different morphologies for primary ferrite in HSLA X70 weld metal; a) continuous GBF nucleated from austenite grain boundary, b) allotriomorphic primary ferrite nucleated on austenite grain boundary, c) idiomorphic primary ferrite nucleated from nonmetallic inclusions, d) intragranular primary ferrite nucleated inside the austenite grain.

Taken from Ghomashchi et al. (2015, p.322)

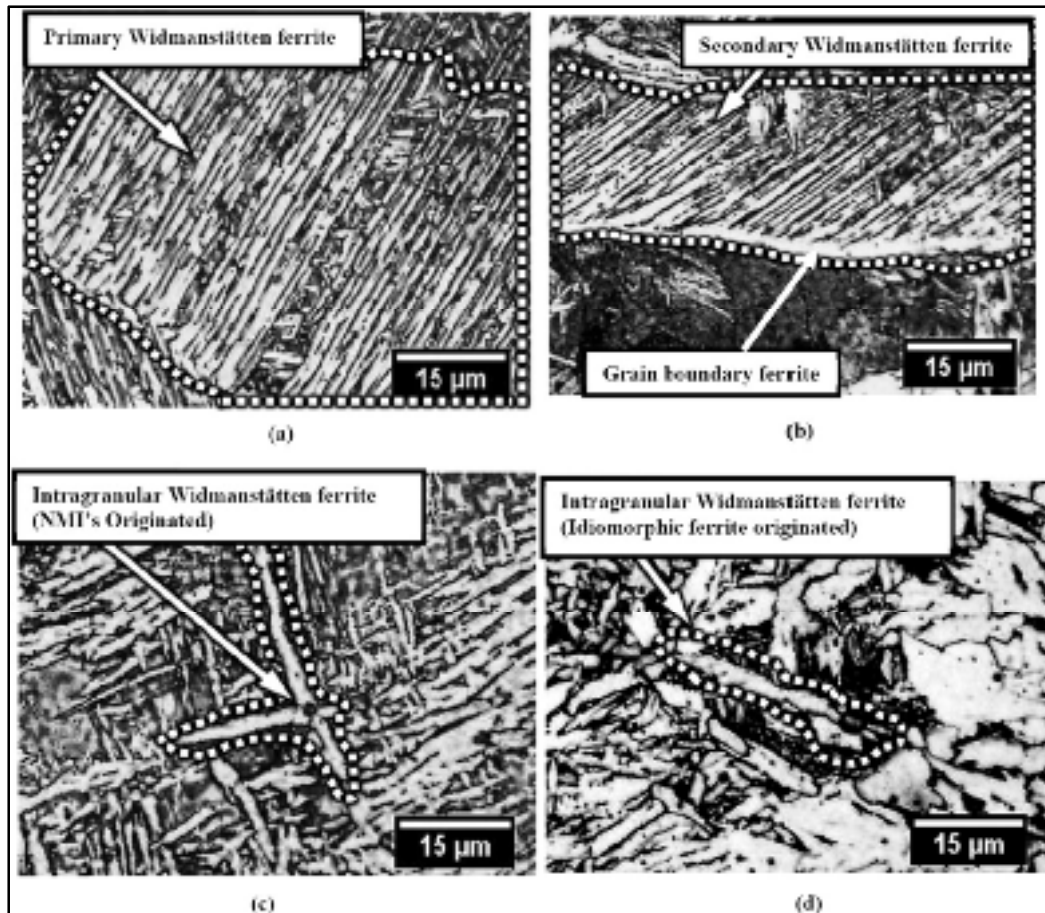


Figure 1.6 Different morphologies for Widmanstätten ferrite in HSLA X70 weld metal; a) primary Widmanstätten ferrite nucleated from austenite grain boundaries, b) secondary Widmanstätten ferrite nucleated from GBF, c) primary Widmanstätten ferrite nucleated from nonmetallic inclusion, d) intragranular Widmanstätten ferrite nucleated from idiomorphic ferrite.

Taken from Ghomashchi et al. (2015, p.322)

Despite of existence of different morphologies, acicular ferrite has been reported as predominant microstructure in HSLA steels weld metal. Yield strength of weld metal has been reported to be higher than HAZ and base metal as a result of existence of acicular ferrite and bainite [14].

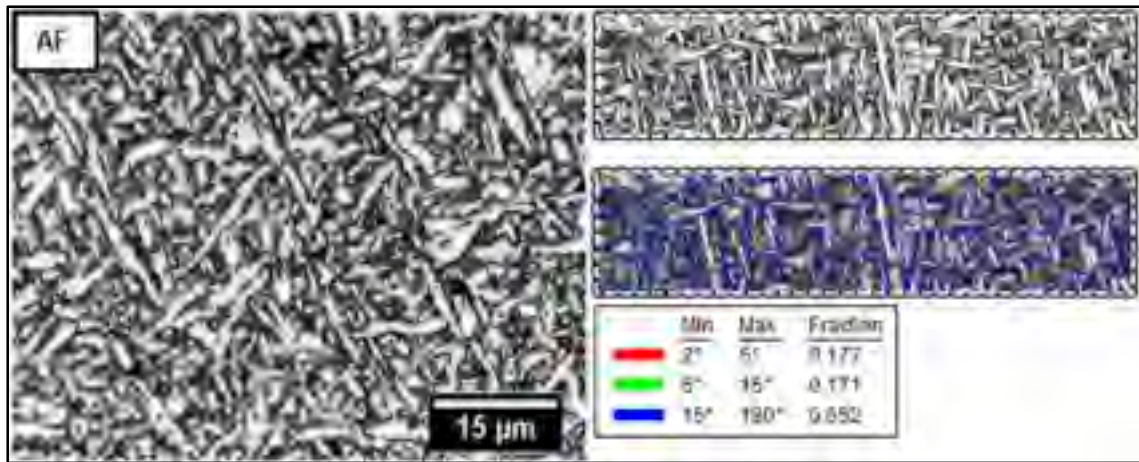


Figure 1.7 Acicular ferrite with high angle boundaries differentiated from other ferrite morphologies using EBSD.
Taken from Ghomashchi et al. (2015, p.323)

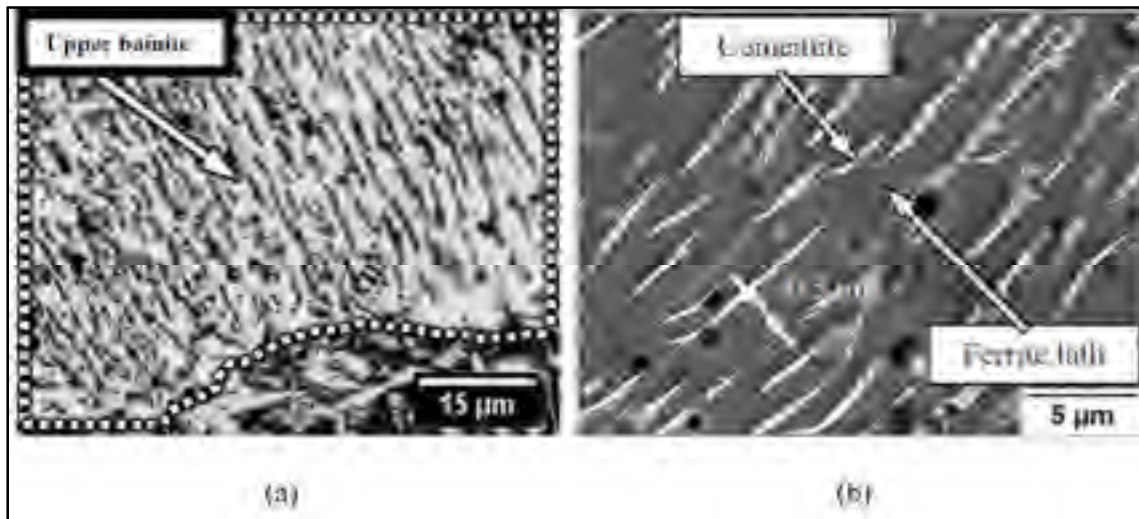


Figure 1.8 Different bainite morphologies in HSLA X70 weld metal; a) upper bainite with parallel ferrite and cementite layers, b) lower bainite with cementite distributed in ferrite lathes.

Taken from Ghomashchi et al. (2015, p.323)

Figure 1.9 indicates the nucleation of acicular ferrite from an inclusion. Chemical composition of inclusions affects their ability for nucleation of acicular ferrite. As shown in

Table 1.2 some of the inclusions are active in acicular ferrite nucleation and some of them are inert [15].

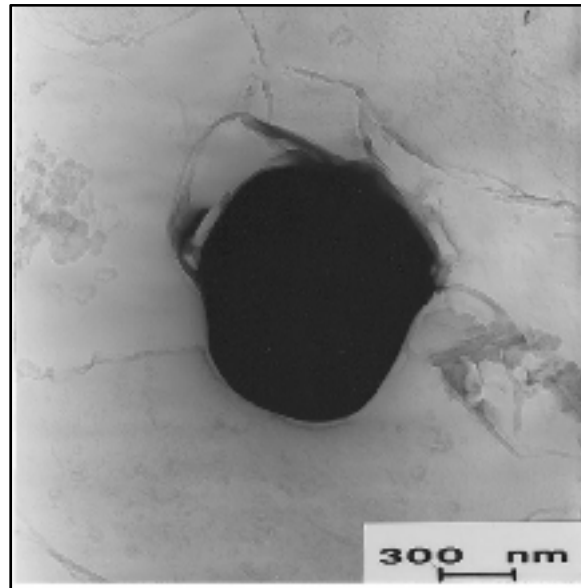


Figure 1.9 TEM image of an inclusion which acicular ferrite nucleated on.
Taken from Madariaga et al. (1999, p959)

Investigation on effect of alloying elements on microstructure of HSLA steels is always challenging. Table 1.3 summarizes the effect of some alloying elements on acicular ferrite nucleation [15].

It has been reported that adding Mo in the range of 0.817-0.881 wt% in API HSLA-70 increases the impact toughness and causes a substantial reduction in fracture appearance transition temperature (FATT) [17].

Ni increases the impact toughness in weld metal by decreasing the martensite start temperature (M_s) and therefore increasing the retained austenite. By decreasing the M_s , the martensite which is formed at lower temperature has more probability for auto-tempering which in turn causes an increase in toughness [18]. Ni can also strengthen the alloy by making solid solution [13].

Table 1.2 Effect of chemical composition of inclusions on their potential for AF nucleation.

Taken from Zhang et al. (2014, p.1478)

Compound added	Active inclusions for acicular ferrite nucleation	Inert inclusions for acicular ferrite nucleation
Simple oxides	Ti-Oxide(Ti_2O_3 or TiO)	Al_2O_3 , SiO_2 , Ti_2O_3
Complex oxides	$(\text{Ti},\text{Mn})_2\text{O}_3$, TiO_2 - $(\text{MnO}-\text{Al}_2\text{O}_3)$ Galaxite spinel $\text{MnO}-\text{Al}_2\text{O}_3$	$\text{MnO}-\text{SiO}_2$, $\text{MnO}-\text{FeOx}-\text{SiO}_2$, $\text{MgO}-\text{Al}_2\text{O}_3$, $\text{MnO}-\text{Al}_2\text{O}_3$
Simple nitrides	TiN , VN	TiN
Simple sulfides		MnS , CuS
Complex oxy-sulfides and multi-phase inclusions	$\text{Al}_2\text{O}_3-\text{MnS}$, $\text{TiO}_2-\text{Al}_2\text{O}_3-\text{MnS}$, Ti and Ti-Ca-oxy-sulfides, $\text{Ti}_2\text{O}_3-\text{TiN}-\text{MnS}$, $\text{TiOx}-\text{TiN}-\text{MnS}$, $\text{FeS}-(\text{Mn},\text{CU})\text{S}$, $\text{MnS}-\text{VC}$, $\text{MnS}-\text{V}(\text{C},\text{N})$	

It has been reported that adding Ni without Mo in the range of 2.03-3.75 wt% in API HSLA-70 reduces the volume fraction of acicular ferrite and therefore degrades the toughness. But adding both Ni (2.03-2.91 wt%) and Mo (0.7-0.995 wt%) enhances the volume fraction of acicular ferrite compared to grain boundary ferrite [17]. On the other hand, high Ni content can also have detrimental effects. It has been reported that high amount of Ni in weld metal induces Ni, Mn and Si compounds which segregate at weld centerline or grain boundaries and therefore increases the risk of hot cracking [19].

As shown in Figure 1.10, in order to prevent detrimental effect of high amount of Ni on toughness of weld metal, it is recommended to decrease Mn content [20]. The effect of ferrite morphology and alloying elements of weld metal, especially on resistance to hot cracking is the matter of interest in the current work which will be further discussed in the next paragraphs. Microstructure and chemical composition of base metal will be used to explain

the results of the current work and discuss the phenomena contributing to the occurrence of weld defects.

Table 1.3 Effect of alloying elements on acicular ferrite nucleation
Taken from Zhang et al. (2014, p.1478)

Element type	Alloying element	Optimum range (wt%)	Effect on AF	Welding process
Austenite stabilizer	C	0.05-0.15	Small increase	MMAW
	Mn	1.40-1.92	Mild increase	SAW
	Ni	2.03-2.91	Moderate increase	SAW
	Cu	0.14-0.94	Moderate increase	MMAW
Ferrite stabilizer	Mo	0.7-0.995	Large increase	SAW
	Cr	0.05-0.91	Moderate increase	MMAW
	Ti	0.02-0.05	Moderate increase	SAW
	B	0.003-0.006	Small decrease	FCAW

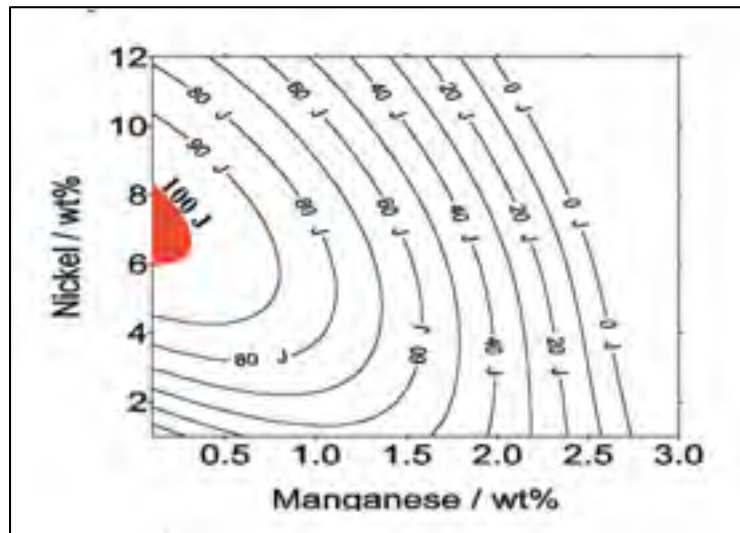


Figure 1.10 Prediction of weld toughness at -40°C as a function of Ni and Mn content.
Taken from Keehan et al.(2002 p.1)

1.1.2 Microstructure of heat affected zone

Figure 1.11 shows the microstructure of heat affected zone (HAZ) in HSLA-100. As shown in Figure 1.12 bainite packets exist as predominant microstructure in HAZ of HSLA steels weld. Acicular ferrite and martensite can be also formed depending on the chemical composition and cooling rate. Prior austenite grain size affects dramatically the microstructure and mechanical properties of HAZ. Prior austenite grain size decreases gradually by increasing the distance from the fusion zone. The coarse grains in HAZ adjacent to the fusion zone are susceptible to cold cracking due to decrease in toughness. Increasing heat input will result in wider coarse grain area in HAZ. Therefore, there will be a wider low toughness area. It has been found that coarse grain HAZ length is 0.5mm for a heat input of 10 KJ/cm while it is 1.1mm for a heat input of 40 KJ/cm in HSLA-100 welded plate [21].

The correlation between modeling and experimental results for grain size and microstructure of HAZ in HSLA steels has been studied based on heat input. This is challenging in HSLA steels because of the presence of carbonitrides which lock the grain growth. As already discussed, solubility of carbonitrides in HSLA steels is increased by increasing the temperature which affects the grain growth. The level of contribution of carbonitrides in grain size of HAZ depends on type of carbonitrides [21]. Although Ti bearing carbonitrides are more effective grain refiners in HAZ compared to Nb bearing carbonitrides, Ti-rich particles have been reported to be detrimental for HAZ toughness specially when the microstructure is bainitic [22].

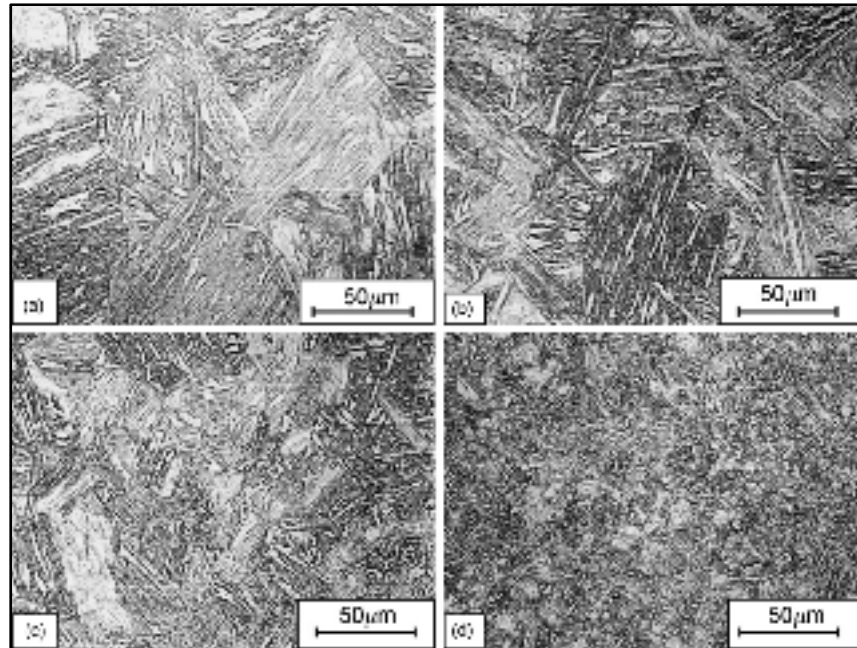


Figure 1.11 Microstructure of various HAZ sections in GMAW welded HSLA-100 steel a) 0.01 mm, b) 0.1 mm, c) 0.3 mm, d) 0.7 mm from fusion line.
Taken from Shome (2007, p.456)

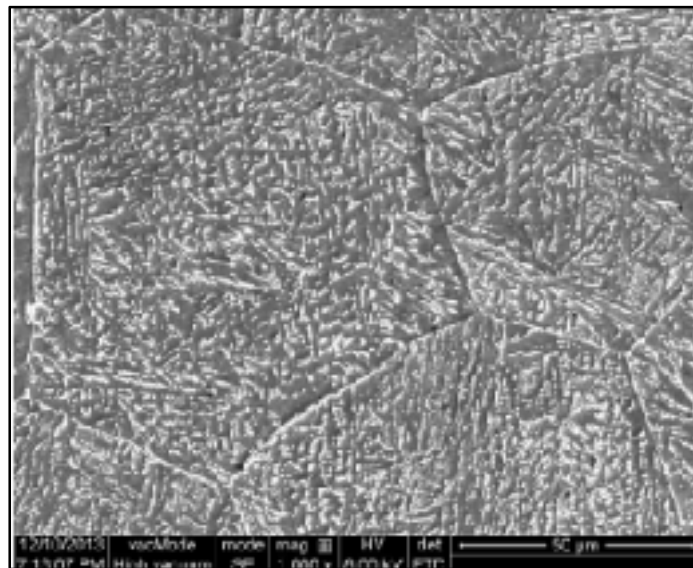


Figure 1.12 Bainite packets in HAZ of a HSLA steel.
Taken from Cao et al. (2015, p.3005)

1.2 Weld defects

1.2.1 Cold cracking

Cold cracking or hydrogen cracking usually occurs at relatively low temperature (-100 to 200°C) in HAZ but also can appear in weld metal [9]. Four major factors contribute to cold cracking: 1) hydrogen content of the weld metal which comes from humidity or molecules of organic materials. 2) formation of sensitive microstructure (martensite), 3) high stress during the cooling caused by solidification shrinkage and 4) thermal contraction under constraints. The commonly observed positions of cold cracking are illustrated in Figure 1.13.

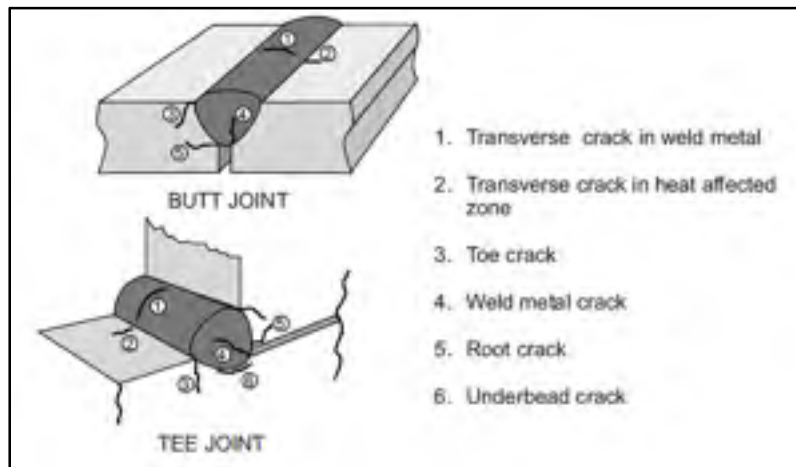


Figure 1.13 Commonly observed positions of cold cracking.
Taken from Welding for design engineers (2007, p.446)

Diatomic hydrogen is decomposed to monatomic hydrogen at high temperature. The solubility of monatomic hydrogen in steel increases at high temperature. Therefore, cold cracking can be formed as a result of solution of monatomic hydrogen. Figure 1.14 compares the absorption of monatomic and diatomic hydrogen as a function of distance from the fusion zone [9].

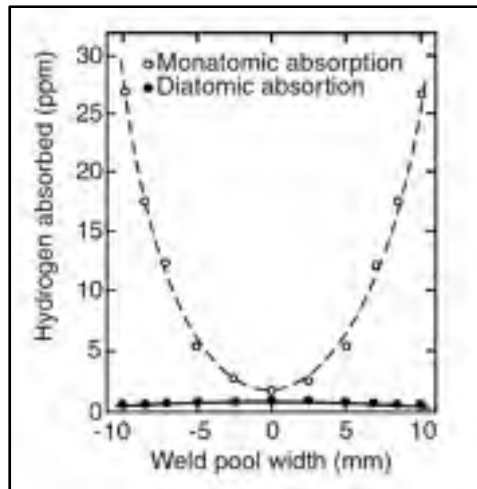


Figure 1.14 Variation of hydrogen absorption in weld pool.
Taken from Kou (2003, p.70)

One of the recommended remedies for resistance to cold cracking in GMAW of HSLA steels is adding fluoride in flux cored wires. Fluoride can decrease the hydrogen content in weld metal. The amount of lessened hydrogen differs by type of fluoride in flux. Wires with CaF_2 have been reported to have the lowest diffusible hydrogen content (6.32 ml in 100 g), while wires with MnF_3 show the highest hydrogen content (7.96 ml in 100 g). It can be explained by the fact that the diffusible hydrogen content in weld metal is degraded when the basicity of slag increases. Basicity of CaF_2 is 0.27 while basicity of MnF_3 is 0.01 [15].

1.2.2 Hot cracking

Generally hot cracking can be divided into three types: 1) Solidification cracking, 2) liquation cracking, 3) ductility dip cracking (DDC).

The most common type of hot cracking is solidification cracking. Solidification is produced by nucleation and growth of grains or dendrites. The grains or dendrites grow towards the centerline of the weld. Therefore the centerline is the last solidified area which is susceptible to be cracked during the solidification [24]. Hot cracking is often detected between dendrites

or grains [9]. Small amount of liquid usually exist in the centerline of the weld. This liquid is caused by low melting point compounds which separate the dendrites during the solidification. The liquid film weakens the centerline, therefore in presence of stress hot cracking can occur at the centerline. This type of hot cracking which occurs at centerline of the weld is called solidification cracking [25].

In contrast to solidification cracking, liquation cracking occurs in the partially melted zone (PMZ). The third type of hot cracking is ductility dip crack (DDC) which occurs in solid state. Below the solidification temperature, the ductility of material which is normally ductile, for example Ni-base or Cu-base alloys, will dramatically decrease which can lead to DDC [26].

As solidification cracking is the most common type of hot cracking and is the subject of the present work, the term ((hot cracking)) will be used in the manuscript only to indicate solidification cracking which occurs at the centerline of the weld during the solidification.

Hot cracking can be in macro or micro scale. Microcracking is not always detectable with non-destructive inspections and therefore they may remain invisible even for some years and then may reveal as a result of notch effect [27]. Hot cracking can be also a nucleation site for stress corrosion cracking [28].

During solidification, the weld metal is contracted. There are two types of contractions: 1) thermal contraction during solidification. 2) Contraction because of volume difference between liquid and solid. In the other words, weld is susceptible to hot cracking because of the difference between density of liquid and solid metal [29]. The effect of thermal contraction on base metal is not as much as the weld metal; therefore, the base metal causes a tensile stress on the mushy zone during the solidification of weld metal [9]. As in mushy zone the grains are not yet strongly bonded, the strength in this semi-solid zone is relatively low and therefore can hardly accommodate the tensile strain [29].

Tensile stress on the weld metal is the main root cause of hot cracking. This tensile stress depends on various factors like the residual stress on base metal prior to welding as a result of manufacturing process or any additional mechanical work on the part prior to welding, thermal properties, microstructure, mechanical properties and chemical composition of both base and weld metal, configuration of the weld joint and using fixture or jig during the welding [30]. Figure 1.15 illustrates the restraint caused by adjacent weld pass in a back-plate weld configuration.

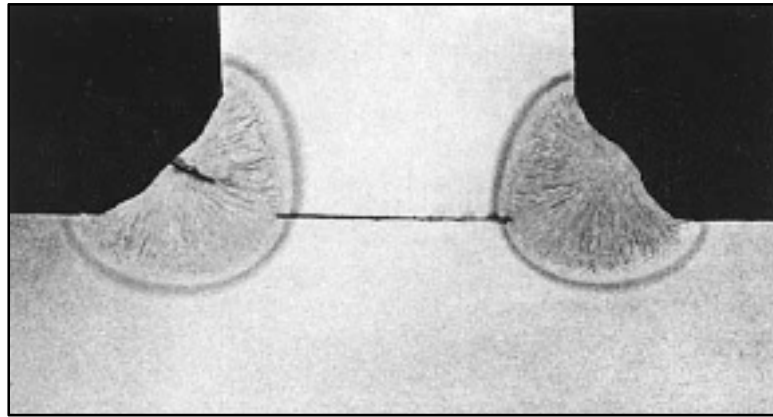


Figure 1.15 Restrain resulting from weld configuration
Taken from Kou (2003, p.285).

As shown in Figure 1.16, the analysis of the residual stresses in T-joint single pass welds of carbon steel SAE 1020 welded by TIG using finite element method (FEM) show that the maximum residual tensile stress is applied on weld face. Residual tensile stress is reduced by increasing the distance from the weld face [31].

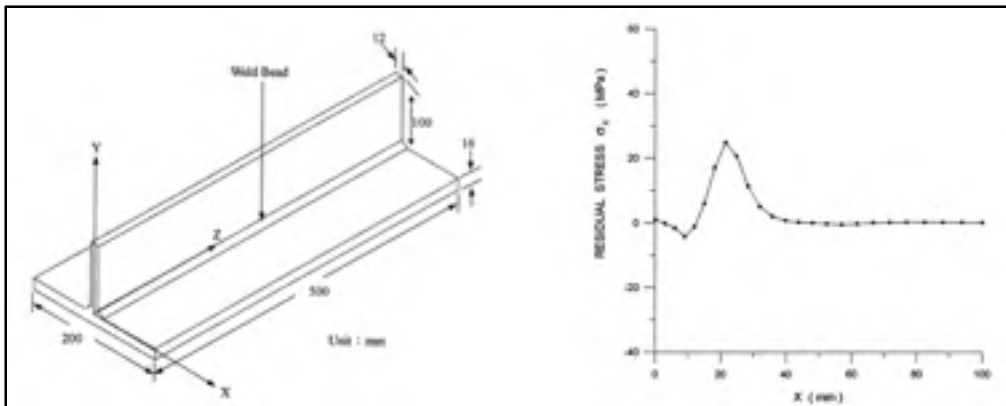


Figure 1.16 Residual stress distribution along X direction resulted from FEM analysis.
Taken from Teng et al. (2001, p.529 and 531)

Figure 1.17 shows a summary of stress sources on weld metal centerline which classifies the stress sources to internal and external. Internal stresses could be due to a combination of 1) negative volume changes during cooling caused by both thermal and phase transformation contractions, and 2) weld geometry which influences stress distribution at the weld face. On the other hand, external stress can be produced by 1) clamping the workpiece which may apply a tensile stress on centerline of the weld, and 2) base metal volume changes due to thermal effects during welding. Similar to the weld metal, the base metal volume changes include both thermal and phase transformation contractions. It has been reported that strength and ductility of weld metal, dimensions of workpiece and joint configuration affect the resistance of centerline against the stress [32].

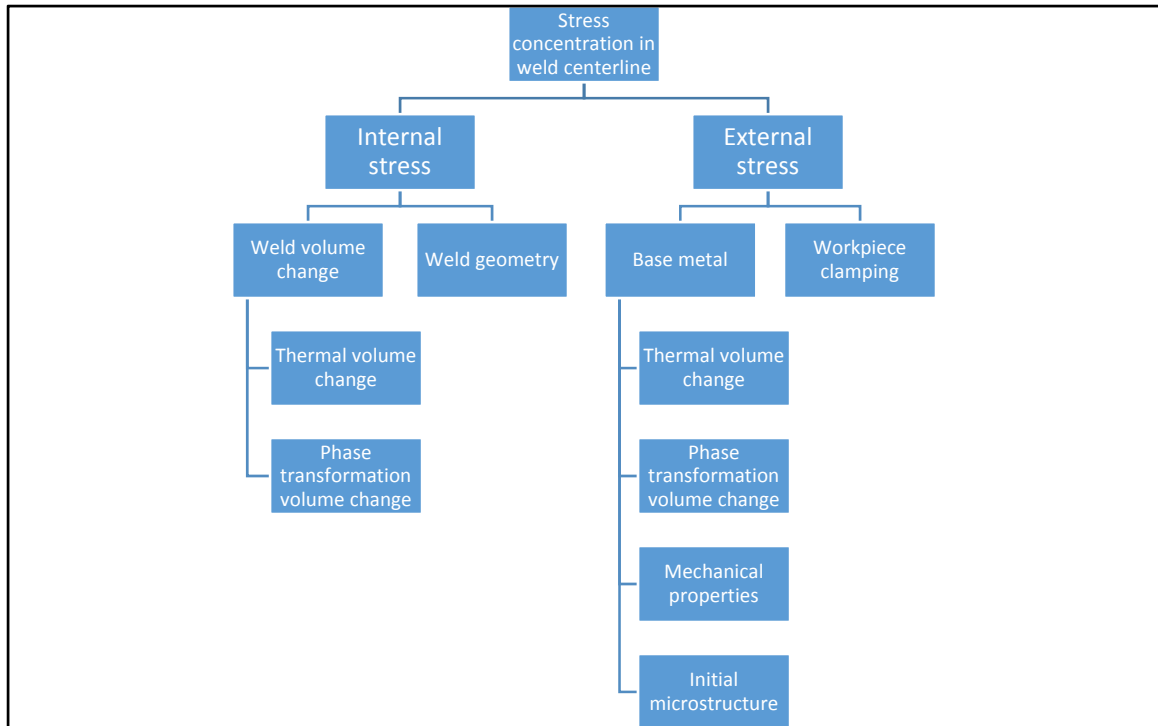


Figure 1.17 Factors influencing stress concentration at weld centerline.

Microstructure of weld metal can affect significantly the susceptibility to hot cracking. various morphologies of ferrite are usually found in weld metal of HSLA steels. In HSLA steels, the aim is usually to induce acicular ferrite in weld metal in order to reduce the susceptibility to hot cracking. Due to the interlocking structure of acicular ferrite, this microstructure has an important role in resistance to crack propagation [15]. Figure 1.18 illustrates how the microstructure can affect the path of crack propagation. In Widmanstätten ferrite nucleated from grain boundary ferrite or austenite grain boundaries, the microstructure contains parallel plates which ease the crack propagation while the chaotic orientation of acicular ferrite nucleated intergranularly on nonmetallic inclusions delays the crack propagation [33].

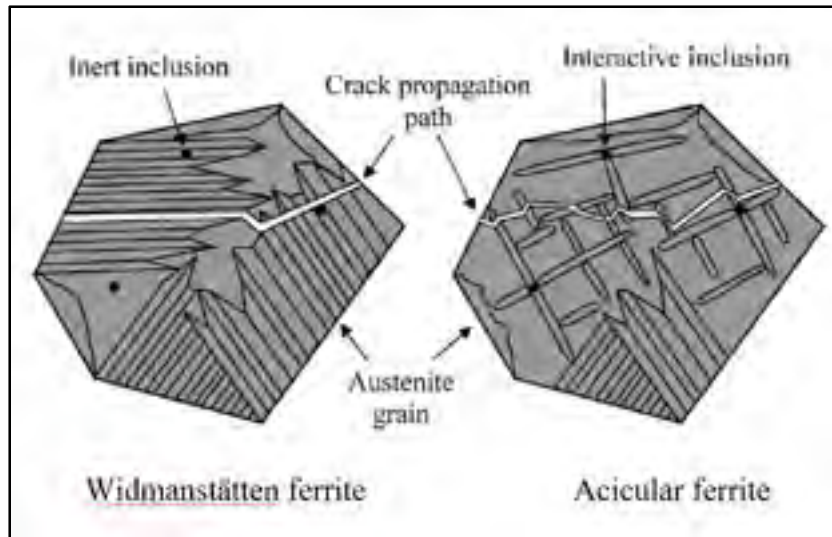


Figure 1.18 Comparison of the path of a cleavage crack in Widmanstätten ferrite and acicular ferrite.
Taken from Sarma et al. (2009, p.1064)

The wider is the solidification range, the wider will be the mushy zone during the solidification. Both solid and liquid coexist in the mushy zone and therefore wider mushy zone weakens the centerline of the weld for hot cracking due to microsegregation of low melting compounds and tramp elements in this zone [9]. Microsegregation is affected dramatically by cooling rate [25]. Existence of P and S can form low melting point compounds which increase the solidification range [9]. Concentration of P and S at grain boundaries increases by increasing the number of thermal cycles. Therefore, multiple layers welds are more susceptible to hot cracking compared to the single layer welds [34]. Fe-S eutectic temperature is 988°C, therefore existence of S can decrease dramatically the solidus temperature from 1400°C [35].

Cu is reported to increase the probability of hot cracking in steels. Solubility of Cu in austenite is limited. Therefore, it can be trapped in boundaries and deteriorate the situation for hot cracking. Sn in weld metal composition exacerbates the effect of Cu by decreasing the solubility of Cu in austenite and decreasing the melting point of Cu-Sn enriched zone [36]. Ni plays a positive role by increasing the solubility of Cu in austenite. Therefore, adding Ni can mitigate the detrimental effect of Cu [37]. Microsegregation of Cr, Mn and Si is also

reported as source of hot cracking in bainitic steels [38]. Also, as shown in Figure 1.19 microsegregation of Ti-rich and Nb-rich phases has been reported to increase susceptibility to hot cracking in weld repair of cast steels [39].

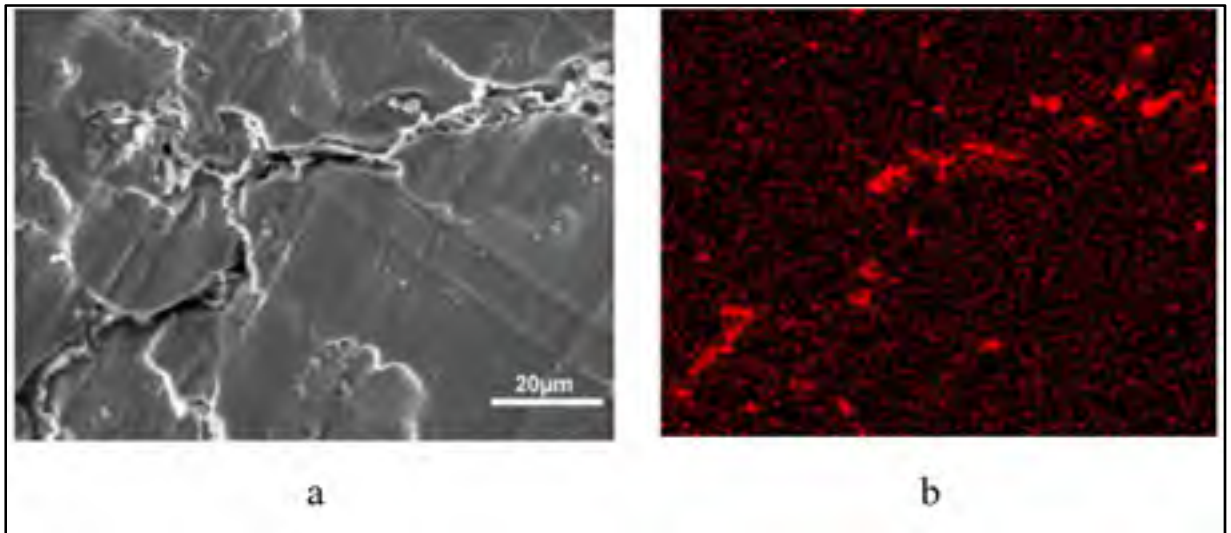


Figure 1.19 Microsegregation of Ti-riched phases in crack path in weld repair of a cast steel, a) crack path, b) EDS map for Ti.
Taken from Branza et al. (2009, p. 546)

Primary phase has an important role in hot cracking. The weld which is solidified from austenite is more susceptible to hot cracking compared to those solidified from delta ferrite due to high solubility of P and S in ferrite [40].

One of the most important items contributing to hot cracking is the liquid surface tension in boundaries. As illustrated in Figure 1.20, high surface tension decreases the probability of formation of liquid film and therefore decreases the susceptibility to hot cracking [9].

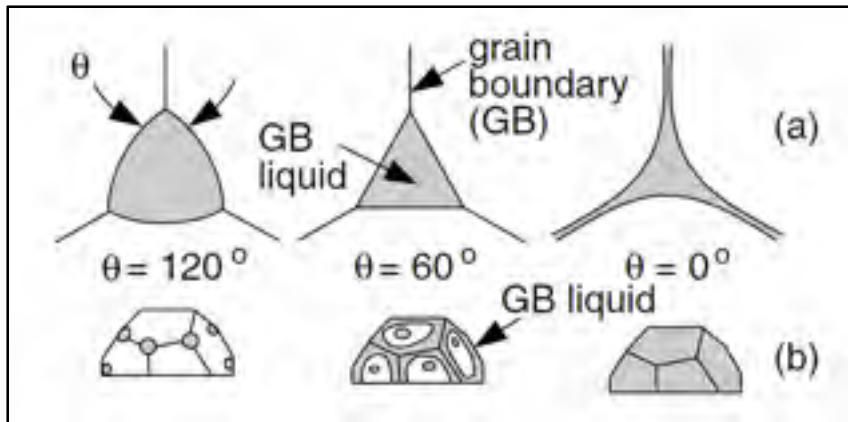


Figure 1.20 Effect of surface tension on wet grain boundaries; a) comparison of angle between liquid and grain boundary in high, medium and low surface tension, b) effect of surface tension on formation of liquid film at grain boundary.

Taken from Kou (2003, p.282)

Increase of grain size leads to higher susceptibility to hot cracking. Fine grains accommodate the strains caused by contraction easier than coarse grains. On the other hand, the smaller is the grain size, the easier will be the feeding of liquid in grain boundaries and therefore the probability of formation of void in fine grain structure is less than coarse grain structure. The total surface of grain boundaries is larger in fine grains and therefore concentration of low melting point compounds is less probable compared to coarse grain structure [9, 27].

A portion of base metal is always diluted in the weld which can be calculated as:

$$D = \frac{\text{Weight of molten base metal}}{\text{Total weight of weld}} \quad (1.1)$$

As shown in Figure 1.21, a practical way to calculate dilution is to estimate it from the 2D image of weld as below:

$$\%DI = \frac{a+b+c}{a+b+c+d} \times 100 \quad (1.2)$$

In which a, b, c and d are the zones specified in Figure 1.21.

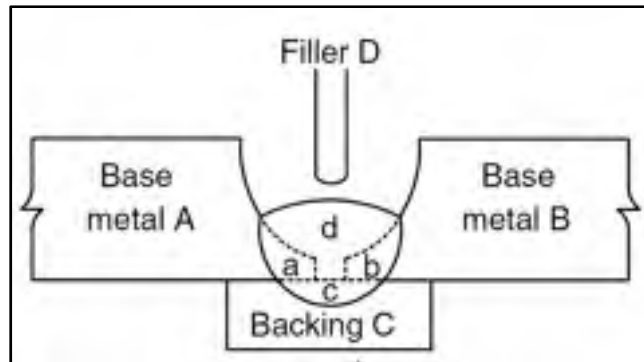


Figure 1.21 Base metal dilution in weld pool.
Taken from Kou (2003, p.257)

The amount of dilution from base metal depends on weld geometry, welding position and heat input per unit length [9]. The contribution of base metal in increasing tramp elements at weld centerline depends on amount of dilution. Segregation of some chemical elements can be observed from the root to further passes. The root pass has a more diluted composition compared to the second pass. Differences in chemical composition from the root to the centerline can lead to a difference in microstructure of the weld metal in different zones. It has been reported that Cr content differs from 18 wt% in first pass to 25 wt% in third pass in a stainless steel which leads to a significant increase in ferrite content in the third pass [41]. Cooling rate and welding speed have important roles on susceptibility to hot cracking. Three factors contribute to cooling rate: 1) weld heat input, 2) preheating and 3) the thickness of base metal [24].

Heat input according to [42] can be calculated as:

$$Q(J) = \text{Voltage}(V) \times \text{Amperage}(A) \times \text{Efficiency factor} \quad (1.3)$$

The efficiency factor is estimated for TIG, GMAW and SAW as 0.6, 0.8 and 0.9 respectively [43].

Considering the effect of welding speed, the heat input per unit length in KJ/cm can be also calculated as:

$$H = \frac{Q \times 60}{1000 \times \text{Welding speed (cm/min)}} \quad [44] \quad (1.4)$$

As seen in Figure 1.22 for welds with similar H, the specimens welded with high speed and high Q are more susceptible to hot cracking compared to those welded with low speed and low Q. The weld pool in Figure 1.22a is tear-drop shaped with perpendicular dendrites which is more likely to be cracked rather than the weld pool in Figure 1.22b with oval weld pool [7].

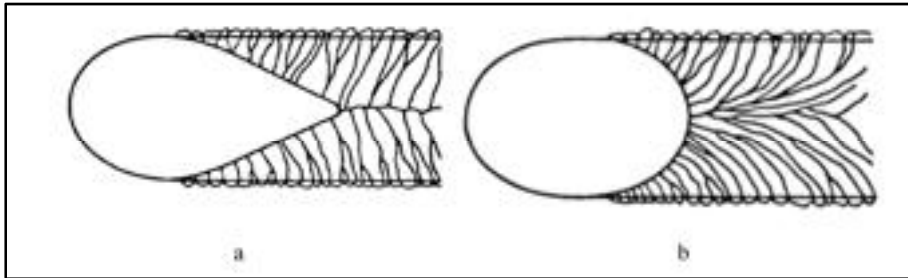


Figure 1.22 Schematic illustration of weld face for similar H, a) high speed and high Q, b) low speed and low Q.

Taken from Kou. (2003, p.176)

High heat input per unit length can deteriorate the mechanical properties of the weld metal by inducing the segregation of low melting point components. High H has also detrimental effects on HAZ by increasing the grain size and lowering the mechanical properties of HAZ. On the other hand, increasing the H can help the auto tempering in weld metal and therefore increase the toughness [45]. In HSLA steel welds, high heat input can significantly increase the size of acicular ferrite plates by increasing the diffusion rate [46].

Temperature gradient and cooling rate both control the solidification pattern. The G/R ratio determines the solidification structure and the product G.R determines the size of grains or dendrites. Figure 1.23 shows the mutual effect of temperature gradient and cooling rate in weld solidification pattern [9]. By increase in cooling rate, solidification rate increases and therefore dendrites and cells will become finer. A relation is proposed by [9] for secondary dendrite arm spacing and cooling rate:

$$SDAS = at_f^n = b(\epsilon)^{-n} \quad [9] \quad (1.5)$$

Where SDAS is secondary dendrite arm spacing , t_f the time elapsed from the beginning to the end of solidification, ϵ is cooling rate, a and b are proportional constants. As shown in Figure 1.24 dendrite growth is time depended. Therefore by increasing cooling rate the time available for dendrites growth is decreased [9].

Weld penetration is an important factor which determines the mechanical resistance of the weld metal. Weld penetration profile depends on heat input per unit length and weld geometry. As shown in Figure 1.25, researches introduce different criteria to measure the weld penetration in T-joints. Wei Liu et al. measured the width of weld face, the throat, the leg and height [47] while Z.B Yang et al. considered the depth and seam angle as criteria for weld penetration [48].

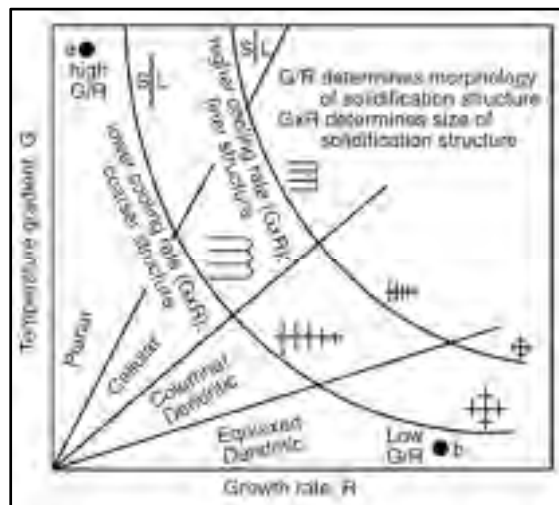


Figure 1.23 Effect of temperature gradient and growth rate on solidification pattern.

Taken from Kou. (2003, p.166)

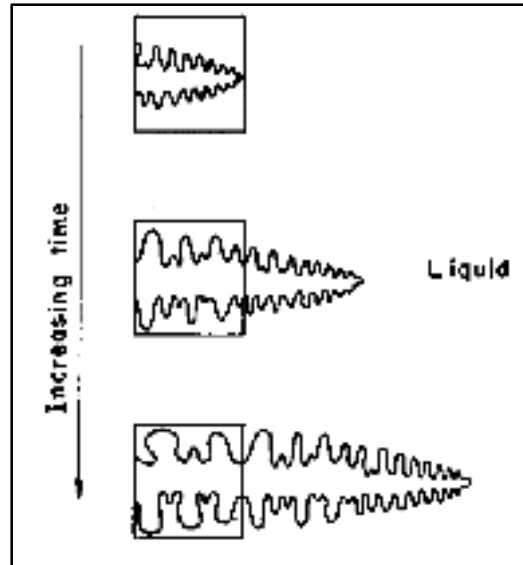


Figure 1.24 Schematic illustration of dendrites growth as a function of solidification time.

Taken from Kou. (2003, p165)

Weld penetration can also be presented as ratio of the depth to width (D/W) which is an important factor contributing to hot cracking. As shown in Figure 1.26, the bigger is the D/W, the higher will be the probability of the low melting compounds to be trapped in weld metal [24]. Increaseing H, leads to more base metal and filler metal melted in a constant length and therefore the probability of trapping of low melting compounds will be increased. The following relation is proposed to design a less risky filet weld configuration [49] :

$$\omega = \sqrt{\frac{H}{500}} \quad (1.6)$$

Where ω is the filet weld leg size (cm) and H is the heat input per unit length (KJ/cm).

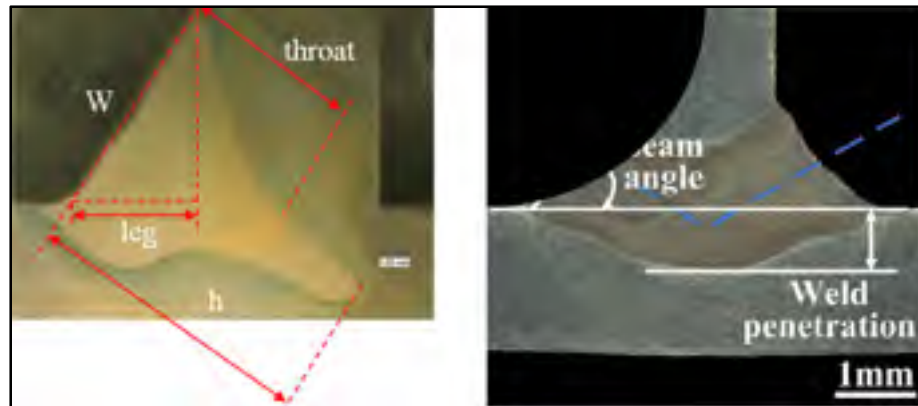


Figure 1.25 Examples of penetration measurement on T-joint welds
Taken from Liu et al. (2014, p.2824) and Yang et al. (2012, p.654)

Residual stress on the welding with lower H has been reported to be significantly higher compared to those welded with higher H due to existence of bainite and Widmanstätten ferrite [50]. Also, hardness maps on a HSLA steel weld metal with different heat input per unit length shows that the specimens with lower H have higher hardness as a result of higher cooling rates and therefore finer grain size. Furthermore, higher cooling rate leads to the formation of bainite and Widmanstätten ferrite rather than acicular ferrite [50]. Cooling the workpiece between the passes will decrease the heat built-up and therefore decreases residual stresses [45].

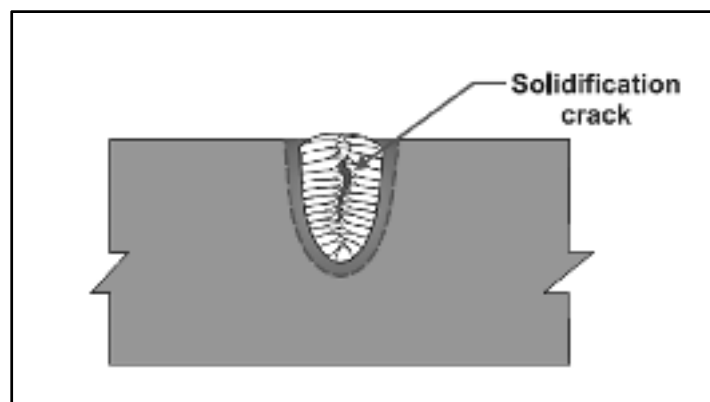


Figure 1.26 Schematic illustration of susceptibility to hot cracking in high ratio of D/W.
Taken from Welding for design engineers (2007, p.227)

Hot cracking is not necessarily the result of one of the above mentioned root causes. One or more causes can coexist together to form a hot crack. This makes it challenging and sometimes misleading to investigate the hot cracking root causes.

Hot cracking theories

Various theories have been introduced to explain hot cracking. Different researches have considered some factors and ignored some others. Although these theories can not describe all the phenomena contributing in hot cracking but study of some of them can help to have a better understanding and discuss some of the factors which contribute to hot cracking observed in the current work. Three of the well-known theories are explained in this chapter.

Technological strength theory

This theory developed by Porkhorov is based on three facts: 1) ductility is reduced by reducing the temperature, 2) negative volume changes while liquid to solid transformation lead to deformation which is called internal strain, 3) restraint during welding causes external strain. The theory introduces a Brittle Temperature Range (BRT) within which, the ductility of the weld metal is reduced by temperature. This range starts from somewhere below the liquids and continued till below the solidus temperature. Cracking occurs if the sum of internal and external strains overcomes the ductility [51].

As shown in Figure 1.27, P_{\min} is the lowest possible ductility for a specific weld metal. Then a safety margin is defined as:

$$\epsilon_{\text{red}} = P_{\min} - (\epsilon_{\text{int}} + \epsilon_{\text{ext}}) \quad (1.7)$$

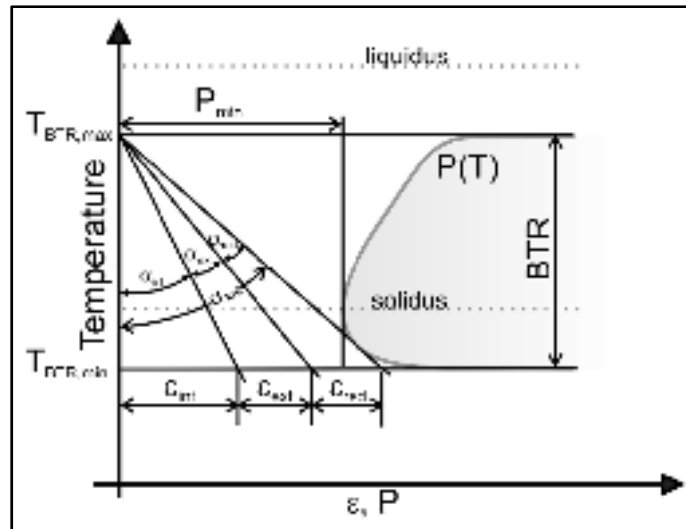


Figure 1.27 Schematic illustration of the technological strength theory.
Taken from Kannengiesser et al. (2014, p.399)

The higher is the safety margin, the lower will be the susceptibility to hot cracking. Critical strain can be shown as:

$$\frac{d\varepsilon}{dT} = \frac{\frac{d\varepsilon}{dt}}{\frac{dT}{dt}} \quad (1.8)$$

Rate of feeding-shrinkage theory

Rate of feeding-shrinkage theory as illustrated in Figure 1.28 is based on competition between rate of feeding and rate of shrinkage during the solidification. During the solidification, dendrites are growing and liquid metal should feed the spaces between dendrites. At the same time, solidification is accompanied by shrinkage. Hot cracking occurs if the rate of feeding can not reach the rate of shrinkage. This theory has two drawbacks: 1) the mechanical effects are completely disregarded. 2) calculation of rate of feeding is challenging. Therefore, in practice it is difficult to analyze the susceptibility to hot cracking just based on this theory. As this theory is based on capability of melt to feed the

interdendritic spaces, it recommends shortening of dendrites size and reducing contamination to avoid hot cracking [27].

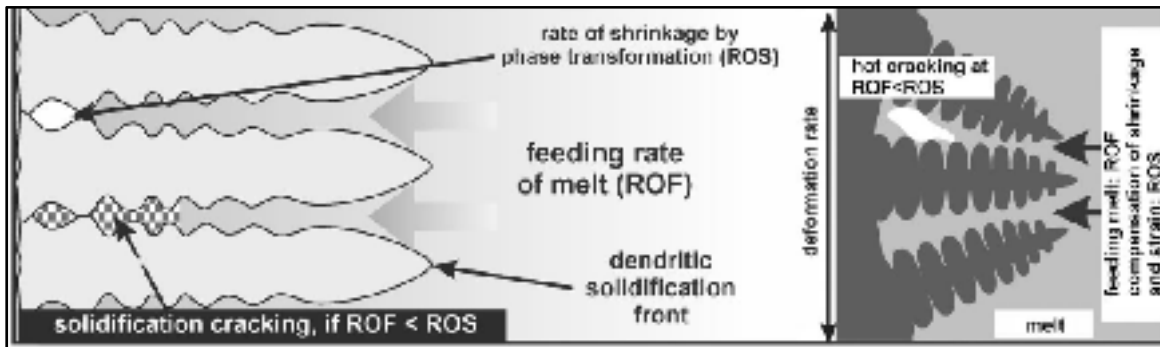


Figure 1.28 Schematic illustration of the rate of feeding-shrinkage theory.
Taken from Kannengiesser et al. (2014, p.400)

Rappaz-Drezet theory

Figure 1.29 shows a schematic explanation of Rappaz-Drezet theory which was introduced by M. RAPPAZ et al [52]. This theory discusses the hot cracking based on two factors: 1) tensile strain perpendicular to dendrite growth; 2) interdendritic liquid feeding. Rappaz-Drezet theory introduces a critical strain in relationship with melt pressure. If the deformation passes the critical strain and melt pressure drops, the first void will be nucleated [52].

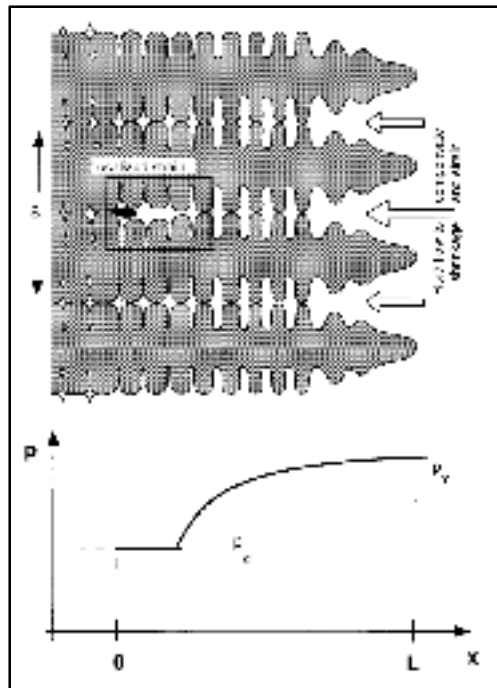


Figure 1.29 Schematic of hot cracking explained by Rappaz-Drezet theory.
Taken from Rappaz, Drezet et al. (1999, p.451)

Preventive methods

Different methods have been proposed to prevent hot cracking. As the main root cause of hot cracking is the tensile stress on weld centerline during the solidification, a suitable preheating has an important effect on reducing the susceptibility to hot cracking. Reducing the restraint is one of the most effective actions which is always recommended for all welded structures [9].

As already discussed, low melting point compounds are one of the most important factors contributing to hot cracking. In order to reduce susceptibility to hot cracking, it is highly recommended to control the chemical composition of both base and filler metals. S in weld metal can increase the susceptibility to hot cracking. Detrimental effect of S can be explained by formation of low melting point FeS. To reduce the probability of FeS formation, it is

recommended to increase Mn content in weld metal chemical composition and therefore produce high melting point MnS in expense of the low melting point FeS [9]. Increasing the Mn/S ratio is effective only on low carbon steels. When carbon content exceeds 0.3 wt%, improvement in this ratio does no longer help to reduce hot cracking susceptibility. Figure 1.30 illustrates the effect of Mn/S ratio combined with effect of carbon [9].

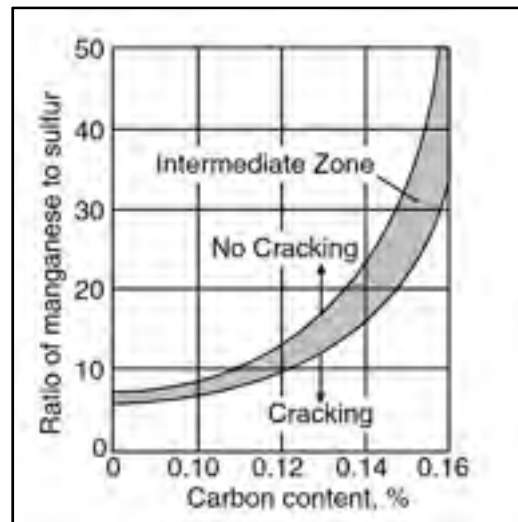


Figure 1.30 Effect of Mn/S ratio combined with effect of carbon in welding of carbon steels
Taken from Kou(2003, p.288)

As the root pass has more dilution with the base metal, using high carbon filler metal may lead to increase significantly the carbon content in weld root compared to further passes. In welding of high carbon steels, it is recommended to weld the root pass with a low carbon filler metal to avoid high carbon content in weld root [9]. Carbon also is reported to increase the width of solidification range. Apart from this fact, low carbon composition is always preferable because of detrimental effect of carbon on toughness. Higher carbon content can also increase the hardenability. However, austenite grain size and alloying elements play also an important role [53]. Many researches have proposed carbon equivalent (CE) formula for different steel grades and microstructures. Talaş, Ş. [54] has assessed the different formulas proposed for CE in prediction of mechanical properties of steel weld metals. He calculated a

correlation coefficient between each formula and various microstructures in weld metal. According to his findings the best correlated formula for acicular ferrite is:

$$C + (Mn/6) + (Si/24) + (Mo/29) + (V/14) \quad [54] \quad (1.9)$$

Reducing the carbon content may not always be recommended. M_s temperature increases by decreasing the carbon content and therefore higher preheating temperature would be needed to optimize the solidification rate which in turn can affect significantly the base metal microstructure [38].

Applying a buttering layer on first pass can help to avoid high carbon content. Buttering is an intermediate layer on base metal which has usually different chemical composition from both base and weld metal. Buttering layer is used when avoiding direct dilution of base and weld metal is desired. Application of buttering layer with a Ni-Fe filler metal has been reported to reduce the susceptibility to hot cracking in welding of a low ductility steel [39].

Control of microstructure can help to reduce susceptibility to hot cracking. Acicular ferrite is a desirable microstructure in HSLA steel weld metal. Addition of Mo and Ni to powder in SAW of HSLA steel has been found to reduce the fracture appearance transition temperature (FATT) thanks to increase of the volume fraction of acicular ferrite in weld metal [17]. Imposing the solidification from ferrite rather than austenite is another general method to reduce the susceptibility to hot cracking. Modification of chemical composition to obtain ferrite stabilizers rather than austenite stabilizer is recommended [38]. This is not always feasible due to desired effects of the alloying elements which could be austenite stabilizers. As shown in Figure 1.31a, it is recommended to avoid tear-shaped weld pool which produces perpendicular dendrites. Oval shaped weld pool as shown in Figure 1.31b is less susceptible to hot cracking due to the formation of non perpendicular dendrites. As shown in Figure 1.31c one of the desired microstructures is having equiaxed grains in centerline of the weld. Magnetically oscillated welding as shown in Figure 1.31d is proposed to prevent the crack propagation in weld metal by forcing the crack to change its direction [55].

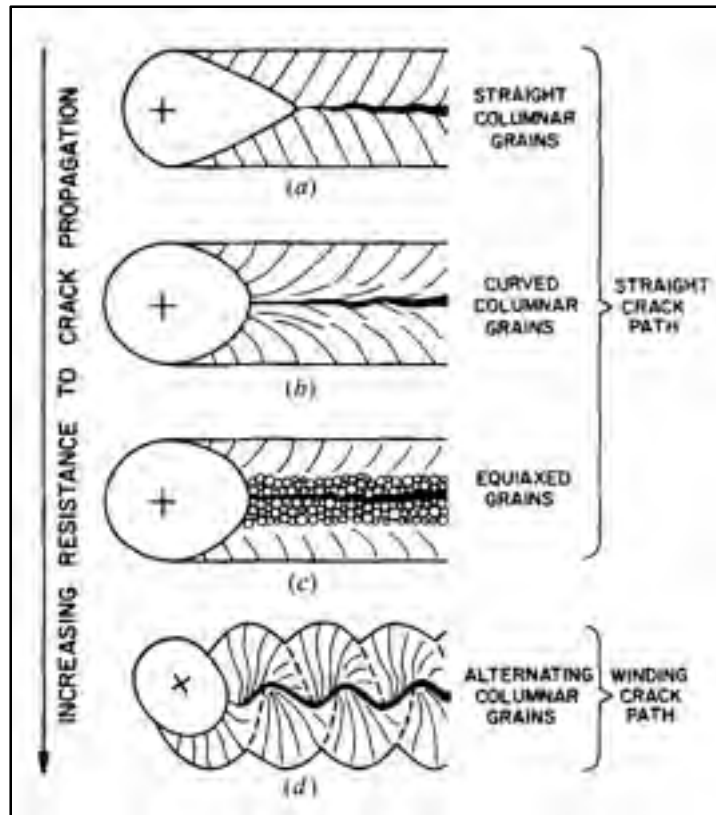


Figure 1.31 Susceptibility to hot cracking for different weld patterns a) tear-shaped weld pool with perpendicular dendrites, b) oval shaped weld pool with non perpendicular dendrites, c) equiaxed grains at centerline of the weld and d) effect of arc oscillation in crack propagation at centerline of the weld

Taken from Kou et al. (1985, p.1888)

Although welding position and fluctuation in welding angle depends on welding technology and limitations due to workpiece, but it would be helpful to keep relatively equal heat flow to both parts as well as reducing arc angle fluctuation during welding. This will help to avoid high D/W ratio which dramatically contributes in susceptibility to hot cracking [24].

Avoiding concave weld face is another recommended remedy for hot cracking. As illustrated in Figure 1.32, the surface of a concave weld pass is subjected to higher tensile stress

compared to convex pass. However excessive convexity on surface of the weld can induce stress concentration and lead to fatigue cracking [9].

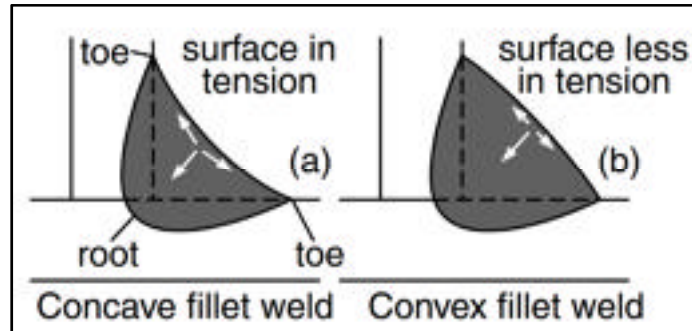


Figure 1.32 Effect of weld face geometry on stress concentration
Taken from Kou (2003, p.294).

All the above mentioned methods are general remedies recommended in the literature. However, specific study must be fulfilled on each alloy and welding conditions to find out which of the above mentioned methods are effective and applicable.

CHAPTER 2

MATERIALS AND METHODS

2.1 Base metals

Two grades of HSLA steels have been used for investigations in the current study: ASTM A572 Gr.50 and ASTM A656 Gr.80. In some parts of the current work the words Gr.50 and Gr.80 are used instead of ASTM A572 Gr.50 and ASTM A656 Gr.80 respectively.

2.1.1 ASTM A572 Gr.50

According to ASTM standard, ASTM A572 contains Nb, V and N. Various grades for ATSM A572 are introduced by ASTM standard. Gr.50 in the current work has a minimum yield strength of 50Ksi (345 MPa). Table 2.1 and Table 2.2 summarize the mechanical properties and chemical composition of the Gr.50 base metal.

Table 2.1 Mechanical properties of ASTM A572 Gr.50 [8].

Re MPa (Ksi)	Rp MPa (Ksi)	%A (8 in, 20.32 cm)	%A (2 in, 5.08 cm)
345 (50)	448 (65)	20	24

Table 2.2 Chemical composition of ASTM A572 Gr.50 (wt%).

C	Mn	P	S	Si	Al	Cu
0.06	1.40	0.015	0.003	0.14	0.03	0.29
Ni	Cr	Mo	Nb	V	Ti	
0.16	0.16	0.05	0.045	0.008	0.013	

2.1.2 ASTM A656 Gr.80

ASTM A656 is also introduced by ASTM in various grades. The grade which is used in the current work is Gr.80 which has a minimum yield strength of 80 Ksi (550 MPa). Table 2.3 summarizes the mechanical properties of this base metal.

Table 2.3 Mechanical properties of ASTM A656 Gr. 80 [56].

Re MPa (Ksi)	Rp MPa (Ksi)	%A (8 in, 20.32 cm)	%A (2 in, 5.08 cm)
552 (80)	621 (90)	12	15

Table 2.4 shows the chemical composition of the Gr.80 base metal provided by the manufacturer.

Table 2.4 Chemical composition of ASTM A656 Gr.80 (wt%).

C	Mn	P	S	Si	Al	Cu
0.05	1.59	0.015	0.003	0.25	0.04	0.41
Ni	Cr	Mo	Nb	V	Ti	Sn
0.26	0.19	0.21	0.088	0.010	0.031	0.012
N	B					
0.114	0.0003					

2.2 Filler metals

Five different filler metals used for the experiments that are categorized into three groups: low, medium and high nickel. The diameter of all the filler metals is 1.14 mm (0.045 in).

Table 2.5 Filler metals used for Gr.50 and Gr.80.

Base	Low nickel	Medium nickel	High nickel
Gr.50	ESAB S-6	Hobart Fabcor E80C-Ni1	Selectarc 80C Ni2
Gr.80	ESAB S-6	Blueshield 100C MG	Hobart Fabcor 80C-N2

2.2.1 ESAB S-6 (low nickel for both Gr.50 and Gr.80)

According to the manufacturer, ESAB S-6 is a solid wire with copper coating designed for manual and semiautomatic GMAW welding. It is classified as AWS A5.18, ER70S-6. The chemical composition of non-diluted weld for the filler metal according to the manufacturer test report is shown in Table 2.6. Mechanical properties of the weld metal for this filler according to the manufacturer are shown in Table 2.7.

Table 2.6 Chemical composition of non-diluted weld for filler metal ESAB S-6 (wt%).

C	Mn	P	S	Si	Cu	Ni
0.07	1.53	0.017	0.012	0.90	0.02	0.02
Cr	Mo	Al	V	Ti+Zr		
0.01	0.02	<0.001	<0.01	<0.01		

Table 2.7 Mechanical properties of weld for ESAB S-6 welded using 75% Ar - 25% CO₂.

R _e MPa (Ksi)	R _p MPa (Ksi)	A%	Charpy impact at -29°C (-20°F) Joule (ft.lbf)
483 (70)	579 (84)	26	91 (67)

2.2.2 Hobart Fabcor E80C-Ni1 H8 (medium nickel for Gr.50)

This filler metal is classified as AWS A5.28-96, ASME SFA5.28. Chemical composition of non-diluted weld and mechanical properties of weld according to the manufacturer are summarized in Table 2.8 and Table 2.9 respectively.

Table 2.8 Chemical composition of non-diluted weld for Hobart Fabcor E80C-Ni1 H8 (medium nickel for Gr.50) (wt%).

C	Mn	P	S	Si	Cu	Ni
0.06	1.15	0.009	0.011	0.38	0.05	1.09
Cr	Mo	V				
0.09	0.11	<0.01				

Table 2.9 Mechanical properties of weld for Hobart Fabcor E80C-Ni1 H8 welded using 95% Ar - 5% CO₂.

R _e MPa (Ksi)	R _p MPa (Ksi)	A%	Charpy impact at -45.5°C (-50°F) Joule (ft.lbf)
607 (88)	655 (95)	26	76 (56)

2.2.3 Selectarc 80C Ni2 (high nickel for Gr.50)

This filler metal is classified as AWS A5.28, SFA 5.28. Table 2.10 and Table 2.11 indicate the chemical composition of non-diluted weld and mechanical properties of the weld presented by the manufacturer respectively.

Table 2.10 Chemical composition of non-diluted weld for Selectarc 80C Ni2 (wt%).

C	Mn	P	S	Si	Cu	Ni
0.04	1.06	0.009	0.007	0.30	0.03	2.15
Cr	Mo	V				
0.04	<0.04	<0.01				

Table 2.11 Mechanical properties of weld for selectarc 80C Ni2.

R _e MPa (Ksi)	R _p MPa (Ksi)	A%	Charpy impact at -62°C (-80°F) Joule (ft.lbf)
496 (72)	593 (86)	24	27 (20)

2.2.4 BLUSHIELD LA 100C MG (medium nickel for Gr.80)

BLUSHIELD LA 100C MG is classified as AWS A.5.28 E100C-G-H8. The chemical composition of non-diluted weld and mechanical properties of the weld metal according to the manufacturer are shown in Table 2.12 and Table 2.13, respectively.

Table 2.12 Chemical composition of non-diluted weld for BLUSHIELD LA 100C MG (wt%).

C	Mn	P	S	Si	Ni	Cr
0.05	1.48	0.01	0.007	0.30	1.99	0.22
Mo	B					
0.52	0.002					

Table 2.13 Mechanical properties of weld for BLUSHIELD LA 100C MG.

R _e MPa (Ksi)	R _p MPa (Ksi)	A%	Charpy impact at -40°F (-40°C) Joule (ft.lbf)
648 (94)	752 (109)	21	41 (30)

2.2.5 Hobart Fabcor 80C-N2 (High nickel for Gr.80)

Hobart Fabcor 80C-N2 is classified as AWS A5.28 E80C-Ni2 H4. Table 2.14 and Table 2.15 show the chemical composition of non-diluted weld and mechanical properties of the weld metal according to the manufacturer respectively.

Table 2.14 Chemical composition of non-diluted weld for Hobart Fabcor 80C-N2 (wt%).

C	Mn	P	S	Si	Ni	Cr
0.063	0.91	0.008	0.010	0.37	2.39	0.06
Mo	Cu	V	B			
0.007	0.03	0.003	0.0004			

Table 2.15 Mechanical properties of weld for BLUSHIELD LA 100C MG.

R_e MPa (Ksi)	R_p MPa (Ksi)	A%	Charpy impact at -80°F (-62°C) Joule (ft.lbf)
552 (80)	627 (91)	24	52 (38)

2.3 Welding process

The welding process used in this work is Gas Metal Arc Welding (GMAW). In this method as shown in Figure 2.1, the weld is applied by initiating an arc between base metal and a filler wire electrode which is continuously fed through a welding gun, the protection of the weld zone from atmospheric contamination is provided by a continuous stream of shielding gas or gas mixture. Traditionally this process was being used for aluminum using inert gas for protection (Metal Inert Gas). In welding of steel, it is highly recommended to have carbon dioxide and/or oxygen present in the shielding gas mix. In the current work, as recommended by the manufacturers of the filler metals, a mix of %85 argon and %15 CO₂ is employed for all the welds. The term MAG (Metal Active Gas) is specifically used in European countries when a portion of protective gas is CO₂. However, in North America a more generic wording (GMAW) is often used [24]. In this work, the term GMAW is used for our specific process which contains 85% Ar and 15% CO₂.

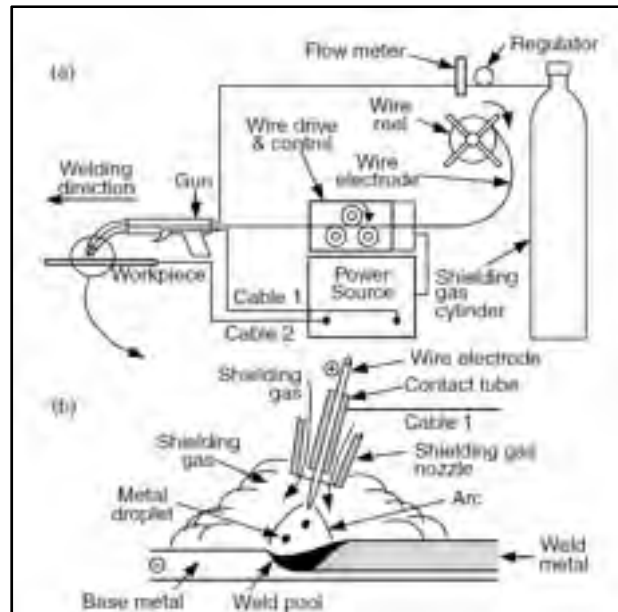


Figure 2.1 Gas Metal Arc Welding; a) overall process; b) enlarged welding area
Taken from Kou. (2003, p.20)

Like common procedures in GMAW, the voltage is kept constant during the welding. Direct current (DC) with electrode positive (EP) is applied to all welds. The factor which controls amperage is the electrode melting rate (wire feeding speed) and the voltage is closely controlled by arc length. In case of a change in the arc length for example while moving the gun toward or away from the workpiece, the power source responds by changing the current output. The power source is constantly responding to the changing demands of the arc. For the process to operate in a stable manner, the power source must be capable to respond correctly to the fluctuation of arc length [9]. High deposition efficiency, elimination of slag chips (as there is in MMAW), low hydrogen deposit and easiness of learning for operators, makes the GMAW a widely used process. However, difficulties and problems in windy conditions and more chance of lack of fusion can be named as drawbacks of this technic [9].

CHAPTER 3

RESULTS AND DISCUSSION

3.1 Characterization of the base metals

3.1.1 ASTM A572 Gr.50

Microstructure of ASTM A572 Gr.50 base metal is shown in Figure 3.1a. It contains equiaxed ferrite grains coexisting with pearlitic bands. The microstructure shown in Figure 3.1a is in agreement with those found in literature and shown in Figure 1.1. Equiaxed ferrite is one of the most common morphologies of ferrite in hot rolled steels which are fully recrystallized [6]. The fine grain size of equiaxed ferrite is the result of normalizing after hot rolling [7]. Based on the iron-carbon equilibrium diagram, ferrite is a phase with carbon content less than 0.02 wt%. As the carbon content of ASTM A572 Gr.50 is about 0.06 %wt, the excess carbon in equilibrium condition forms pearlitic bands. These pearlitic bands have been reported to be dissolved in austenite during thermal cycle of welding and consequently transformed to hard martensite after cooling [57]. Some rectangular shape particles were also observed in the matrix shown in Figure 3.1b in as-polished state which are assumed to be complex carbonitrides according to the literature [8]. These particles cannot be detected on etched samples even under SEM.

The result of thermodynamic calculations shown in Figures 3.2 and 3.3 confirm that under equilibrium conditions the predominant phase in Gr.50 alloy is ferrite. These calculations also support the assumption of complex carbonitrides M (C, N) formation which was presented in Figure 3.1b.

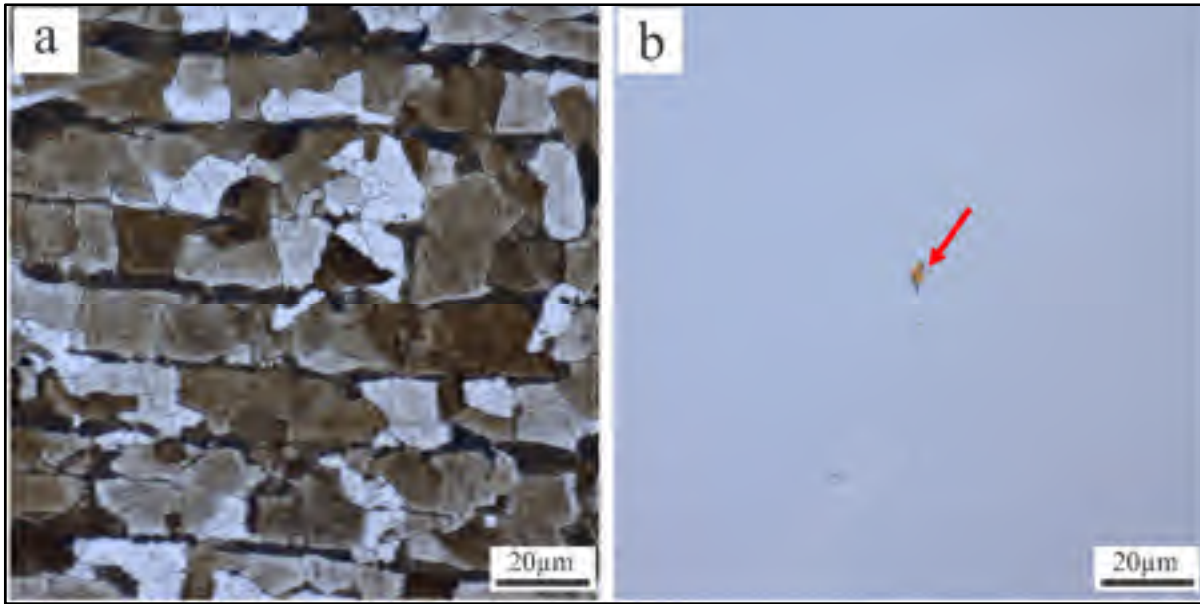


Figure 3.1 Optical microstructure of as received ASTM A572 Gr.50; a) equiaxed ferrite coexisting with pearlitic bands (hot etched), b) complex carbonitride particle (as polished).

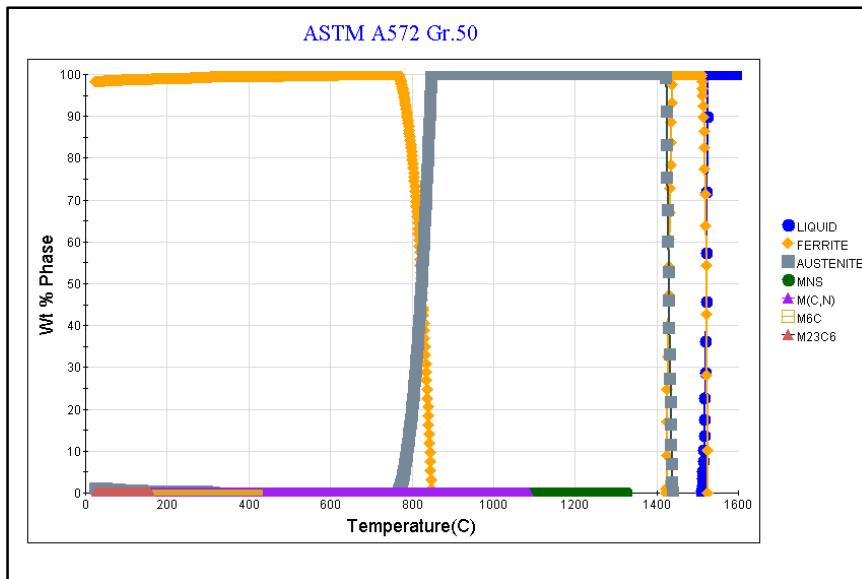


Figure 3.2 Thermodynamic calculation for equilibrium phases in Gr.50 base metal.

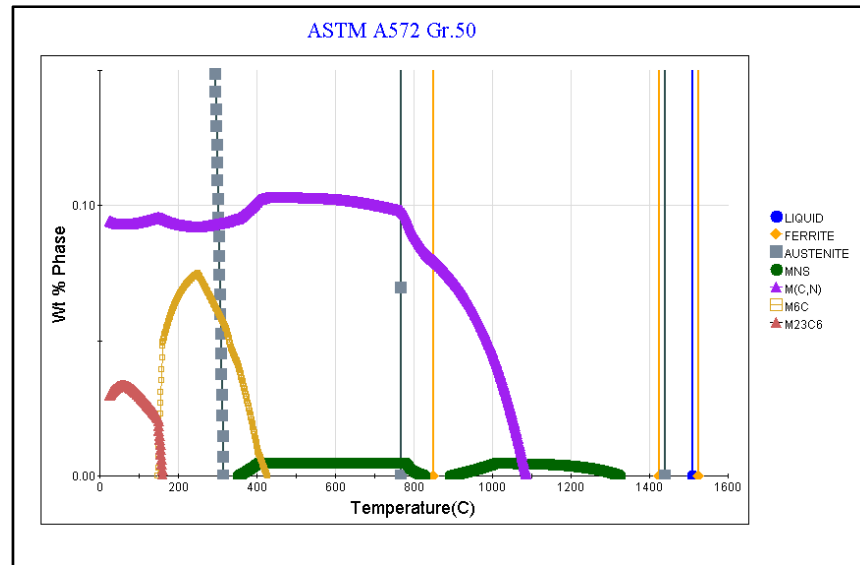


Figure 3.3 Thermodynamic calculation for equilibrium phases in Gr.50 base metal in high magnification to reveal low content phases.

As mentioned in Table 2.2, the Nb, V and Ti content of Gr.50 base metal is 0.045, 0.008 and 0.013 wt%, respectively. This confirms that the M(C,N) particles shown in thermodynamic calculation results (Figure 3.3) and revealed on as polished microstructure (Figure 3.1b) are complex carbonitrides containing Nb, V and Ti. However, the chemical analysis of carbonitrides in Gr.50 base metal was not feasible by the methods applied in current work due to difficulty of their observation under SEM.

3.1.2 ASTM A656 Gr.80

As shown in Figure 3.4a the microstructure of ASTM A656 Gr.80 base metal consists of ferrite grains. The effect of primary hot rolling process is observed as deformed ferrite grains. This indicates that the base metal has not been fully recrystallized after rolling. The rectangular shape particles, with the same shape and size as in Gr.50 base metal are distributed in the matrix. The abundance of these particles seems to be more in Gr.80 base metal compared to Gr.50. The particles in Gr.80 are clearly visible under SEM as shown in

Figure 3.4b. Thus, in contrast to Gr.50 base metal, the chemical analysis of the particles was feasible using EDS.

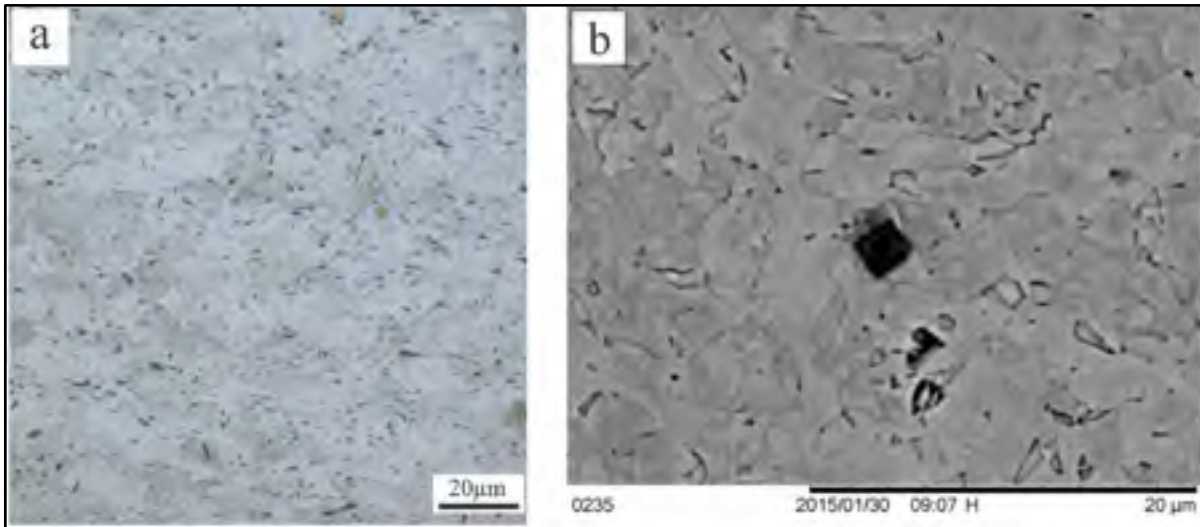


Figure 3.4 Microstructure of Gr.80 base metal; a) ferrite grains with complex carbonitrides , b) SEM image of a complex carbonitride (hot etched).

The chemical analysis with EDS shown in Figure 3.5 confirms that the rectangular particles in Gr.80 base metal are complex carbonitrides of Nb, V and Ti. Regarding the similarity of shape and size of these particles in both base metals, the same chemical composition is expected for Gr.50 particles as well. As shown in Table 2.4, the Nb, V and Ti content of Gr.80 base metal is 0.088, 0.010 and 0.031 wt%, respectively. The sum of microalloying elements (Nb +V+Ti) in Gr.80 base metal is 0.129 wt% while it is 0.066 wt% for Gr.50 base metal. Comparison of the N content of Gr.50 and Gr.80 base metals (Tables 2.2 and 2.4) shows that Gr. 80 contains higher percentage of N. The higher percentage of N as well as higher content of microalloying elements leads to formation of more nitrides. The abundance of carbonitrides in Gr.80 base metal compared to Gr.50 confirms the above analysis. The results indicate enrichment of Al, Mg and O in particles' core which is representative of an oxide inclusion surrounded by carbonitrides. These oxides could be originated from primary deoxidation stage [58] or the refractory materials used during the melting process [59, 60]. These oxides are potential sites for heterogeneous nucleation of subsequent carbonitrides. A

similar mechanism for the formation of the Ti-rich inclusions on aluminum oxide has been reported both numerically and experimentally by [61, 58].

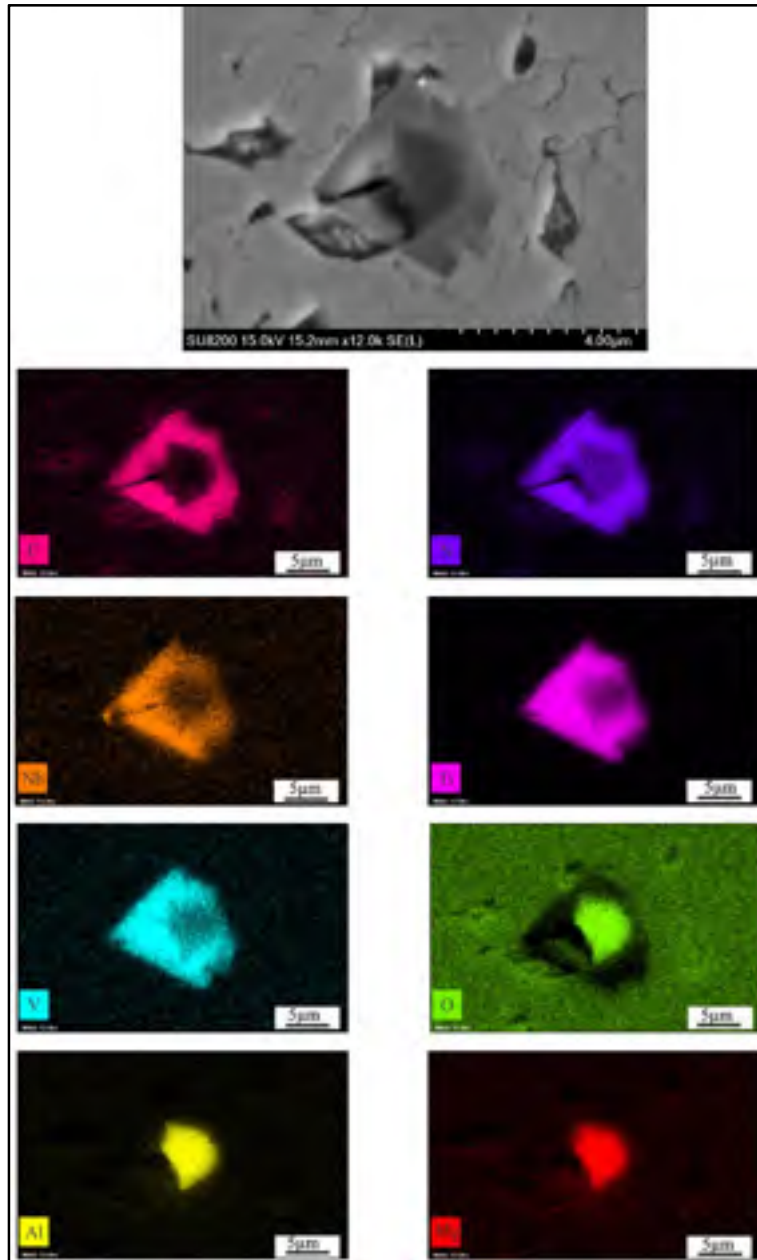


Figure 3.5 EDS analysis on complex carbonitrides of Gr.80 base metal.

Figures 3.6 and 3.7 show the equilibrium phases calculated for ASTM A656 Gr. 80 based on chemical composition in Table 2.4 which confirms the formation of complex carbonitrides below 1000°C. Although according to the thermodynamic calculations, formation of MnS and BN is also probable but no evidence was found to confirm their presence in the base metal.

Comparing the microstructure of base metals in Figures 3.1 and 3.4, Gr.80 base metal which has not been recrystallized is assumed to contain higher amount of residual stresses [62]. Although the heat transferred during welding releases the residual stresses in HAZ but a portion of residual stresses can be remained at the zones which are not affected by heating. Thus, less stress can be accommodated by Gr.80 base metal during the welding and a portion of the stress will be imposed to the weld metal. On the other hand, the yield strength of the Gr.80 is higher than the Gr.50. Therefore, more stress is expected to be transferred to the centerline of the Gr.80 weld.

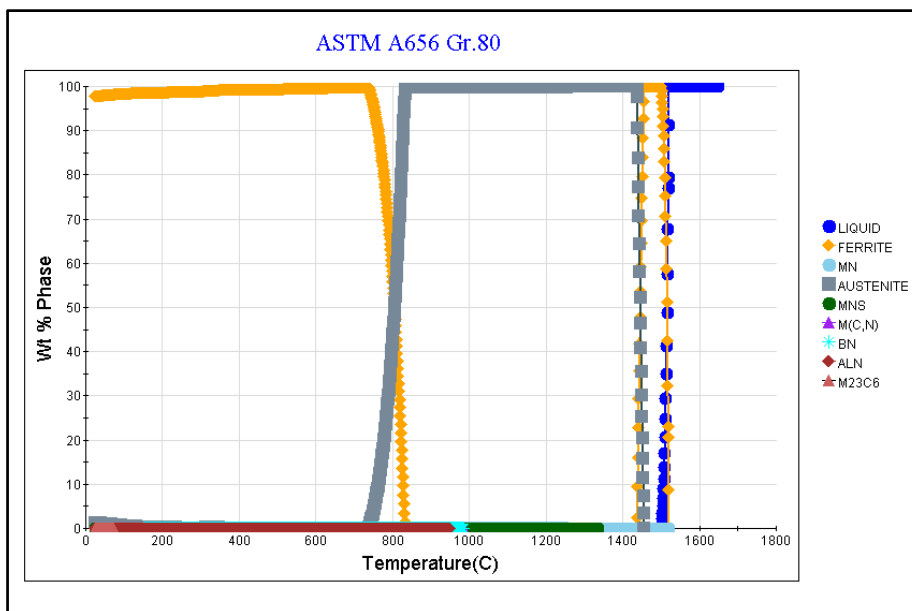


Figure 3.6 Thermodynamic calculation for equilibrium phases in Gr.80 base metal.

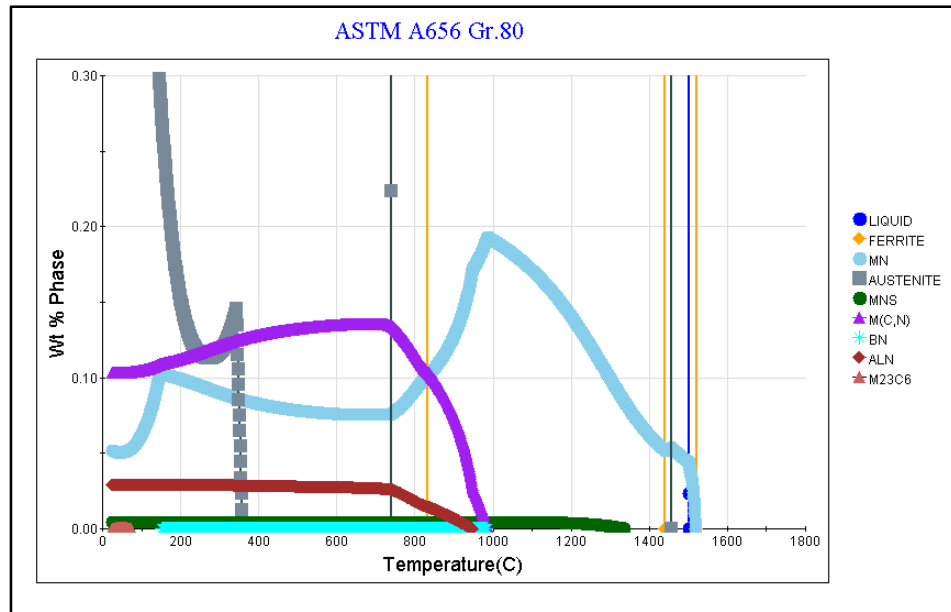


Figure 3.7 Thermodynamic calculation for Equilibrium phases in Gr.80 base metal in high magnification to reveal low content phases.

3.1.3 Physical properties

As physical properties of base metal especially linear expansion coefficient and thermal conductivity have an important role in welding processes, these parameters are calculated for both base metals as a function of temperature. As shown in Figure 3.8, there is a linear relation between thermal expansion coefficient and temperature while thermal conductivity changed semi-linearly as a function of temperature. There is an increasing trend of thermal expansion coefficient with temperature for both base metals except a sudden drop around 800°C which is correlated with eutectoid reaction. Thermal conductivity of both alloys shows an ascending trend from 0 to around 200°C and then descends by increase of temperature from 200°C. Descending trend continues till A_3 temperature where above there is no ferrite (852°C for Gr.50 and 835°C for Gr.80) and then thermal conductivity again increases as a function of temperature. The results indicate that linear expansion coefficient for both base metals is approximately similar. Conversely thermal conductivity of Gr.50 base metal in the range of 0-200°C is higher than the thermal conductivity of the Gr.80 base metal. This is in agreement with the model proposed by [63] which predicts the thermal conductivity of

diluted solutions as a function of chemical composition and temperature and confirms the highest thermal conductivity for pure iron. It is also reported that an important decrease occurs in thermal conductivity by adding Ni, Cr and Mn [63]. Knowing that the content of alloying elements in Gr.80 base metal is higher than Gr.50, higher thermal conductivity is expected for Gr.50 base metal compared to Gr.80. This model confirms also a semi-linear evolution for thermal conductivity as a function of temperature. Thermal conductivity affects significantly the microstructure of steel which is subjected to thermal cycles in welding [63].

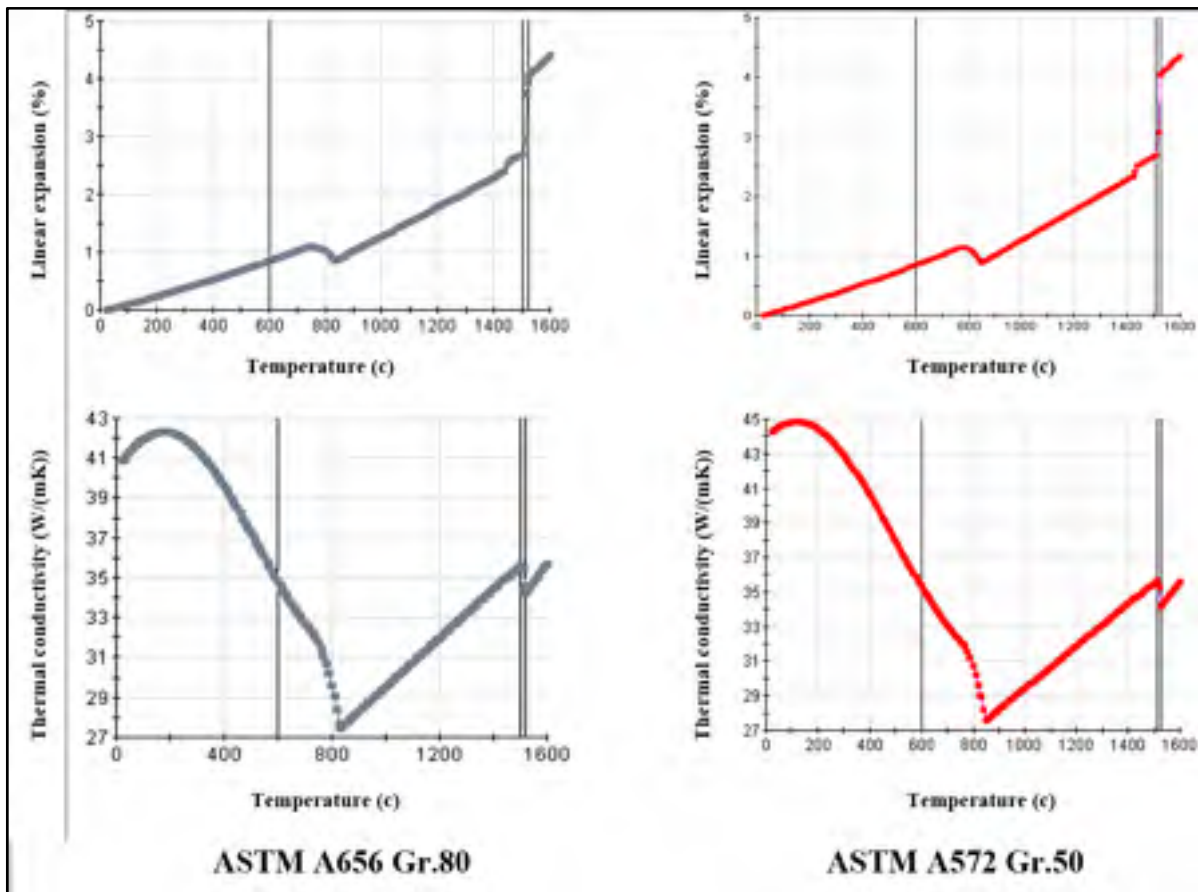


Figure 3.8 Calculation of base metals physical properties; a) linear expansion coefficient, b) thermal conductivity

3.2 Welding of specimens

Before starting the current work, a preliminary study was carried out based on the existing industrial process. Specimens were welded with different heat inputs, filler metals, base metals and weld configurations to investigate the hot cracking root causes. It was found that excessive penetration must be avoided as it increases the weld depth and therefore induces the susceptibility to hot cracking. Where excessive penetration is not avoidable, due to operational limitations, it was recommended to increase the nickel content in weld metal in order to enhance the solubility of Cu and therefore prevent low melting compounds microsegregations at weld centerline. This conclusion was mostly based on statistics rather than substantiation by metallurgical discussions. One of the justifications of the current work was to focus on metallurgical studies and find the link between microstructure, chemical composition, physical and mechanical properties with hot cracking.

The aim of the phase A of the current work was to further analyse the industrial results and optimum designation of experiments for the next steps. The welding parameters used for specimens of phase A are summarized in Table 3.1. Microstructure of base metal, weld metal and HAZ was revealed in phase A and the nature of hot cracking and its link with the microstructure was investigated. In order to investigate the effect of Ni on hot cracking prevention and also compare the susceptibility of Gr.50 and Gr.80 welds to hot cracking under the same conditions, a plan was implemented to carry out further experiments (phase B). Welding parameters for phase B specimens are summarized in Table 3.2. The welding position in the all specimens (phase A and phase B) is 2F and the mixture of shielding gas is 85%Ar-15%CO₂. Dimensions and configurations of workpieces in phase B are shown in Figure 3.9.

Table 3.1 Welding parameters for phase A workpieces prepared by the industrial party.

ID	Base metal	Filler metal	Joint	Thick (mm)	Gap (mm)	Voltage (V)	Current (A)	W.S (cm/min)
RC5	Gr.50	80C-	SB	12.7	2.03	31	unknown	unknown
L6	Gr.80	100MG	SB	12.7	1.52	30	285	48.26
L43	Gr.80	100MG	SB	12.7	1.52	30	300	50.8
L19	Gr.80	100MG	SB	12.7	1.52	30	310	45.72
BK2	Gr.80	100MG	BK	12.7	1.52	30	285	60.96
BK3	Gr.80	100MG	BK	12.7	1.52	30	310	40.64

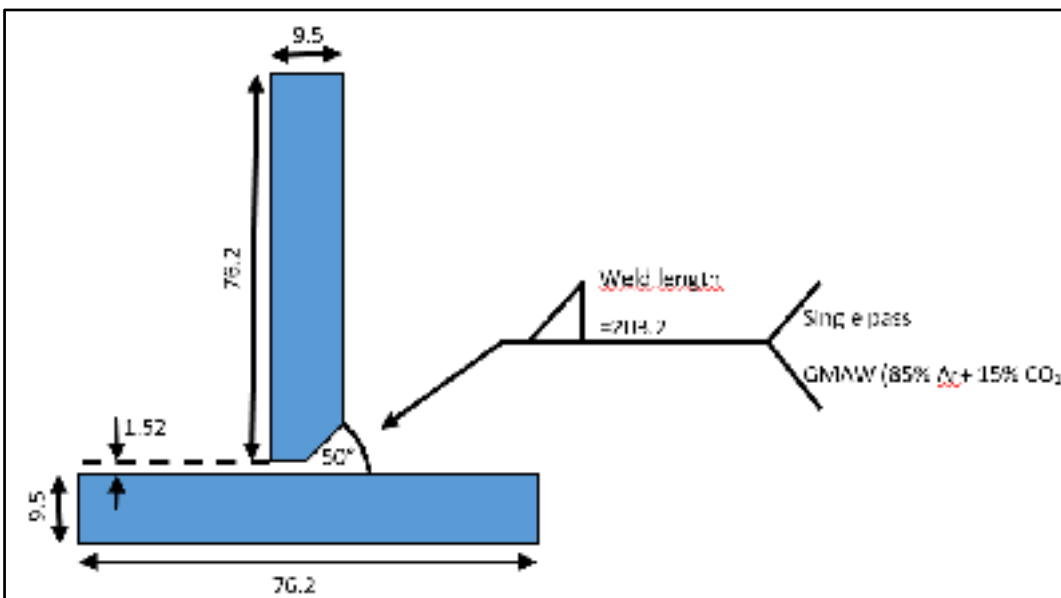


Figure 3.9 Weld configuration for phase B, All dimensions are in mm.

Two etching methods were employed to reveal the microstructures: 1) hot etching at 90-95°C using a solution of 40 gr NaOH + 60 gr H₂O + 15 gr NaNO₃. The etching time was 70 s for optical microscopy and 180 s for SEM, 2) 20 s etching with Nital 4%, rinsing with ethanol followed by secondary 15 s etching with the same solution.

Table 3.2 Welding parameters for phase B workpieces.

ID	Base metal	Filler metal	Joint	Tick (mm)	Gap (mm)	Voltage (V)	Current (A)	W.S (cm/min)
50-1	Gr.50	ESAB S-6	SB	9.525	1.52	27	250	40.64
50-4	Gr.50	E80C-Ni1 H8	SB	9.525	1.52	27	260	40.64
50-7	Gr.50	80C Ni2	SB	9.525	1.52	27	260	39.37
80-1	Gr.80	ESAB S-6	SB	9.525	1.52	27	250	43.18
80-4	Gr.80	100C MG	SB	9.525	1.52	27	275	40.64
80-7	Gr.80	80C-N2	SB	9.525	1.52	27	275	40.64

3.3 Characterization of the weld metal

3.3.1 Macroscopic studies on phase A welds

Initial observations indicated that most of the macrocrackings occur in specimens welded by Gr.80 base metal. Microstructural study of phase A specimens allowed determination of weld metal penetration and solidification profiles. As shown in Figure 3.10 macro hot cracking is observed in both BK2-1 and L6 which are welded by Gr.80. It is worth noting that the specimen L43 which is also welded by Gr.80 base metal does not indicate any macrocracking. However, this specimen contains a lack of penetration defect. No macrocracking was observed in Gr.50 welds. However, due to difficulty of differentiating between the sound centerline and microcracking with optical microscope, the soundness of Gr.50 welds couldn't be confirmed in phase A.

Dendritic solidification pattern is observed in all the specimens as the main grain morphology feature of weld metal. As shown in Figure 3.10 the dendrites are advanced opposite to the heat flow direction from two sides and meet at centerline of the weld where the crack appears. Comprehensive analysis of all the microstructures of the specimens revealed a link between dendrites orientation and crack size. As shown in Figure 3.10a, when

the dendrites deviate from perpendicularity against the centerline, the hot cracking is less likely to occur or is small in size, while as shown in Figure 3.10b, where the dendrites are perpendicular to the centerline, the crack is bigger in size. Although the weld shown in Figure 3.10c is not acceptable due to a lack of penetration, but as there is no perpendicular dendrites zone on this weld, no cracking appears at the centerline. Comparing the weld penetration in Figure 3.10c (lack of penetration) with other three welds, it can be assumed that the more is the penetration of the weld in base metal, the bigger is the perpendicular dendrites zone. As shown in schematic images in Figure 3.11 this can be explained by the variation of heat flow which is linked to the welding angle. When the welding angle is around 45° (Figure 3.11a), a low penetration or even lack of penetration is obtained. Conversely, an excessive penetration occurs when welding angle gets closer to 0° with a zone in the weld pool where the heat flow is perpendicular to the weld bead.

In all specimens, an equiaxed grain zone is observed at weld face. An example of these grains is illustrated in Figure 3.12 in a constitutive magnification. This equiaxed zone is observed on both single bevel and back plate configurations. It is worth to note that, as shown in schematic image illustrated in Figure 3.13, even in single bevel welds, an equiaxed zone occurs also in back face of the welds with excessive penetration. As schematically illustrated in Figure 3.13, equiaxed grains appear in a small portion of the fusion zone at weld face which has no direct contact with the base metal. Dendrites grow heterogeneously towards the centerline in the zones having direct contact with the base metal. Conversely, the equiaxed grains with no direct contact with the base metal solidify rapidly as a result of heat exchange with the shielding gas. Both growth rate and temperature gradient are expected to be different in weld face compared to the other zones in weld metal.

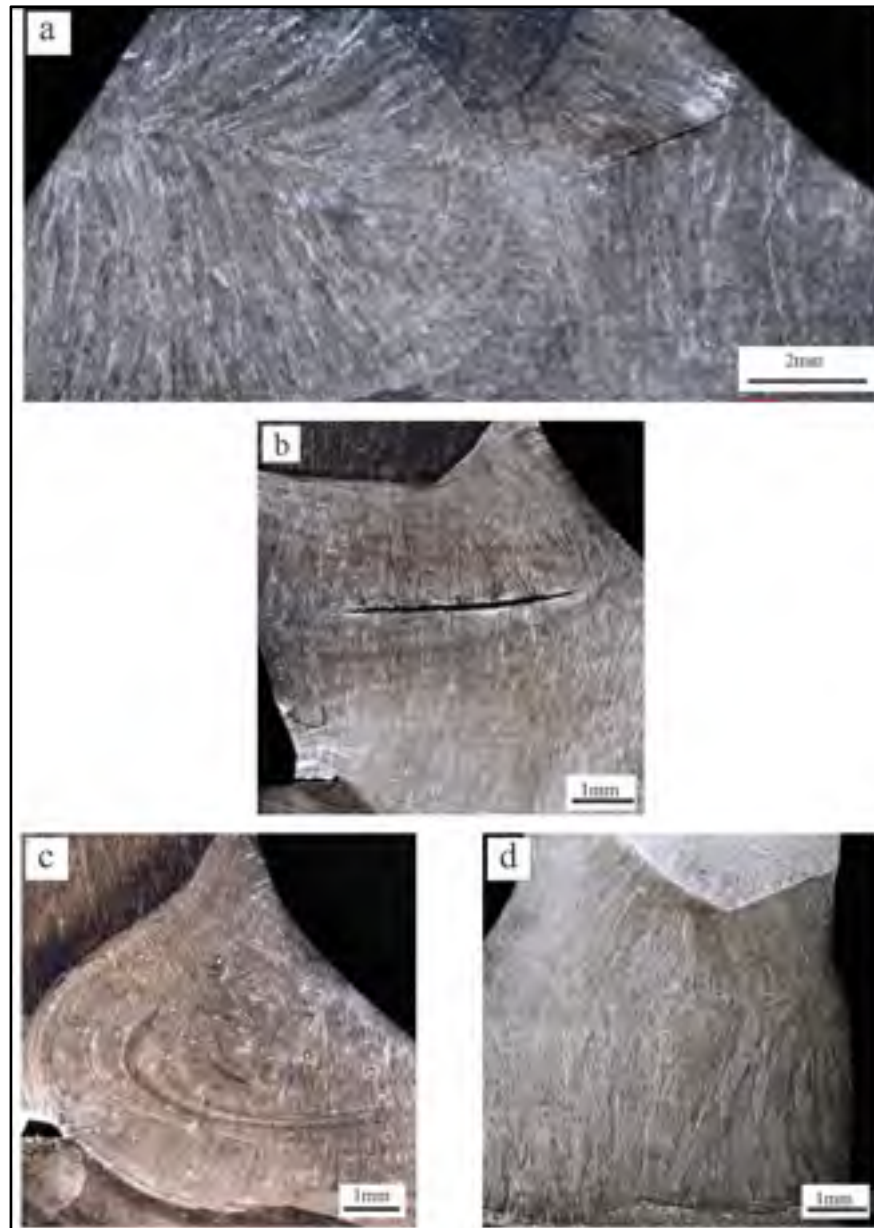


Figure 3.10 Examples of macrographic observations in phase A; a) macrocracking in a Gr.80 back plate weld (specimen: BK2-1), b) macrocracking in a Gr.80 single bevel weld (specimen: L6), c) lack of penetration in a Gr.80 single bevel weld (specimen: L43) and d) centerline in a Gr.50 single bevel weld with no macrocracking (specimen: RC5), all specimens are hot etched.

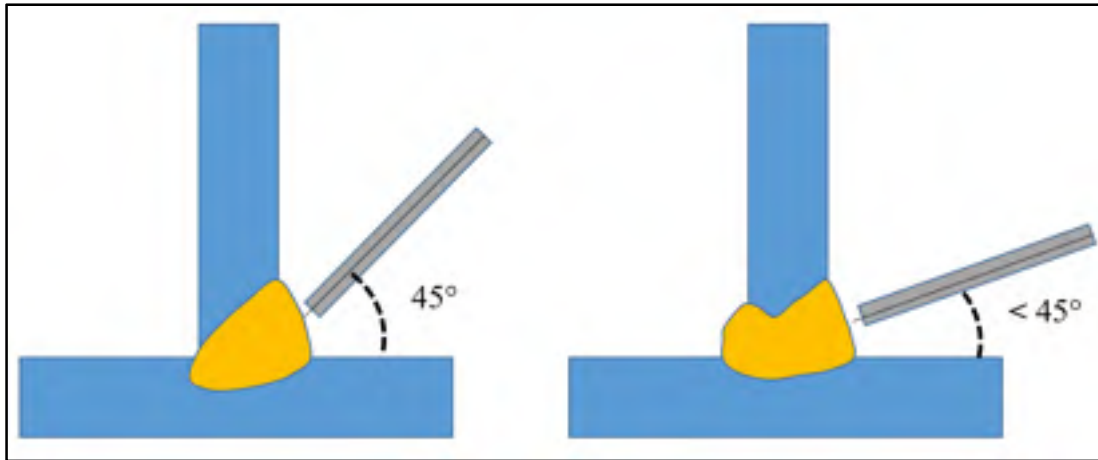


Figure 3.11 Schematic of relation between weld penetration and heat transfer directions resulted from welding angle. Heat transfer direction is illustrated by small arrows and welding angle is illustrated by big arrows; a) low penetration resulted from 45° welding angle, b) excessive penetration resulted from deviation in welding angle from 45° .

Comprehensive macrographic studies in phase A depicted the solidification pattern of the welds. This pattern has been discussed in terms of heat flow direction. It can be concluded that excessive penetration causes more perpendicular columns or dendrites and leads to hot cracking. On the other hand, care must be taken not to end up with lack of penetration. Therefore, an optimum value might be defined for penetration of the weld to avoid both hot cracking and lack of penetration defects.

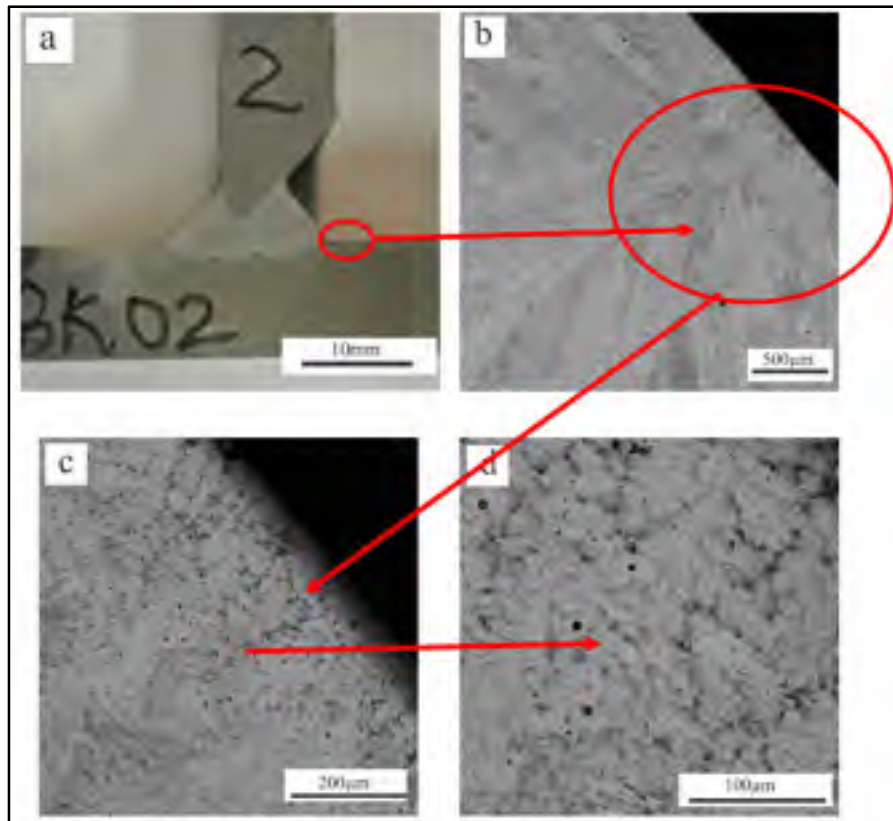


Figure 3.12 Constitutive magnification of equiaxed grains at weld face form a to d (specimen: BK2-2, hot etched).

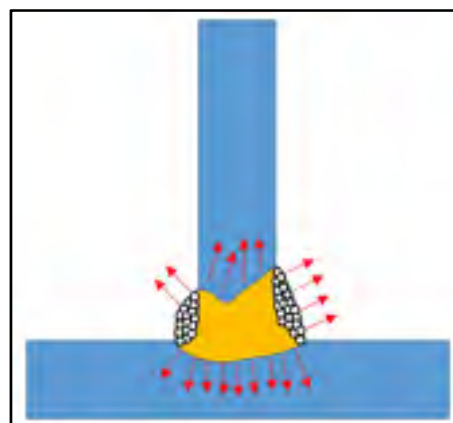


Figure 3.13 Relation between heat transfer and equiaxed grains.

3.3.2 Macroscopic studies on phase B welds

As already mentioned, a plan is employed to study the difference between the two base metals and also the effect of Ni content on prevention of hot cracking as one of the recommended actions in the literature. Figures 3.14 and 3.15 show the macroscopic metallography performed using low, medium and high Ni content filler metals for Gr.50 and Gr.80, respectively. Each workpiece has been investigated in three sections. The results indicate that all Gr.80 welds contain macrocracking while in Gr.50 welds no macrocracking was observed. On the other hand, no significant link is found in the present study between Ni content and hot cracking. This can be explained by the existence of more important root causes which probably overcome the positive effect of Ni and lead to the cracking of the Gr.80 welds.

As shown in Figures 3.14 and 3.15, weld penetration is not the same in different sections of the same workpiece. As described in Figure 3.11, the difference between penetration profiles in different sections of the same workpiece is the result of fluctuation in welding angle due to manual welding process. On the other hand, macrocracking does not occur through the entire weld. It can be assumed that there is a relationship between fluctuation in welding angle and susceptibility to hot cracking.

As shown in Figure 3.16, the weld face height (H2), excessive penetration height (H1) and penetration length (L) for Gr.80 welds are measured on macro images. The penetration length is approximately the same for all the specimens. It can be confirmed that arc fluctuation has no significant effect on the penetration length. Conversely, excessive penetration and penetration height change dramatically by altering the welding angle. Figure 3.17 indicates that the higher is the H2, the higher will be the susceptibility to hot cracking. This is in agreement with the literature which recommends to avoid deep welds to prevent hot cracking [24]. The minimum H2 among all Gr.80 specimens was observed on specimen 80-1-3 (H2=2.09 mm). As shown in Figure 3.15, although the centerline of the 80-1-3 specimen is free of hot cracking, a complete penetration has

been formed in the joint. An excessive penetration height of 1 mm can be recommended to prevent lack of penetration. On the other hand, the critical excessive penetration height above which the hot cracks might appear as a result of excessive penetration can be recommended as 2.5 mm. This is somehow conservative but keeps the penetration profile in a safe margin. This result is original and to the knowledge of the author it is the first time such processing map is proposed for these steels.

Karadeniz et al. have investigated the effect of welding parameters on automatic GMAW weld penetration [64]. They found an optimum combination of heat input and welding speed to have proper penetration. To maintain the penetration profile in optimum range (in this work: $H=1$ to 2.5 mm), it is recommended to use automatic welding with an optimized welding speed and heat input as well as a constant welding angle of 45° . According to the literature [24] the higher is the CO_2 content in shielding gas mixture the more will be the penetration of the weld. This is explained by the higher thermal conductivity of ionized CO_2 compared to Argon and therefore increase in heat input per unit length. Thus, decreasing the CO_2 content in the shielding gas mixture can reduce the weld penetration. This can be recommended as a remedy to reduce excessive penetration height and therefore mitigate susceptibility to hot cracking. Figure 3.18 schematically illustrates the effect of shielding gas mixture on weld penetration.

As indicated by arrows in Figure 3.19 the location where hot cracking appears is in the narrowed zone of weld metal below the V-shape profile. This V-shape profile also exists in lower side as illustrated. Hot cracking was observed under the conditions where the dendrites moving forward to the centerline are aligned together and perpendicular to the centerline of the weld. It should be mentioned that the velocities of the two solidification fronts are not necessarily similar. As a result of the formation of a hot spot in V-shape zone in the upper part of the T-joint base metal, solidification velocity from this surface decreases and therefore the centerline is moved upward. As illustrated in Figure 3.19, the distance from the centerline to the lower piece is higher than the upper piece. This is true for all the Gr.50 and Gr.80 specimens.

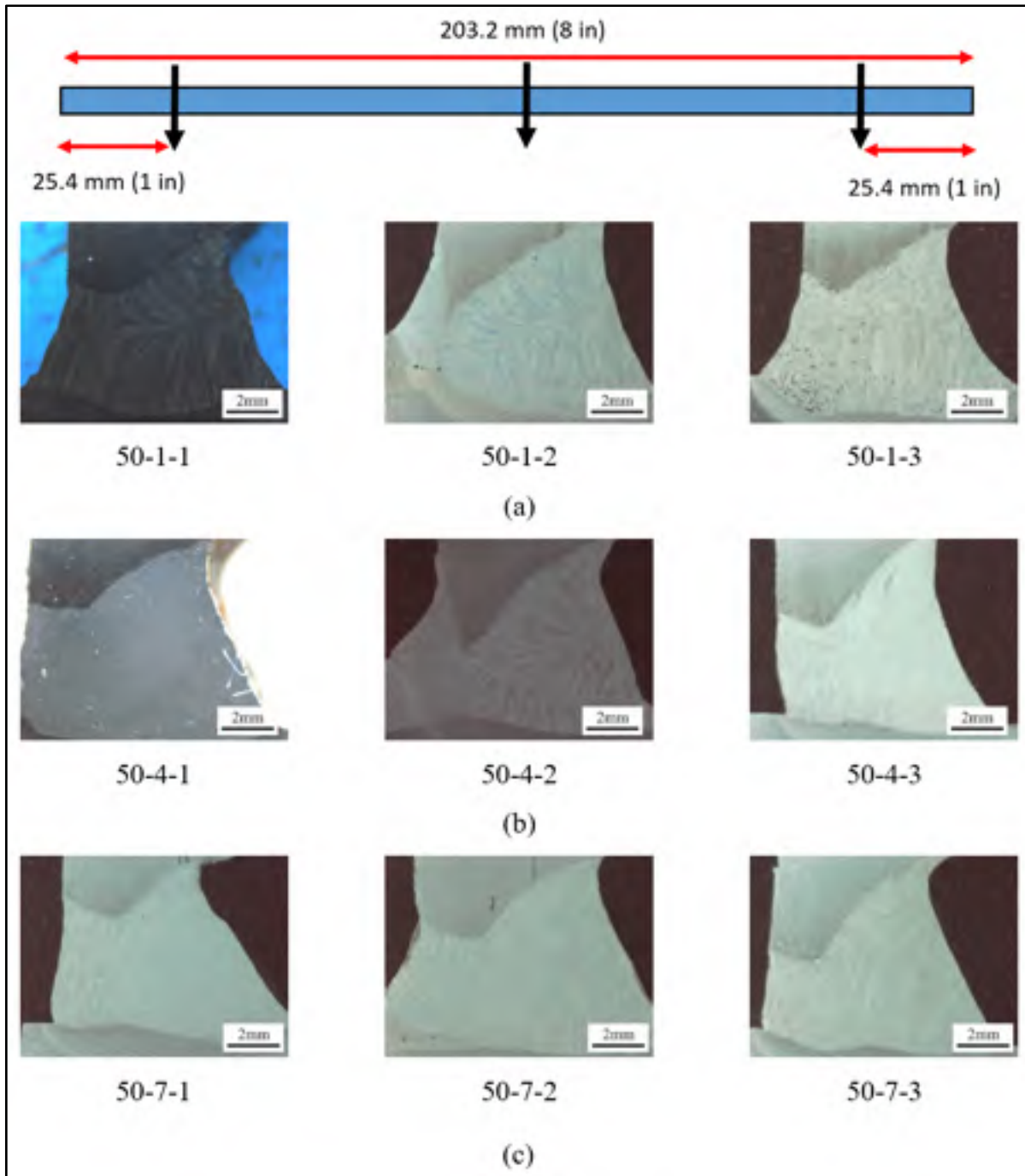


Figure 3.14 Macrograph of the Gr.50 workpieces in three sections using: a) low (0.02 wt%), b) medium (1.09 wt%) and c) high (2.15 wt%) Ni content filler metals. Etched by Nital 4%.

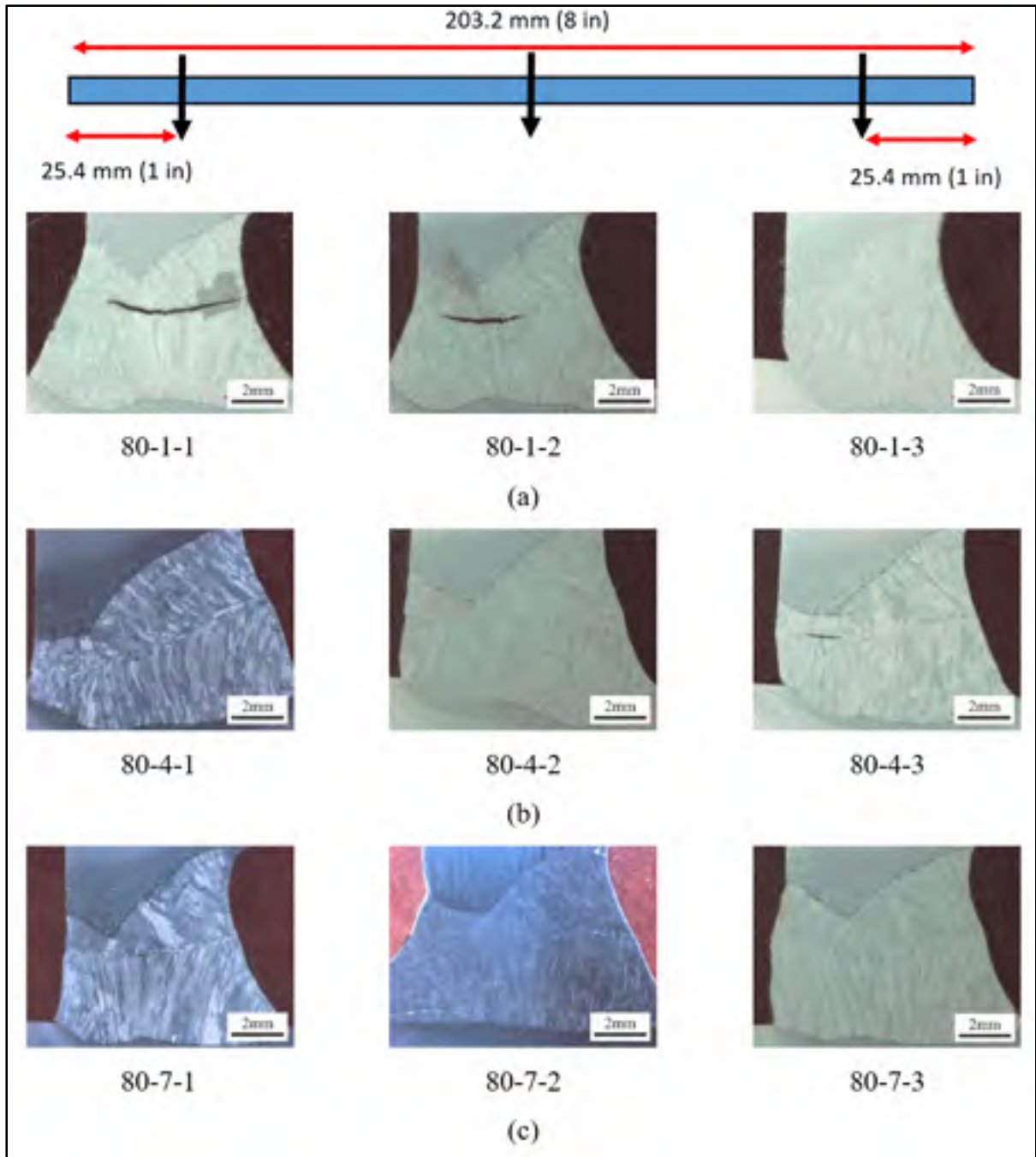


Figure 3.15 Macrograph of the Gr.80 workpieces in three sections using: a) low (0.02 wt%), b) medium (1.99 wt%) and c) high (2.39 wt%) Ni content filler metals. Etched by Nital 4%.

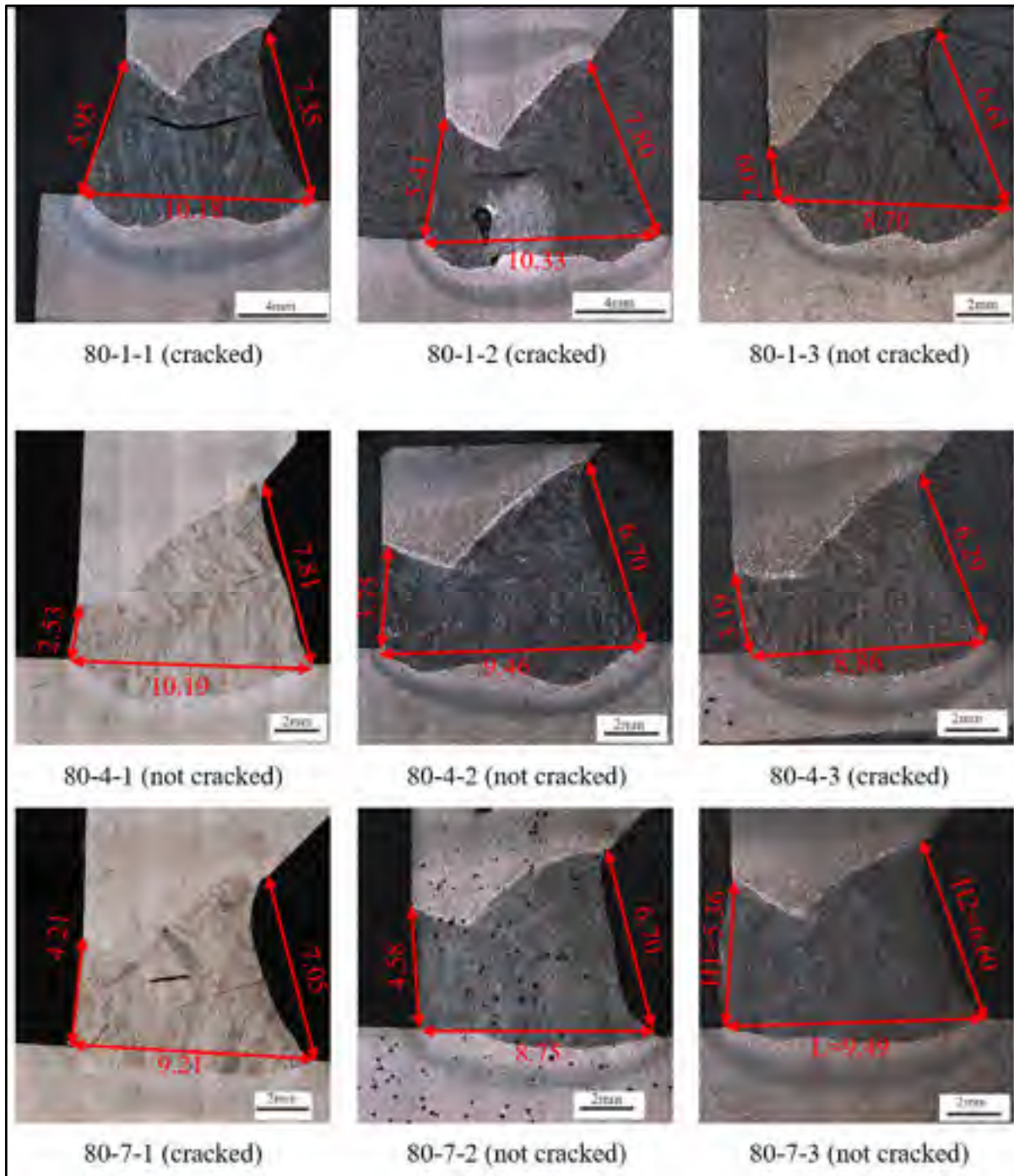


Figure 3.16 Measurement of weld face height (H2), excessive penetration height (H1) and penetration length (L) for Gr.80 welds. All specimens are etched by Nital 4%.

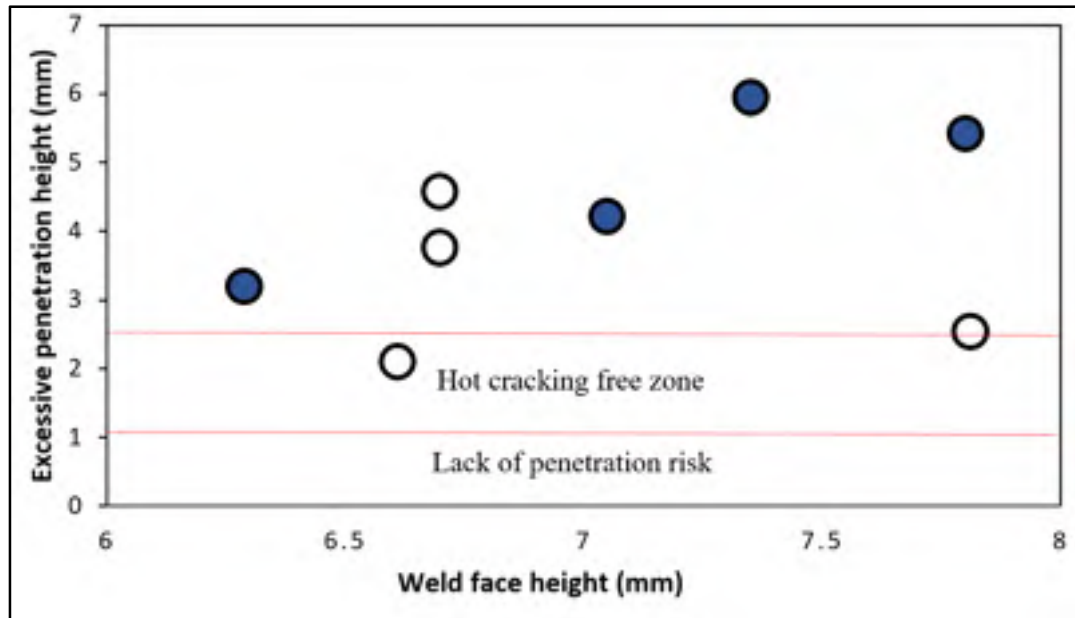


Figure 3.17 Relation between weld face height, excessive penetration height and susceptibility to hot cracking in Gr.80 weld metals.

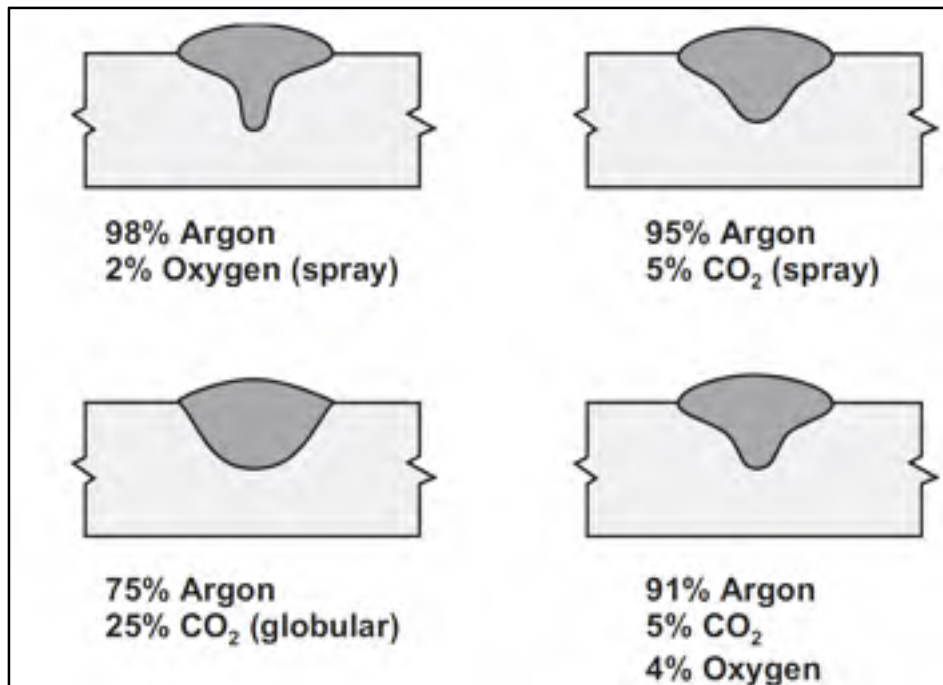


Figure 3.18 Effect of shielding gas mixture on weld penetration.
Taken from Welding for design engineers (2007, p.165)

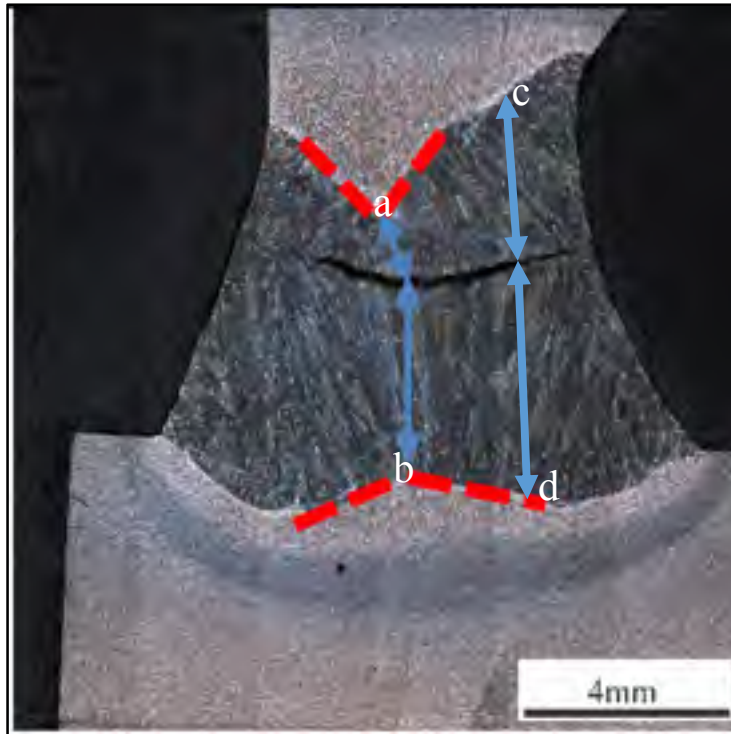


Figure 3.19 An example in specimen 80-1-1 illustrating the V-shape profile at both upper and lower sides in red dash lines. The distances between centerline and weld-base borders are illustrated by arrows.

Based on the observations in this work, hot cracking is probably related to the solidification patterns of the dendrites. The time elapsed between initiation and completion of solidification depends on the width of the fusion zone in a specific area. As shown schematically in Figure 3.20, the bigger is the width of the fusion zone, the longer will be the time needed for the dendrites to meet at the centerline. As illustrated in Figure 3.19 the time needed for dendrite growth completion from point (a) and (b) to the centerline is shorter than the time needed for growth completion from point (c) and (d) to the centerline.

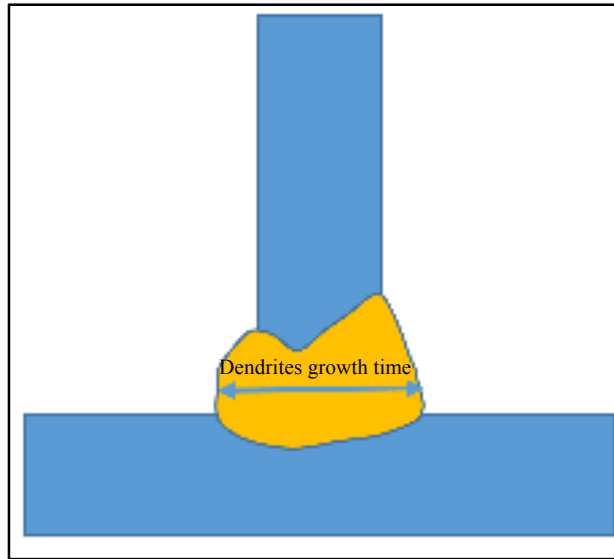


Figure 3.20 Schematic illustration of the time needed for completion of dendrite growth depending the width of the fusion zone.

Figure 3.21 shows the proposed stages of crack formation during solidification based on the results observed in this research. The penetration during the welding, causes an extra heat imposed to location 1 in Figure 3.21a and melts the base metal in this area. Therefore, a V-shape profile is formed in both sides before the start of solidification. As illustrated in Figure 3.21b solidification of all dendrites starts at the same time. The time elapsed for the dendrites in the narrow area to meet at the centerline is less than the time needed for the adjacent dendrites. As dendrite's growth is time dependent [9], the length of dendrites in the narrow area is less than the adjacent dendrites. Therefore, while the dendrites in the narrow area meet at the centerline (Figure 3.21c), the growth of adjacent dendrites is still ongoing. At the next stage, the dendrites in the narrow area start to contract while those in the adjacent zone are still growing and consequently meet at the centerline. In parallel dendrites in the V-shape area are losing their temperature and experiencing a contraction (Figure 3.21d). As the path for liquid penetration is blocked by the adjacent dendrites, the contraction in V-shape area cannot be compensated by liquid feeding. Therefore, the first failure appears in the narrowed V-shape zone in the form of very small voids. After formation of first void, the contraction of neighbor dendrites will continue and ease the crack propagation.

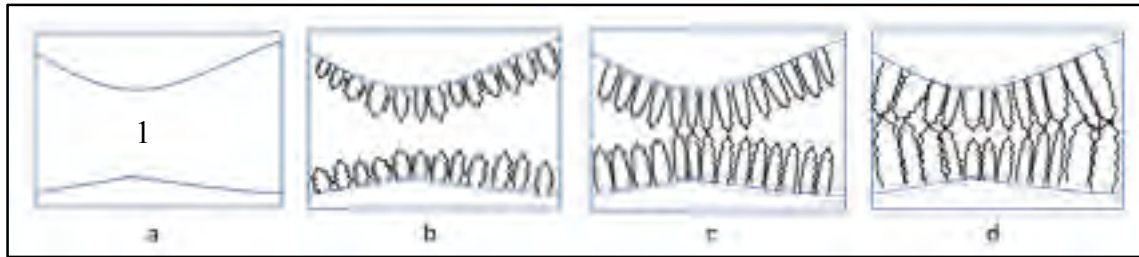


Figure 3.21 Schematic illustration of nucleation of a hot cracking at centerline; a) liquid before starting the solidification. b) nucleation and growth of dendrites, c) dendrites of V-shape area meet at centerline. d) dendrites which meet in stage c are being contracted and at the same time adjacent dendrites are developing and meeting each other blocking the liquid feeding path to narrow V-shape area which forms the first void.

As shown in Figure 3.22, equiaxed grains are also present at weld face as in phase A experiments. The formation of these equiaxed grains has been discussed in phase A and will not be repeated here. As shown in Figure 3.22a, the crack propagates at the meeting point of dendrites and stops at the equiaxed grains. It confirms that equiaxed grains block the crack propagation path. As shown in Figure 1.31 from the literature [55], the resistance of equiaxed grains against crack propagation is higher than dendritic microstructure. Equiaxed grains prevent the crack propagation. This leads the crack to stop before reaching the weld surface and not be visible during and after the welding. As the crack is located under the surface, it is not even detectable by fluorescent penetrant Inspection (FPI), and considering its small size it might not be detectable by ultrasonic techniques. Thus, it is recommended to have metallographic investigations before any industrial application.

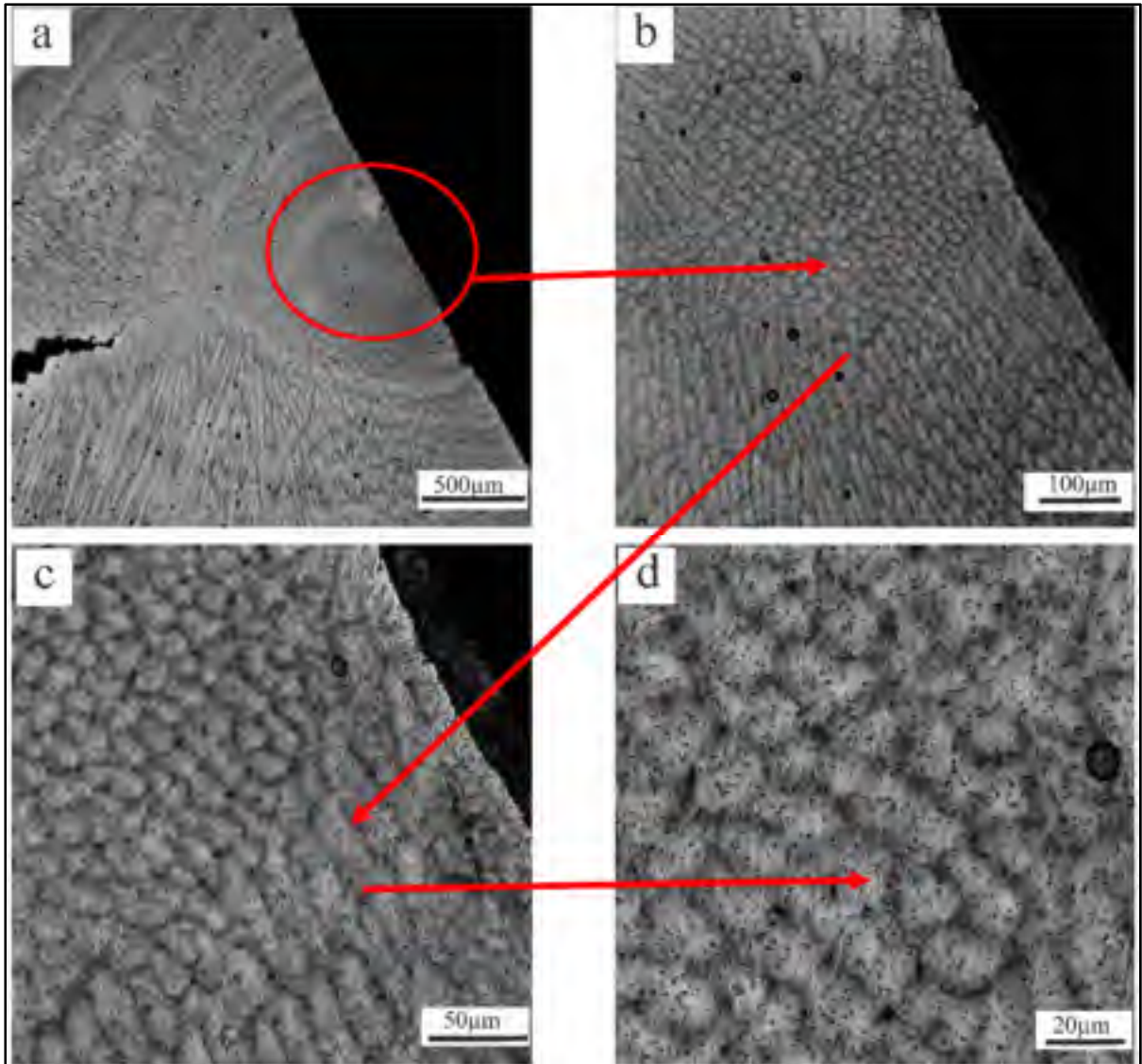


Figure 3.22 Consecutive images from equiaxed grains at weld face from a to d and their effect on crack stoppage (specimen: 80-1-1, hot etched).

The detailed investigation on weld penetration and solidification profile allowed to develop a more clear understanding of the hot cracking process observed at the macro scale and link them to the crack nucleation and propagation. In the next paragraphs, the effect of chemical composition and microstructure of the weld metal on hot cracking will be discussed.

3.3.3 Chemical composition

Using mass spectrometry, the chemical composition of the weld metal was obtained. A comparison between the chemical composition of base, filler and weld metal is shown in Table 3.3 and Table 3.4 for the phase B welds. The chemical compositions show that the carbon content of G.80 specimens is approximately the same (0.05-0.08 wt%) in base, filler and weld metal. In contrast, the carbon content of Gr.50 weld metal is higher than its base and filler metals. This can be attributed to the dissolution of pearlite bands shown in Figure 3.1 from the base metal to the weld. Dilution of carbon from the base metal can increase the weld tensile strength [65] and at the same time decrease the ductility and impact toughness. Higher carbon content can also increase the hardenability; however, austenite grain size and other alloying elements play also an important role in mechanical properties of steel [53]. Therefore, mechanical properties of the weld metal can not be substantiated only based on carbon content. Carbon equivalent (CE) for acicular ferrite microstructure in weld metal is proposed as: $C + (Mn/6) + (Si/24) + (Mo/29) + (V/14)$ [54]. Calculated CE showed in Table 3.5 indicates that CE varies in a small range (0.27-0.35 wt%) for all weld metals. Therefore, in spite of high carbon content in Gr.50 welds, the effect of alloying elements on mechanical properties is expected to be very close for both Gr.50 and Gr.80 welds.

Table 3.3 Comparison of chemical composition of base, filler metal and weld for Gr.50 welds phase B (wt%).

	C	Mn	P	S	Si	Ni	Cr	Mo	V	Cu	Al	Nb	Ti	Sn	N
base	0.06	1.4	0.015	0.003	0.14	0.16	0.16	0.05	0.008	0.29	0.03	0.045	0.013		
50-1 wire	0.07	1.53	0.017	0.012	0.90	0.02	0.01	0.02	<0.01	0.02	<0.001				
50-1 weld	0.154	1.076	0.0066	0.0033	0.427	0.09	0.06	0.022	0.015	0.16	0.0157	0.0016	36.3 ppm	0.0054	163.6 ppm
50-4 wire	0.06	1.15	0.009	0.011	0.38	1.09	0.09	0.11	<0.01						
50-4 weld	0.132	1.02	0.012	0.009	0.33	0.55	0.07	0.088	0.015	0.15	0.024	0.0026	0.0005	0.0071	0.0003
50-7 wire	0.04	1.06	0.009	0.007	0.30	2.15	0.04	<0.04	<0.01	0.03					
50-7 weld	0.097	1.01	.0013	0.0001	0.236	1.28	0.06	0.024	0.0257	0.14	0.0236	0.0020	171.5 ppm	0.0058	134.2 ppm

Table 3.4 Comparison of chemical composition of base, filler metal and weld for Gr.80 welds phase B (wt%).

	C	Mn	P	S	Si	Ni	Cr	Mo	V	Cu	Al	Nb	Ti	Sn	N
base	0.05	1.59	0.015	0.003	0.25	0.26	0.19	0.21	0.010	0.41	0.04	0.088	0.031	0.012	0.114
80-1 wire	0.07	1.53	0.017	0.012	0.90	0.02	0.01	0.02	<0.01	0.02	<0.001				
80-1 weld	0.079	1.492	0.0043	0.0012	0.438	0.192	0.12	0.121	0.0077	0.262	<0.001				
80-4 wire	0.05	1.48	0.01	0.007	0.30	1.99	0.22	0.52							
80-4 weld	0.056	1.66	0.011	0.003	0.31	0.34	0.18	0.201	0.011	0.39	0.040	0.1054	0.0002	0.0128	0.0002
80-7 wire	0.063	0.91	0.008	0.010	0.37	2.39	0.06	0.007	0.003	0.03					
80-7 weld	0.052	1.577	0.0101	0.0043	0.326	1.03	0.13	0.24	0.0094	0.277	0.0336	0.0662	369.4p pm	0.0087	130.4p pm

Table 3.5 Carbon equivalent calculations based on weld metals chemical compositions.

50-1	$0.154 + (1.076/6) + (0.427/24) + (0.022/29) + (0.015/14) = 0.3527$
50-4	$0.132 + (1.02/6) + (0.33/24) + (0.088/29) + (0.015/14) = 0.3198$
50-7	$0.097 + (1.01/6) + (0.236/24) + (0.024/29) + (0.0257/14) = 0.2788$
80-1	$0.079 + (1.492/6) + (0.438/24) + (0.121/29) + (0.0077/14) = 0.3485$
80-4	$0.056 + (1.66/6) + (0.31/24) + (0.201/29) + (0.011/14) = 0.3502$
80-7	$0.052 + (1.577/6) + (0.326/24) + (0.24/29) + (0.0094/14) = 0.3403$

3.3.4 Microstructural studies on weld metal

The results of macrography do not show any macrocracking in Gr.50 specimens; however, the centerline of Gr.50 specimens have been subjected to micrographic investigation to ensure the integrity of the centerline. Although, as shown in Figure 3.23 after hot etching of Gr.50 specimens a crack like boundary was revealed, but the images taken after etching with Nital 4% for microscopic examinations as shown in Figure 3.24, did not reveal any cracking at the centerline of Gr.50 specimens.

Comparison of Figures 3.23 and 3.25 shows that the mode of solidification for Gr.50 weld is more dendritic with well-developed secondary arms compared to Gr.80 where the weld zone consists of cellular grains. As shown in Figures 3.26 and 3.27, the secondary dendrite arms (SDA) are more developed in Gr.50 weld metals compared to Gr.80. However, Gr.80 has more alloying elements and based on general assumption for solidification pattern, illustrated in Figure 3.28, more dendritic microstructure is expected for a melt containing higher alloying elements and therefore higher constitutional supercooling [9]. This apparent discrepancy can be explained by the difference between initiation of solidification in Gr.50 and Gr.80 melts. In contrast to casting, where solidification initiates by nucleation, in welding there is no nucleation stage due to the existence of unmelted grains which act as preferred nucleation site for new grains to grow with the same crystallographic orientations. The growth of weld metal dendrites from previously existing unmelted gains is called

epitaxial growth [66]. Figure 3.30 shows a schematic of expitaxial growth on previously existed grains.

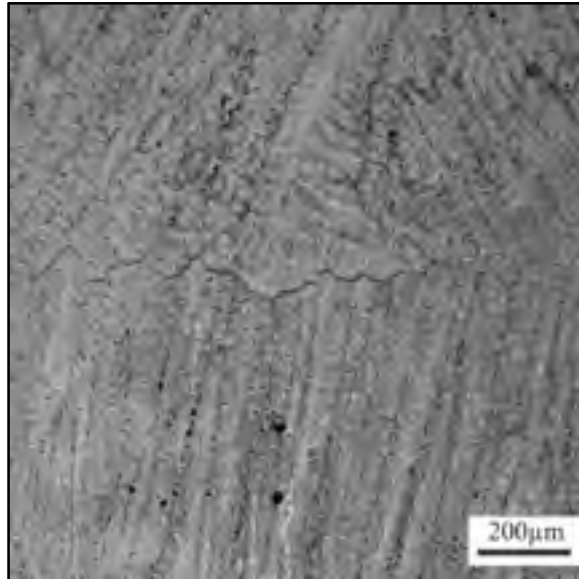


Figure 3.23 Dendrites with well developed secondary arms in Gr.50 (specimen: 50-1-3, hot etched).

Comparing the initial grain size in Figure 3.29a and b at the interface of the weld and HAZ, the primary austenite grain size of Gr.50 is around 60 μm while it is around 45 μm for Gr.80. Primary dendrite arm spacing (PDAS) measurements for both welds (around 75 μm for Gr.50 and 40 μm for Gr.80) confirm a good compliance between PDAS in weld metal with primary austenite grain size for HAZ in both materials. This is in agreement with observations regarding the epitaxial growth of the dendrites on previously existing grains in the partially melted zone proposed by [66], as shown in Figure 3.30.

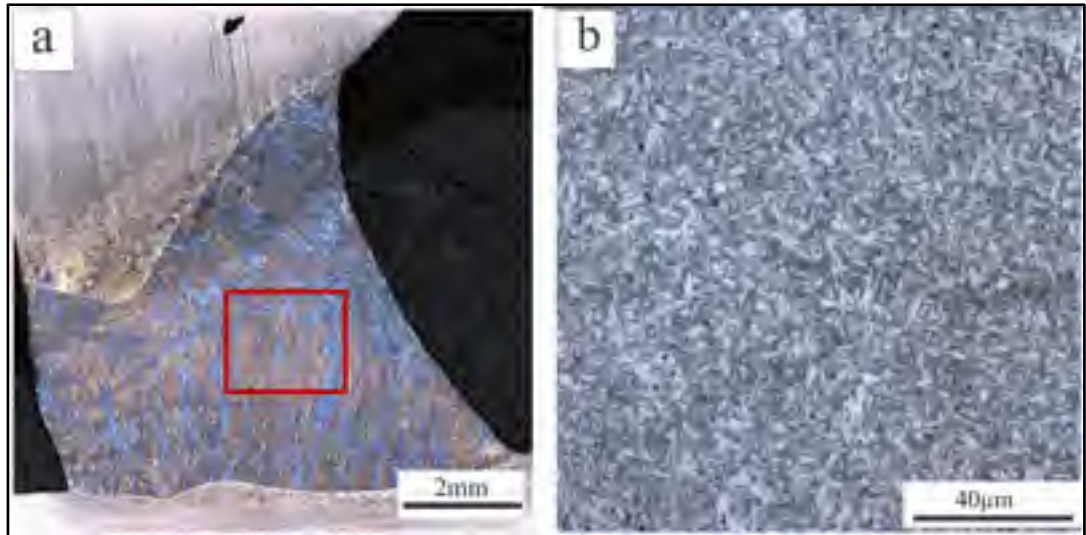


Figure 3.24 Centerline of the weld metal; a) sound centerline in Gr.50 specimen. b) the same zone in higher magnification (specimen:50-4-3, etched by Nital 4%).

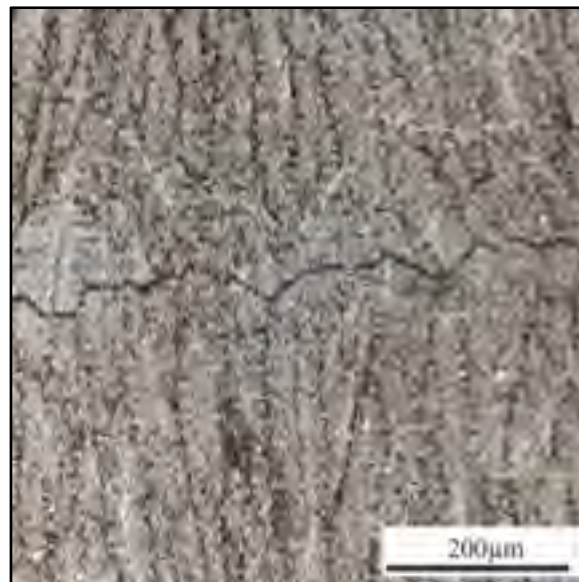


Figure 3.25 Dendrites with short secondary arms in Gr.80 (specimen: 80-4-3, hot etched).

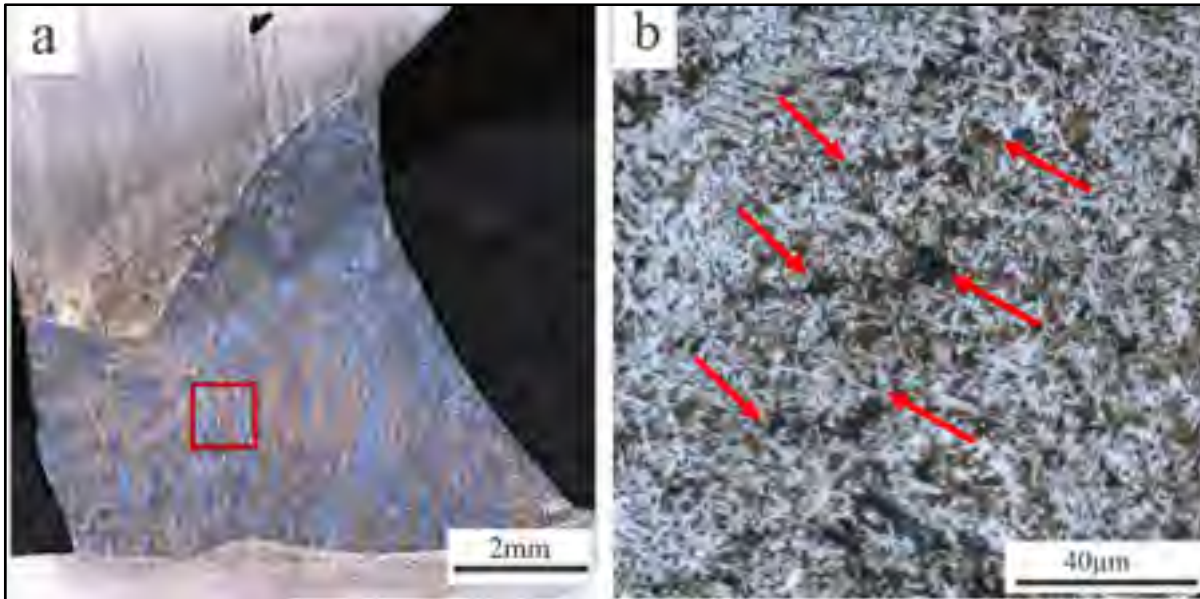


Figure 3.26 Long secondary dendrite arms in Gr.50 in a) low and b) high magnification. SDA tips are shown by arrows (specimen: 50-4-3, hot etched).

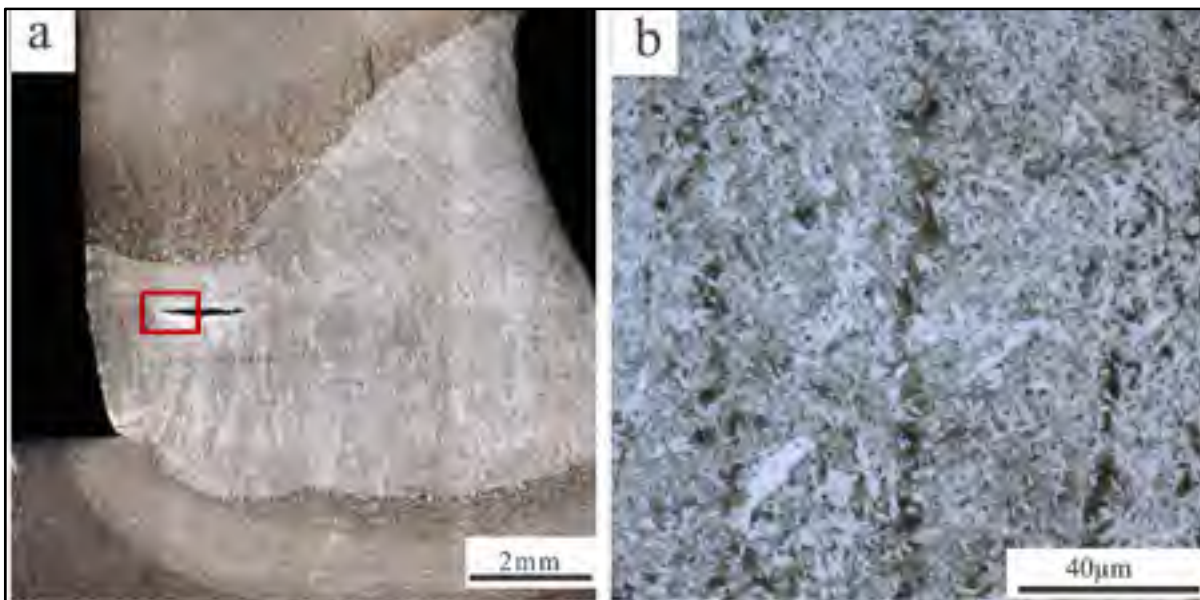


Figure 3.27 Short secondary dendrite arms in Gr.80 in a) lower and b) higher magnification (specimen: 80-4-3, hot etched).

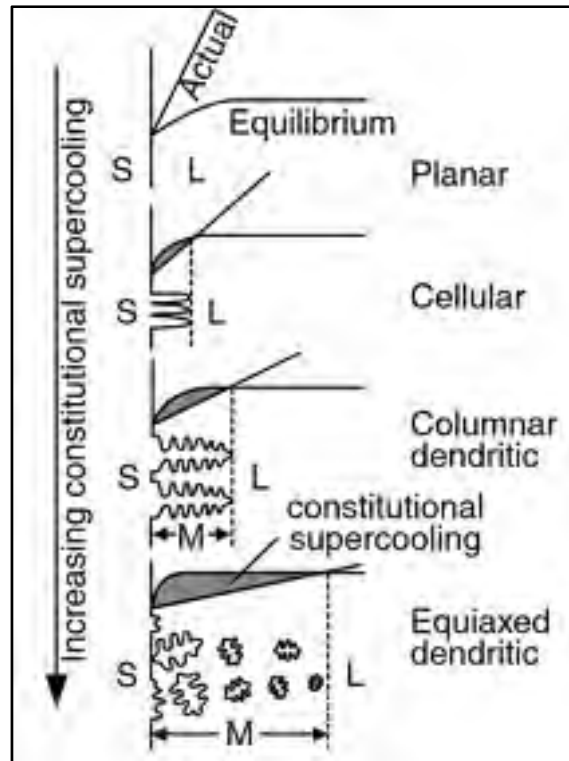


Figure 3.28 Evolution of solidification mode by increase in constitutional supercooling.
Taken from Kou (2003, p.159).

Bigger PDAS for Gr.50 provides the condition for the development of more secondary dendrite arms (SDA). As shown in Figure 3.26, SDA in Gr.50 welds are locked together around the centerline of the weld and therefore increase the resistance of centerline against the mechanical stresses, while the SDA in Gr.80 are not long enough to lock each other.

In contrast to SDA, PDA cannot be easily locked in V-shaped zone due to perpendicularity to the centerline. However, as the distance from the narrow V-shaped zone is increased, the perpendicularity is reducing and therefore, PDA become also locked and no cracking is observed.

Microscopic examinations also revealed that hot cracks are most of the time adjacent to the inclusions (Figure 3.31). The possible contribution of nonmetallic inclusions to ease hot cracking propagation will be discussed in the following paragraphs.

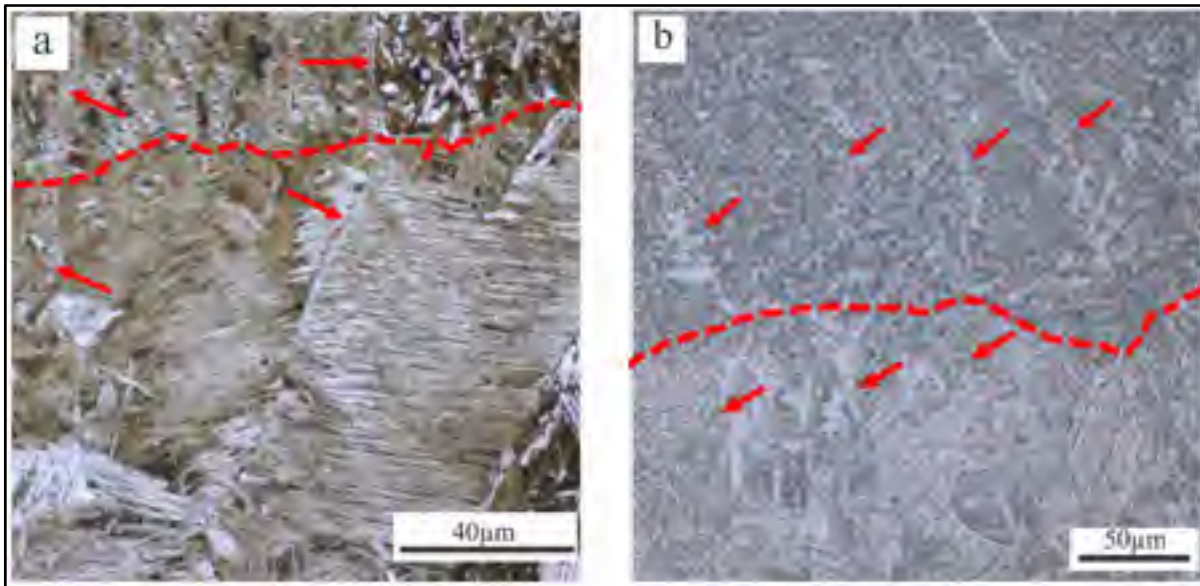


Figure 3.29 Comparison of grain size in HAZ of a) Gr.50 and b) Gr. 80 adjacent to the weld.

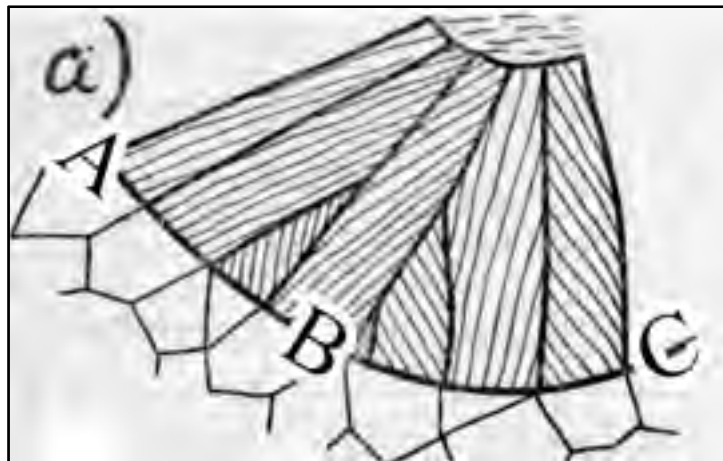


Figure 3.30 Schematic representation of epitaxial fusion line ABC proposed by Rajamäki(2008, p.18)

Figure 3.32 shows the blades nucleated from nonmetallic inclusions in both Gr.50 and Gr.80 welds. As discussed in literature review, acicular ferrite can be differentiated from Widmanstätten and idiomorphic ferrites by width of blades, blades' length to width ratio and also high angle boundaries [11]. The blades' width in Figure 3.32 is less than 5 μm and the ratio of length to width in most of the blades is less than 4. These two characteristics are related to acicular ferrite microstructure. Moreover, the presence of high angle boundaries in all blades confirms that the predominant component of the weld metal microstructure is acicular ferrite which has nucleated heterogeneously from nonmetallic inclusions. This finding is in agreement with those reported by other authors [11, 12, 15, 16].

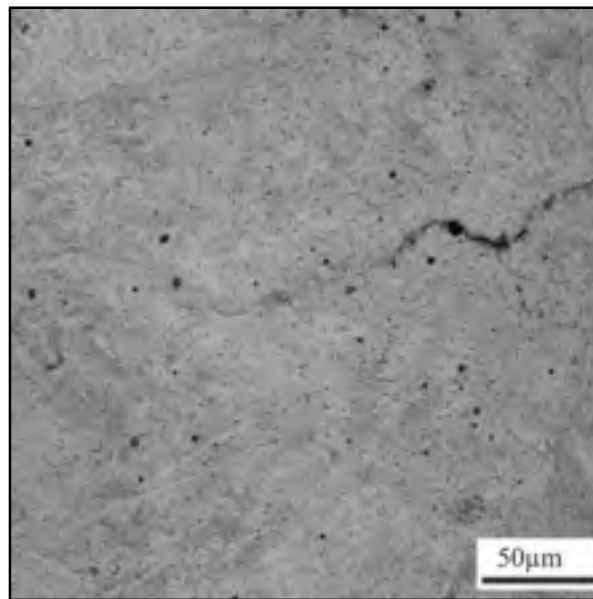


Figure 3.31 Centerline of the weld where hot cracking follows the inclusions engulfed with gas porosities (specimen BK2-1, hot etched).

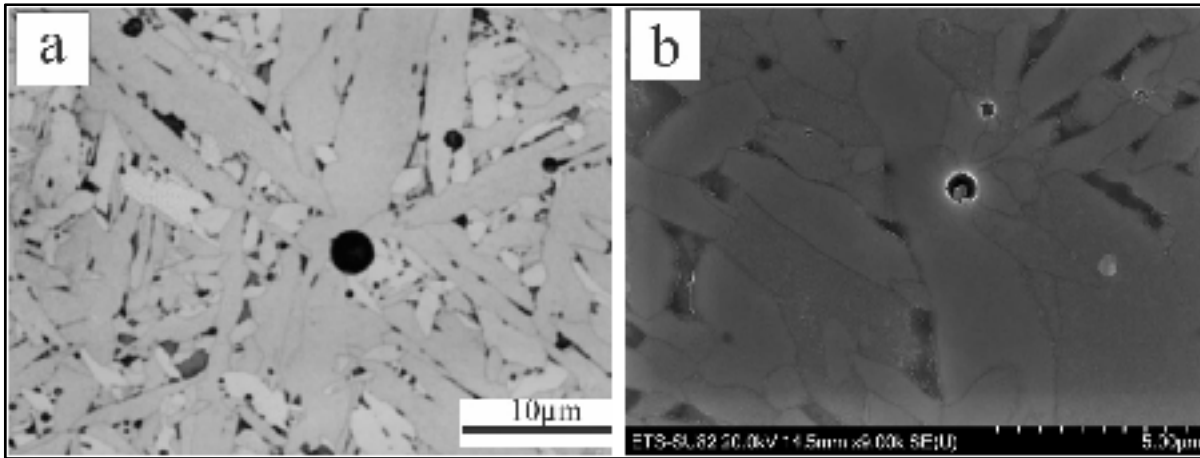


Figure 3.32 Acicular ferrite nucleated from inclusions; a) Gr.80 (specimen: K03-1, hot etched) b) Gr.50 (specimen: 50-1-1, hot etched).

As shown in high magnification FEG-SEM images in Figure 3.33, different morphologies of inclusions are observed in the weld metal. EDS results in Figure 3.34 confirm the existence of a variety of inclusions containing V, Ti and Al. Investigating on morphology of inclusions as shown in Figure 3.33 confirms that a round shaped void engulfs every single inclusion which seems to be gas porosity. To ensure that these voids are not the result of etching, as polished specimen was also studied under SEM and the existence of gas porosity in weld metal was confirmed (Figure 3.35).

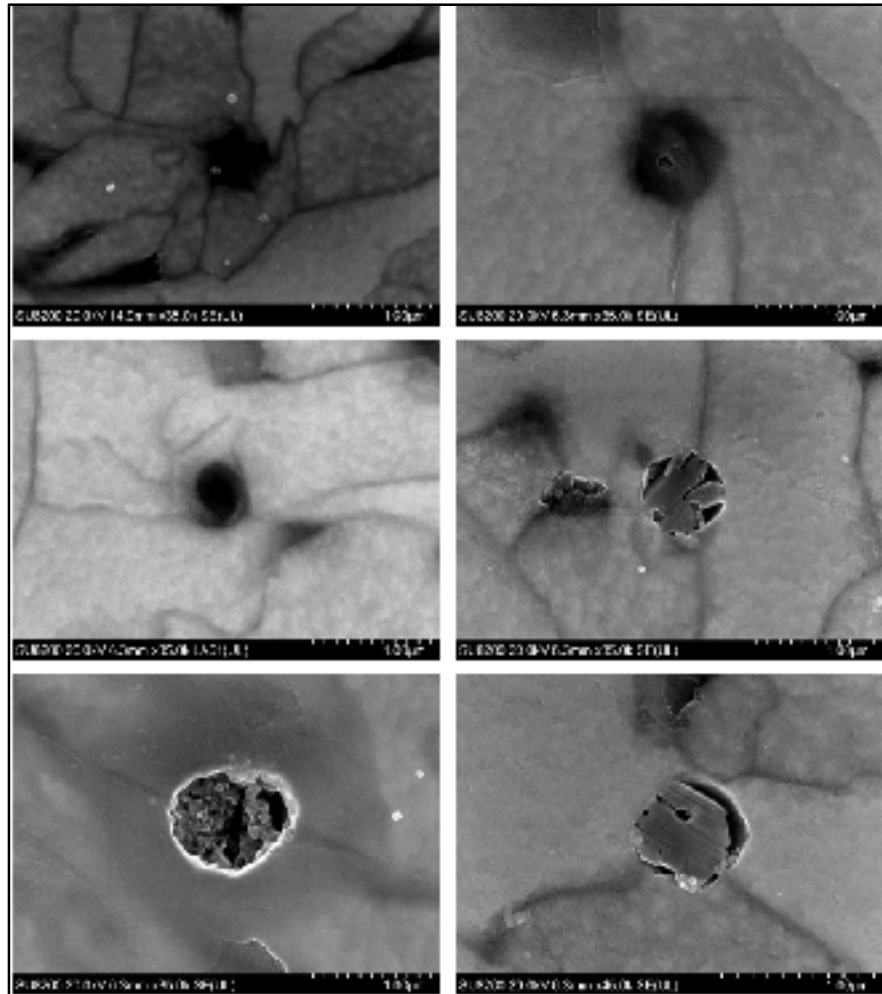


Figure 3.33 Morphologies of different types of inclusions in weld metal observed by FEG-SEM (specimen:80-4-3, hot etched).

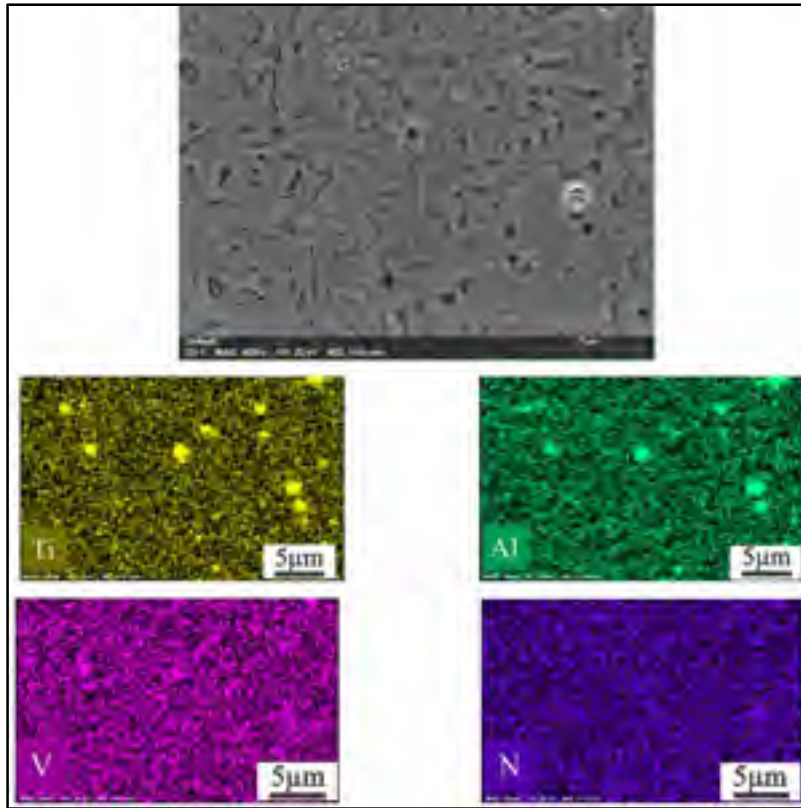


Figure 3.34 EDS mapping on weld metal showing the existence of Al, V and Ti in inclusions (specimen: 80-4-3, hot etched).

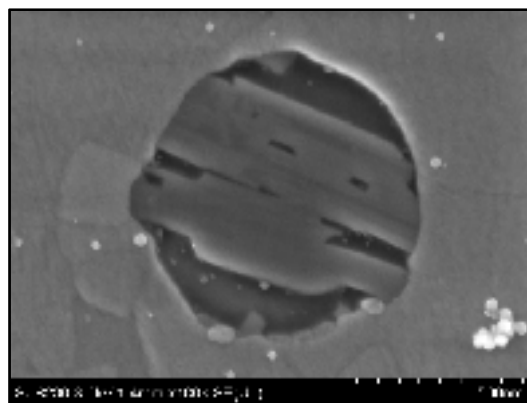


Figure 3.35 Inclusions in as polished weld metal (specimen: 80-4-3).

Figures 3.36 and 3.37 show the microstructure of weld metal for Gr.50 and Gr.80 welds using low, medium, and high Ni content filler metals, respectively. High angle acicular ferrite blades nucleated from nonmetallic inclusions, Widmanstätten ferrite which are nucleated from dendrites' boundaries and allotriomorphic ferrite all present in weld metal of both Gr.50 and Gr.80 which is also in agreement with those reported by other researchers [11, 12]. Differentiating between continuous and allotriomorphic ferrite is not easy by optical microscopy. SEM images shown in Figure 3.38 confirms that the grain boundary ferrites are not continuous. As described in chapter 1, allotriomorphic ferrites are formed discontinuously on grain boundaries. Therefore, it can be confirmed that the ferrites formed on dendrite boundaries are allotriomorphic. As shown in Figure 3.39, primary allotriomorphic ferrite is also observed in boundaries of the equiaxed grains in weld face and Widmanstätten ferrite nucleates on them into the grains. The distribution of acicular, Widmanstätten and primary allotriomorphic ferrite, shape and length of acicular ferrites and width of allotriomorphic ferrites bands are similar in both Gr.50 and Gr.80 welds. However, comparing the specimens with different Ni content, it can be concluded that the lower is the Ni content in the weld metal, the higher will be the probability of formation of Widmanstätten ferrite. According to the literature, adding Ni (2.03-2.91 wt%) and Mo (0.7-0.995 wt%) both together enhances the volume fraction of acicular ferrite [17]. As mentioned in Table 1.3, Mo increases significantly the acicular ferrite portion. Ni also has a moderate increasing effect on acicular ferrite portion [15]. As shown in Table 3.6, the increase in Ni content of the welds except for the specimen 50-7 is accompanied by increase in Mo content. Thus it can be concluded that increase in Ni and Mo content leads to higher volume fraction of acicular ferrite which in turn delays the propagation of Widmanstätten ferrite into the dendrites.

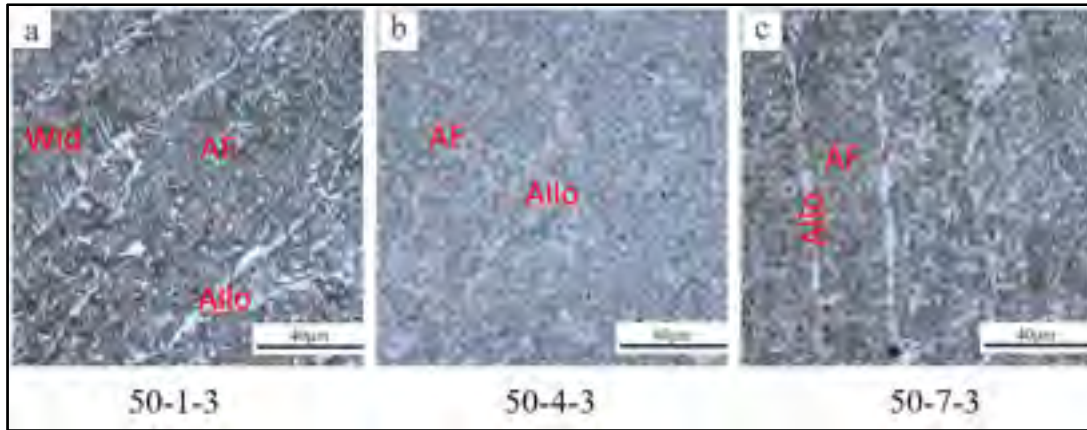


Figure 3.36 Microstructure of Gr.50 welds containing acicular ferrite (AF), Widmanstätten (WF) and allotriomorphic ferrite (Allot) welded by filler containing a) low Ni, b) medium Ni, c) high Ni (all specimens are etched by Nital 4%).

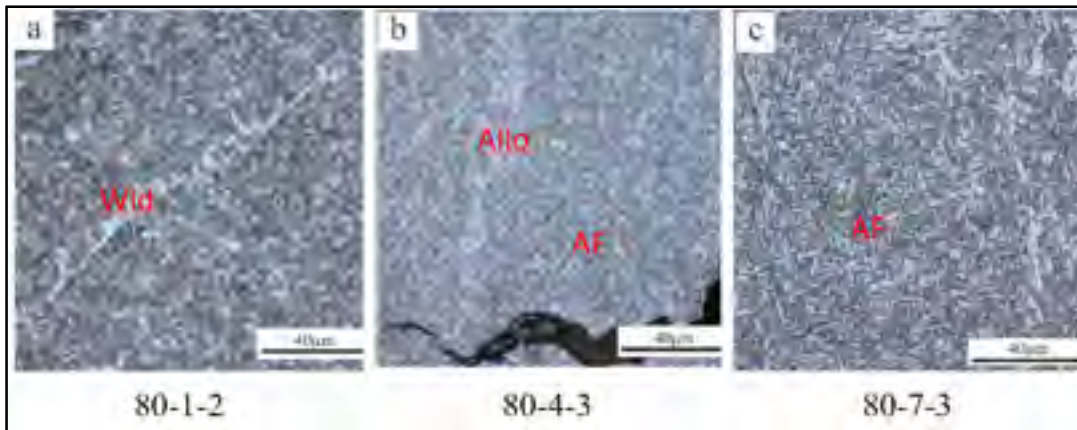


Figure 3.37 Microstructure of Gr.80 welds containing acicular ferrite (AF), Widmanstätten (WF), allotriomorphic (Allot) welded by filler containing a) low Ni, b) medium Ni, and c) high Ni (all specimens are etched by Nital 4%).

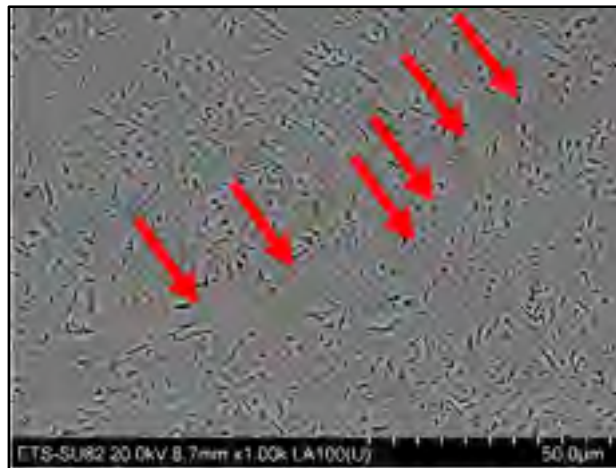


Figure 3.38 Illustration of allotropic ferrite in dendrite boundary. Arrows illustrate the boundaries between ferrites (specimen: 50-1-1, hot etched).

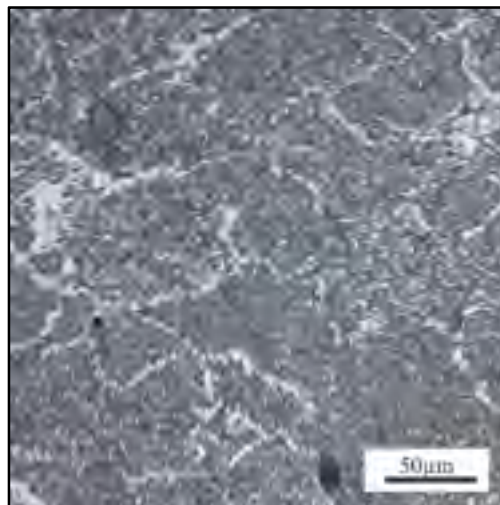


Figure 3.39 Allotropic ferrites in equiaxed grain boundaries with Widmanstätten ferrite nucleated from the allotropic ferrites (specimen 50-1-3 etched by Nital 4%).

Table 3.6 Ni and Mo content in weld metals.

Specimen	Ni (Wt%)	Mo (Wt%)
50-1	0.09	0.022
50-4	0.58	0.088
50-7	1.28	0.024
80-1	0.19	0.12
80-4	0.34	0.20
80-7	1.03	0.24

3.3.5 Local chemical changes at centerline of the weld

In order to study the type and distribution of local solute elements at the centreline of the weld, EDS mapping was employed. The etched centreline is clearly observable by optical microscope and even appear as a crack which could be misleading about hot cracking of Gr.50 weld metal. However, detection of centreline during SEM observations was challenging as no apparent crack was present and the determination of the location of the weld centreline was not straightforward. As shown in Figure 3.40a, in order to accurately determine the position of the weld centreline, indentations were made using Vickers microhardness machine on the centreline path. Then the specimen was brought under SEM and the line was identified. It became clear that what was looking as crack under optical microscope is actually the meeting points of solidification fronts from the two sides of the weld. Therefore, other possibilities such as segregation of alloying elements were examined. Figures 3.40 and 3.41 show the EDS maps of the alloying elements at the centerline of the Gr.80 and Gr.50 welded with medium Ni filler for Gr.80 and Gr.50, respectively. The results reveal enrichment of Mo, Cu, S, Ni, Nb at the centerline of the Gr.80 welds. While in Gr.50, in addition to those elements, Si and Mn enriched at the centerline. Microsegregation of Si and Mn between dendrites have been detected by Xinjie Di et al. as detrimental elements for mechanical properties of the medium manganese steel GMAW weld [67]. Tavares et al. have reported on the influence of enrichment in Si, S and Mn on fracture surface of the ASTM

A335 welded by GMAW. Analyzing a section of filler metal, they also showed that some of the tramp elements like Si and Mn can be diluted from filler metal as well as the base metal [68].

In order to have an estimation about the solidification range of welds, liquidus and solidus temperatures were calculated for all weld metals in both equilibrium and 100°C/s cooling rates. The results are reported in Figures 3.42 and 3.43 where the solidification range of Gr.50 low Ni weld is very close to that of Gr. 80 low Ni weld. This is also true for medium and high Ni specimens. Similar solidification ranges are in agreement with the EDS map results showing that microsegregation of tramp elements occurs on both Gr.50 and Gr.80 welds. As none of the Gr.50 welds were cracked, it can be concluded that although microsegregation of tramp elements reduce the resistance of the centerline to hot cracking but in the case of the current work, it has a minor influence.

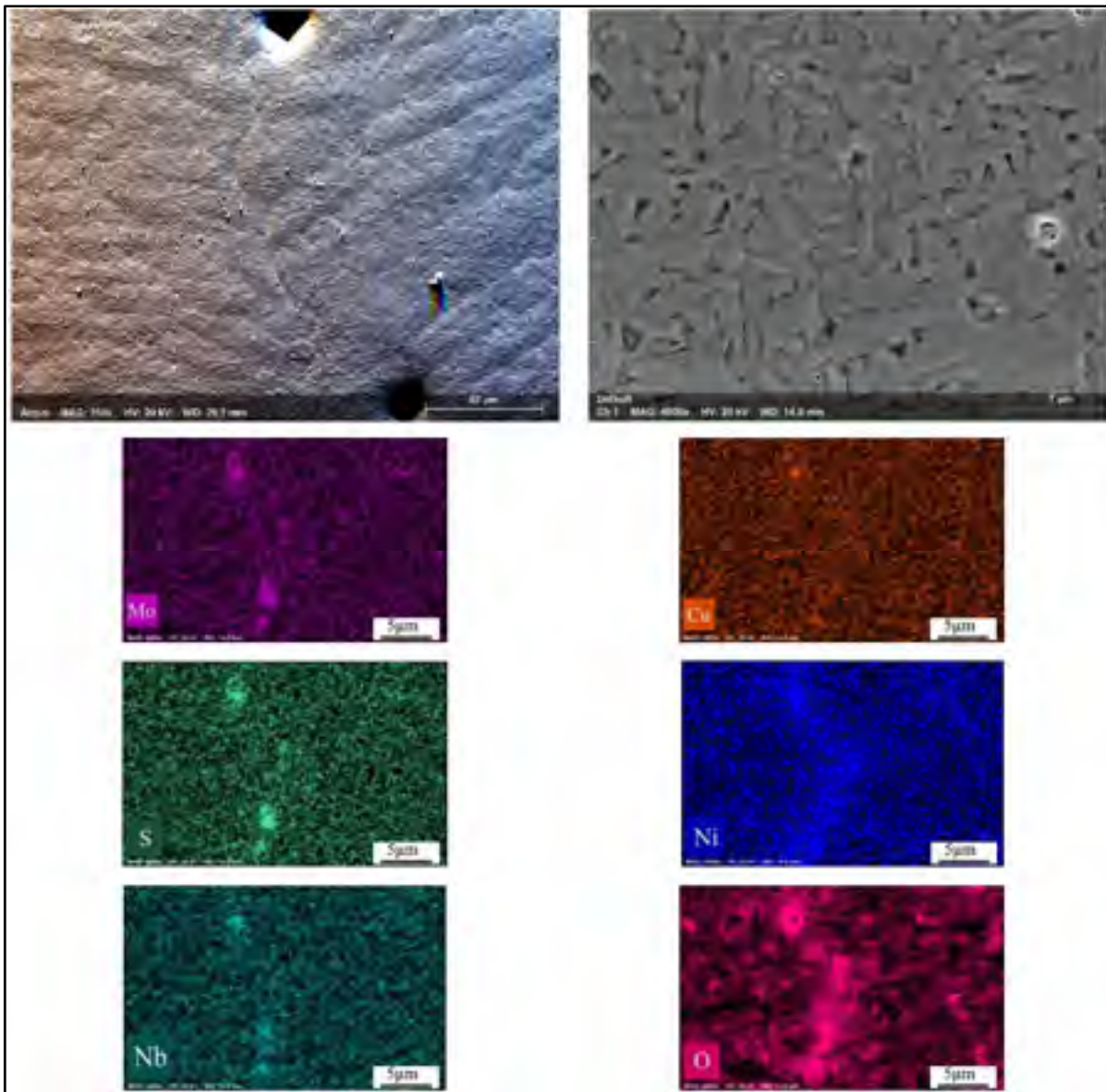


Figure 3.40 EDS mapping showing microsegregation of components at centerline of Gr.80 weld (specimen: 80-4-3, hot etched).

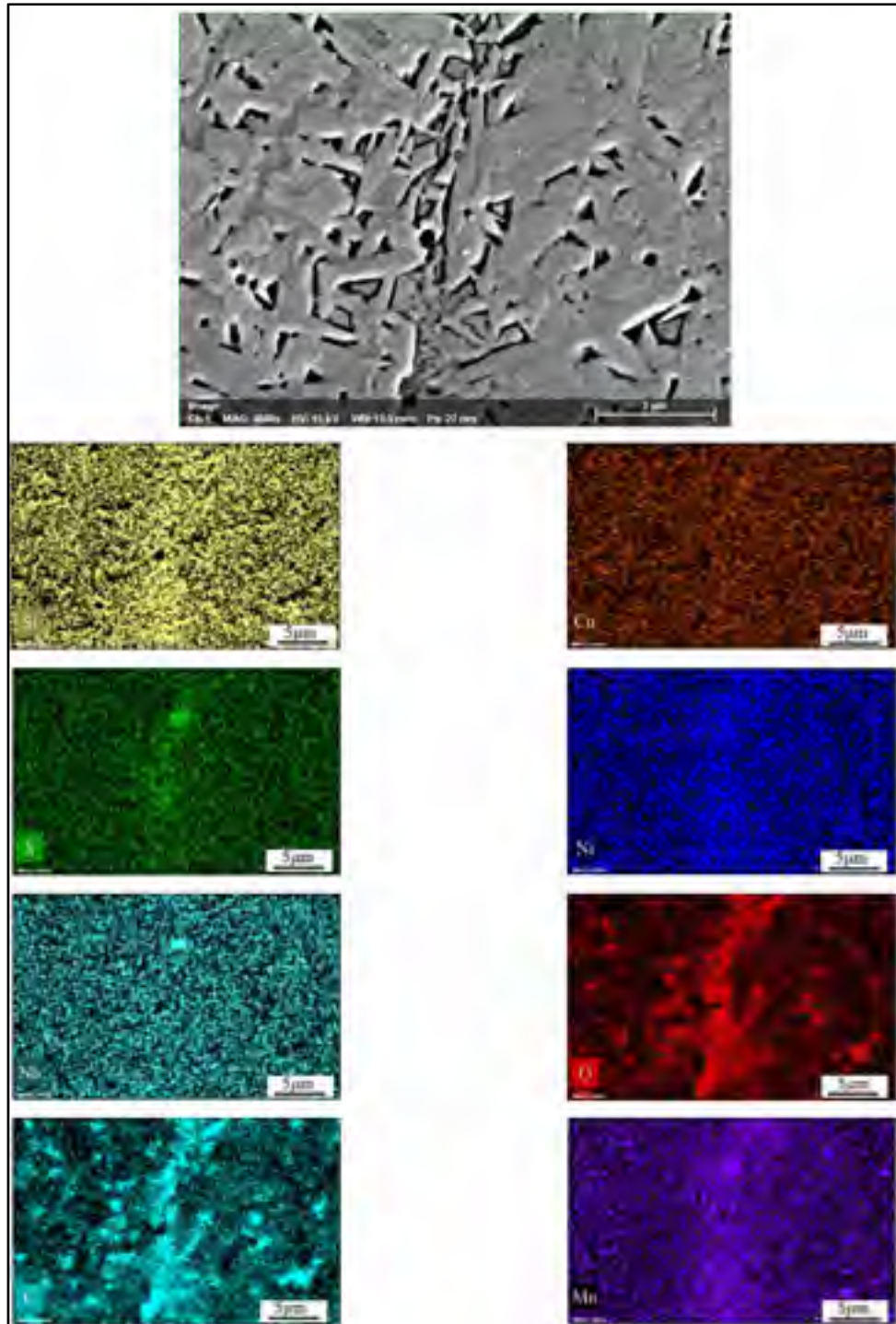


Figure 3.41 EDS mapping showing microsegregation of components at centerline of Gr.50 weld (specimens:50-4-3, hot etched).

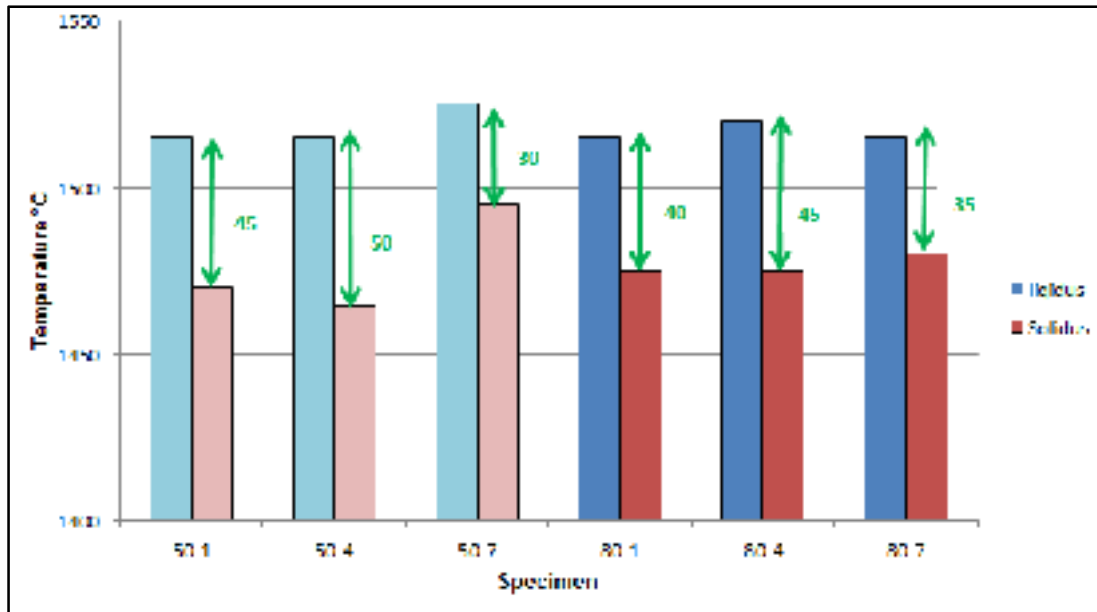


Figure 3.42 Comparison of solidification range calculated for weld specimens at cooling rate of 100°C/s.

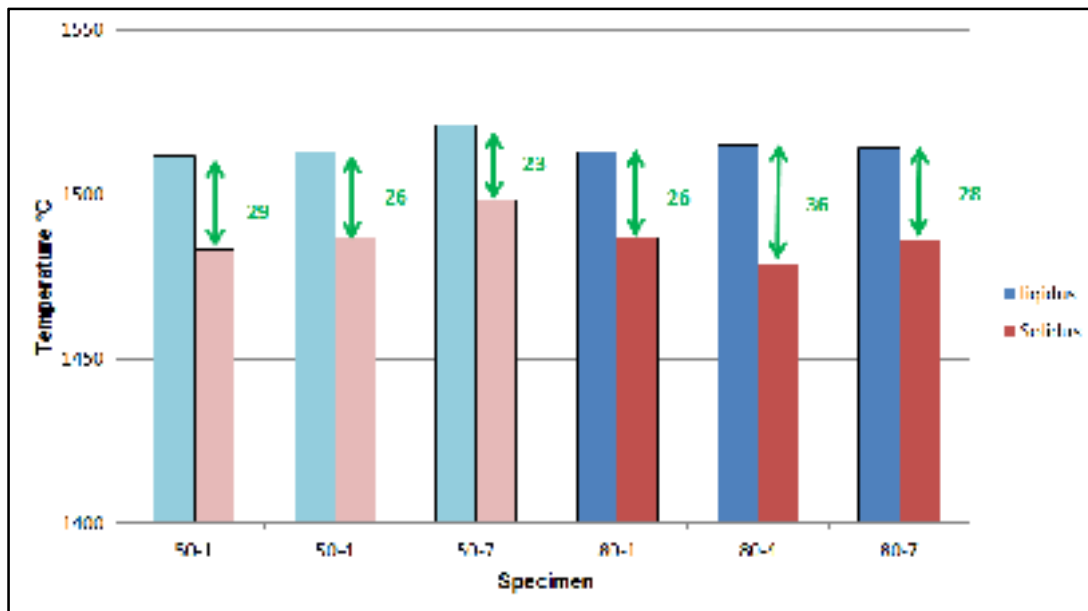


Figure 3.43 Comparison of solidification range calculated for weld specimens at Equilibrium cooling rate.

3.4 Effect of heat affected zone on hot cracking

CCT diagrams for Gr.50 base metal showed in Figure 3.44 confirm the formation of ferrite and bainite in high cooling rates (100°C/s and 10°C/s), while in lower cooling rates formation of pearlite is also probable. Therefore, observation of different morphologies of bainite and ferrite can be expected in Gr.50 HAZ close to the weld-HAZ boundary and pearlite in further distances.

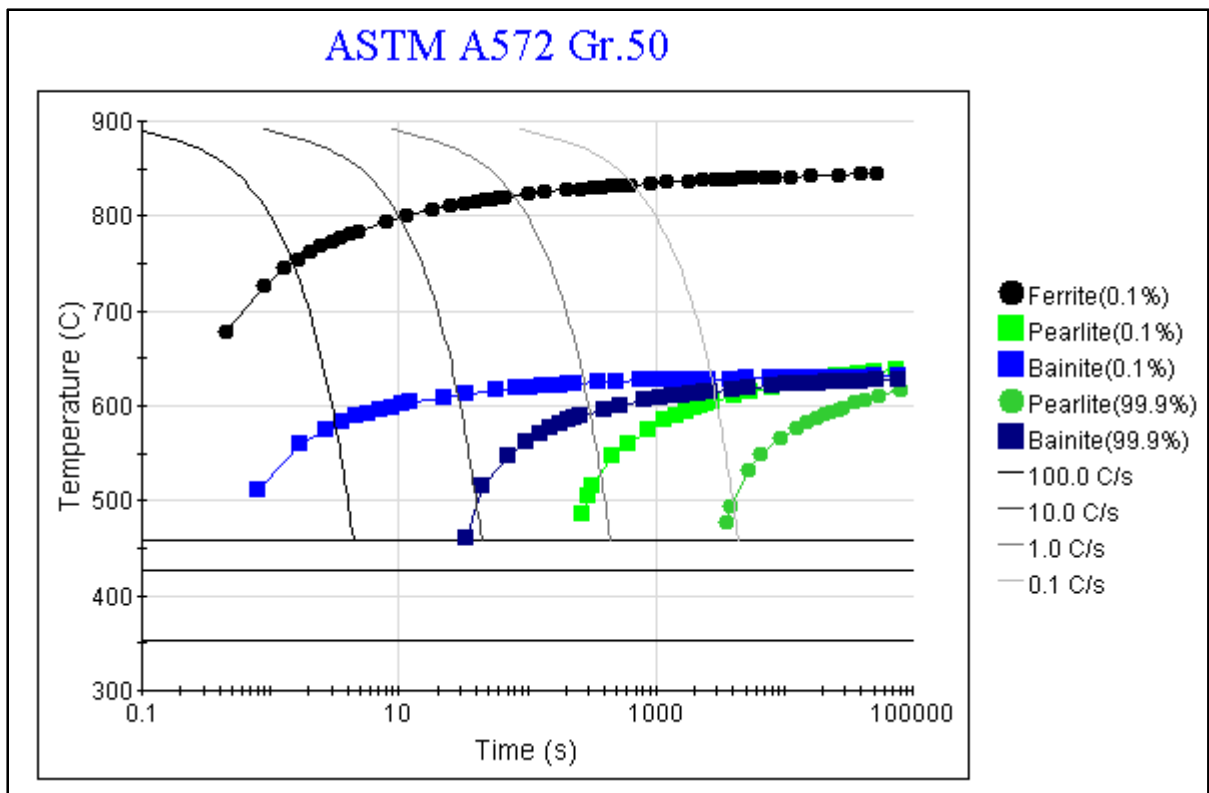


Figure 3.44 CCT diagram calculated for HAZ of Gr.50 welds.

Figure 3.45 shows the evolution of microstructure in the HAZ of a Gr.50 specimen from the weld metal to the base metal. The microstructural evolution is in agreement with those found by Frei et al. for gradual dissolution of pearlitic bands in HAZ for a hot rolled, normalized and tempered steel with equiaxed ferrites and pearlitic bands [57]. The microstructure adjacent to the weld metal consists of a non-equilibrium long needle shape phase. By taking

distance from the weld metal towards the base metal, the length of the needles decreases. The finest needles belong to Figure 3.45d which is correlated to an approximate distance of 280-380 μm from the weld-HAZ boundary. Equilibrium phases gradually appear starting from a distance of 400 μm as illustrated in Figure 3.45e. Pearlitic bands, the same as those found in the base metal, can be clearly observed in Figure 3.45j, k and l.

Hardness line for Gr.50 showed in Figure 3.46, indicates a HAZ width of 1680 μm which can be correlated with the width of microstructural evolution from weld-HAZ boundary to HAZ-base boundary (1580 μm) shown in Figure 3.45. The range of hardness variation within the HAZ of Gr.50 is 117 HV which can be explained by the huge variation of morphology within HAZ. The maximum hardness in HAZ of Gr.50 is 321 HV which corresponds to 360 μm from weld-HAZ boundary. Furthermore, the maximum achieved hardness is correlated with the finest needle morphology in Figure 3.45d (280-380 μm from the weld-HAZ boundary). It can be concluded that the finer are the needles, the higher will be the hardness. Just after the hardness peak, there is a descending trend in HAZ hardness towards the base metal. This can be explained by development of equilibrium phases observed in Figure 3.45e, f and g. Finally, the hardness reaches to the value of those observed in the base metal.

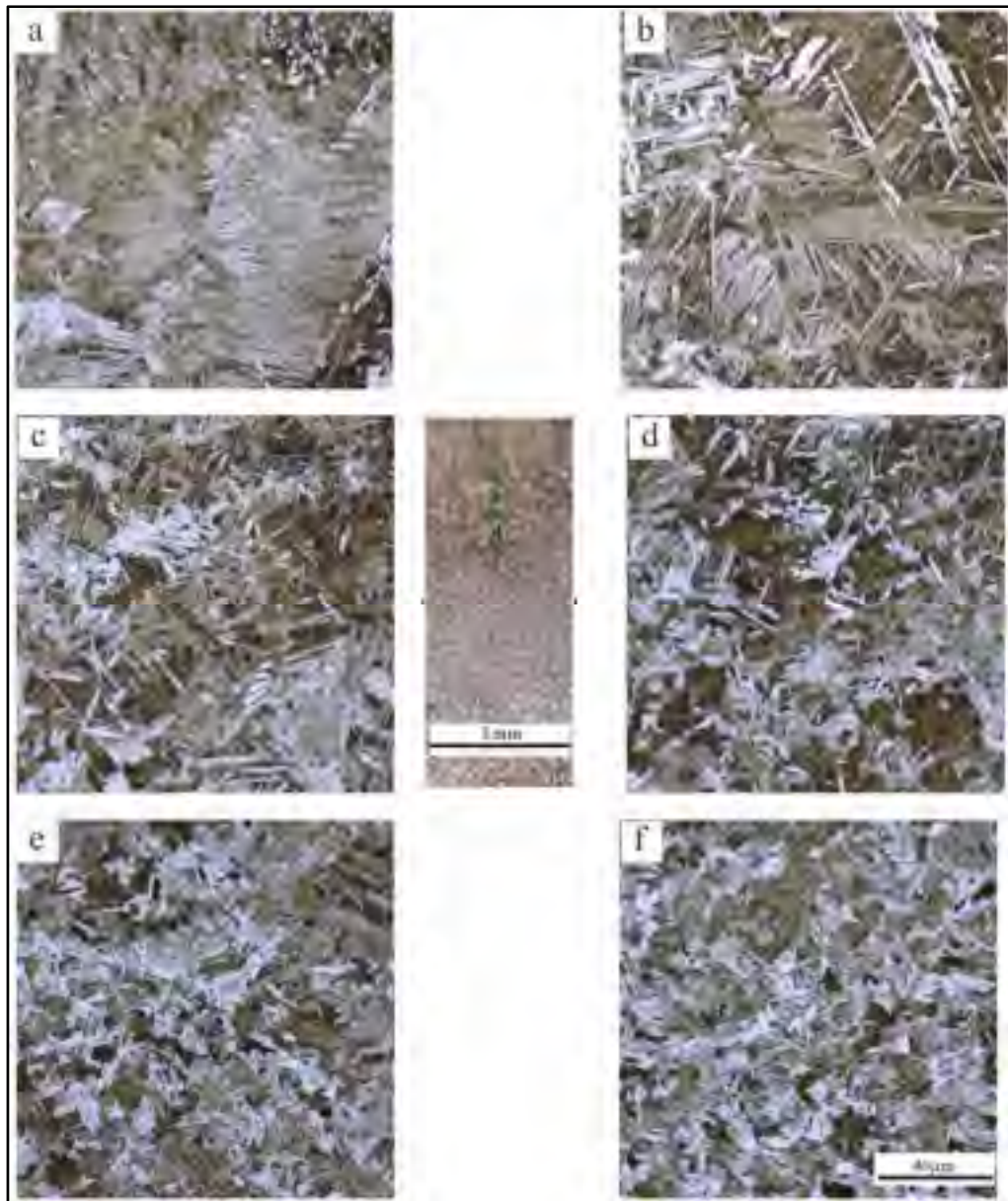


Figure 3.45 Microstructure evolution in HAZ of a Gr.50 weld locations a to f (specimen: 50-4-3, hot etched).locations g to l (specimen: 50-4-3, hot etched).

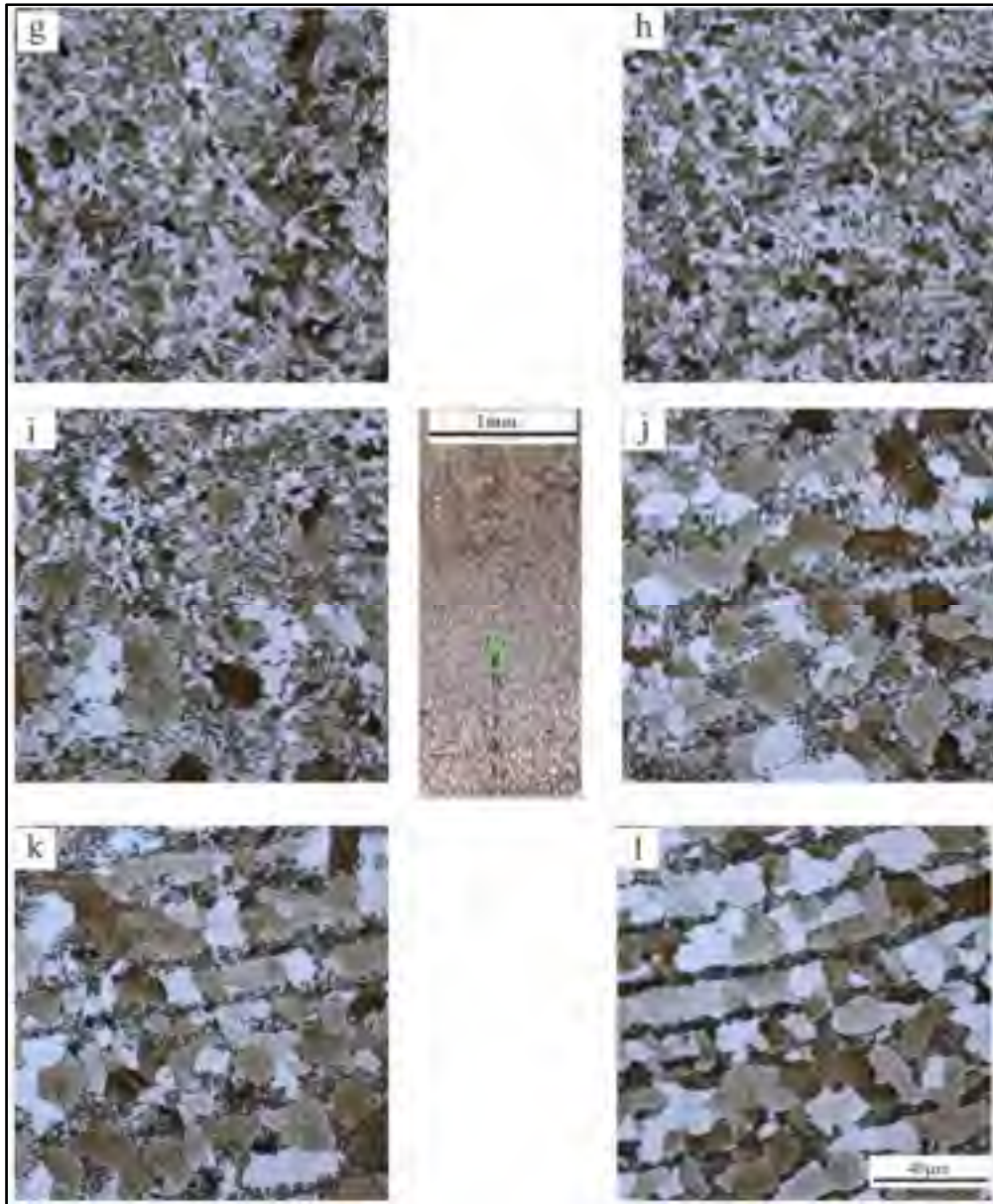


Figure 3.45 Continued (from location g to l)

CCT diagrams calculated for Gr.80 base metal shown in Figure 3.47 which are very similar to the Gr.50 base metal indicate that formation of ferrite and bainite in high cooling rates (100°C/s and 10°C/s), while in lower cooling rates, formation of pearlite is also probable.

Figure 3.48 shows the evolution of microstructure in HAZ of a Gr.80 specimen from the weld metal towards the base metal. The only microstructure observed on Gr.80 HAZ is bainite packets. This is in agreement with the literature as shown in Figures 1.11 and 1.12

[21, 69]. Baitine packets size depends on the size of prior austenite. The higher is the austenitization temperature the coarser will be the size of the packets [21]. Therefore, as shown in Figure 3.49, as the distance from the weld metal increases, the size of packets is reduced. In contrast to the Gr.50, there is no morphology change within HAZ in Gr.80 and the only variation from the weld to the base metal is decrease in the size of packets. This observation can be explained by the initial microstructure of the base metal. Gr.80 base metal consists of non-equilibrium ferrite which keeps its non-equilibrium nature during the thermal cycles in HAZ. Conversely, Gr.50 base metal is mostly consisting of equilibrium ferrite and pearlite which transform to non-equilibrium phases as a result of welding thermal cycles. The average size of the packets varies from 45 μm just adjacent to the weld showed in Figure 3.48a to 3.5 μm shown in Figure 3.48g.

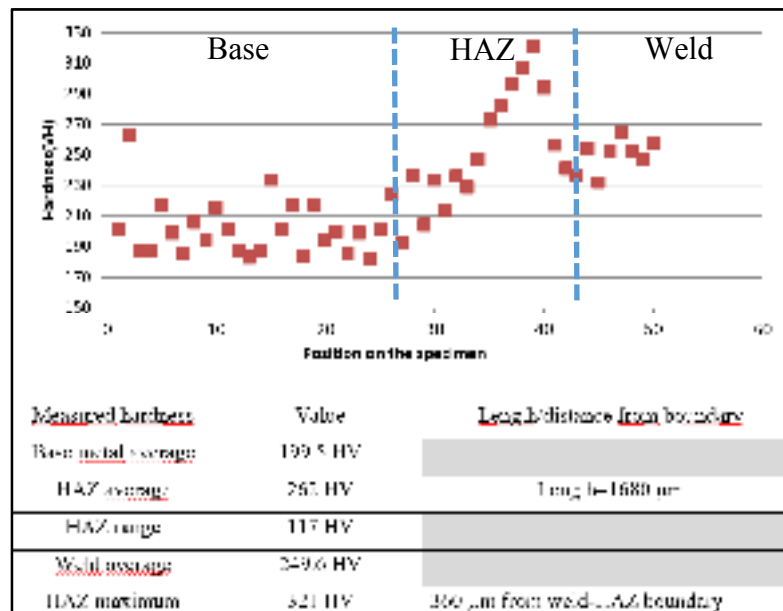


Figure 3.46 Hardness variation from base metal to the weld in Gr.50 (specimen: 50-4-3, hot etched).

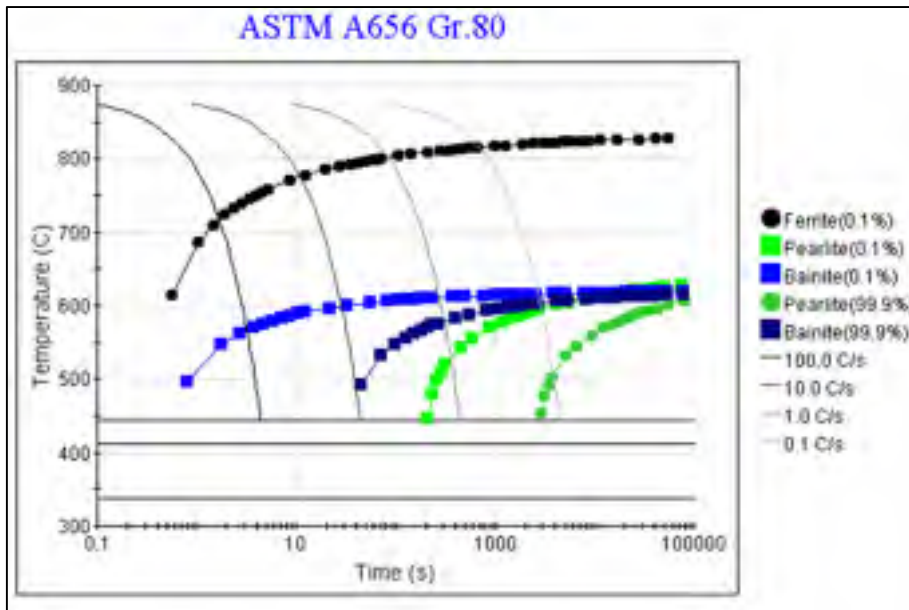


Figure 3.47 CCT diagram calculated for HAZ of Gr.80 welds.

Figure 3.49 shows the evolution of average grain size in HAZ of Gr80 as a function of distance from the weld based on microstructural studies showed in Figure 3.48. Hardness line showed in Figure 3.50, indicates a HAZ width of 720 μm for Gr.80 which is approximately in agreement with the width of microstructural evolution from weld-HAZ boundary to HAZ-base boundary (680 μm). Gr.50 HAZ is 2.3 times wider compared to Gr.80 HAZ. It can be explained by higher thermal conductivity of Gr.50 base metal compared to Gr.80 base metal as illustrated in Figure 3.8. The range of hardness variation within the HAZ is 45 HV which is just 0.38 of the hardness variation in Gr.50 HAZ. This can be explained by no significant morphology variation within Gr.80 HAZ compared to huge variation in Gr.50 HAZ. The maximum hardness in HAZ is 325 HV which corresponds to 360 μm from weld-HAZ boundary which is correlated with Figure 3.48d (280-380 μm from the weld-HAZ boundary). The range of hardness observed in Gr.80 HAZ is in agreement with those reported for hardness of bainite packets in a HSLA steel welded by GMAW (275-375 HV) [21]. Although the hardness of G.80 base metal is higher than Gr.50 base metal, the maximum hardness achieved in HAZ of Gr.50 is almost the same as those achieved in Gr.80 HAZ. This can be attributed to the formation of needle shape phase which harden the HAZ of Gr.50. The

same as Gr.50 HAZ, just after the hardness peak, there is a descending trend in hardness towards the base metal which shows the gradual evolution towards the base metal microstructure as shown in Figure 3.48h. The hardness of weld metal in both Gr.50 and Gr.80 weld metals is higher than HAZ which is in agreement with the literature [14]. On the other hand, as explained in paragraph 3.3.3 the carbon equivalents (CE) calculated for both welds are very close which explains the approximately similar hardness values.

As shown in Figure 3.52, carbonitrides with similar morphologies as those presented in the base metal are detected in HAZ. EDS analysis shown in

Figure 3.51, confirms that carbonitrides in the HAZ remained undissolved during the welding cycles.

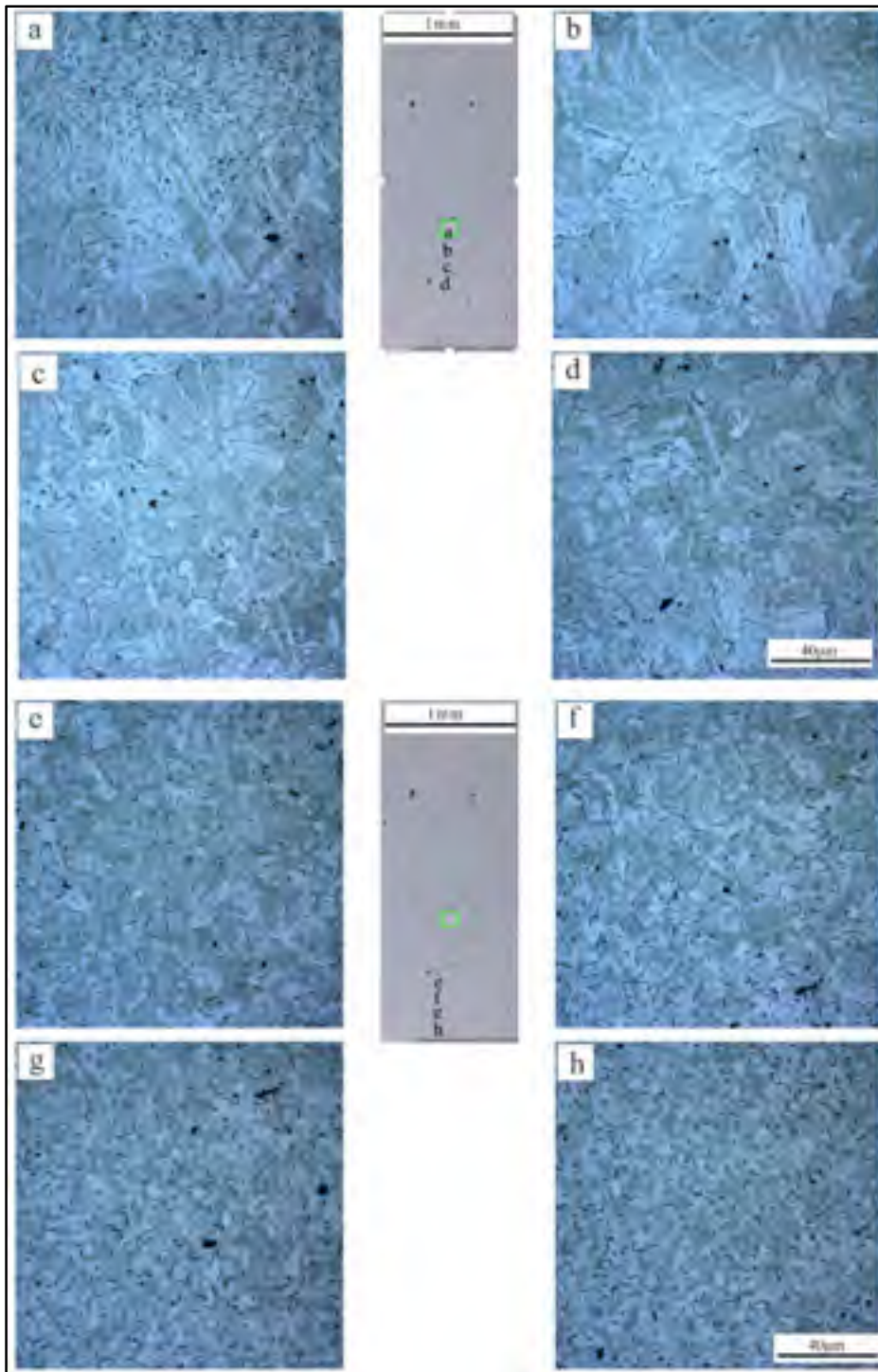


Figure 3.48 Microstructure evolution in HAZ of a Gr.80 weld, from a to d (specimen: 80-4-3, hot etched).

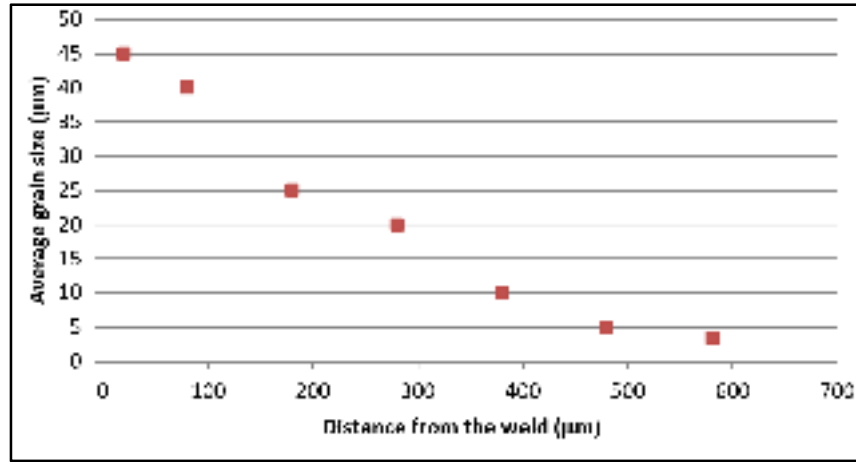


Figure 3.49 Evolution of average grain size in HAZ of Gr80 as a function of distance from the weld (specimen: 80-4-3).

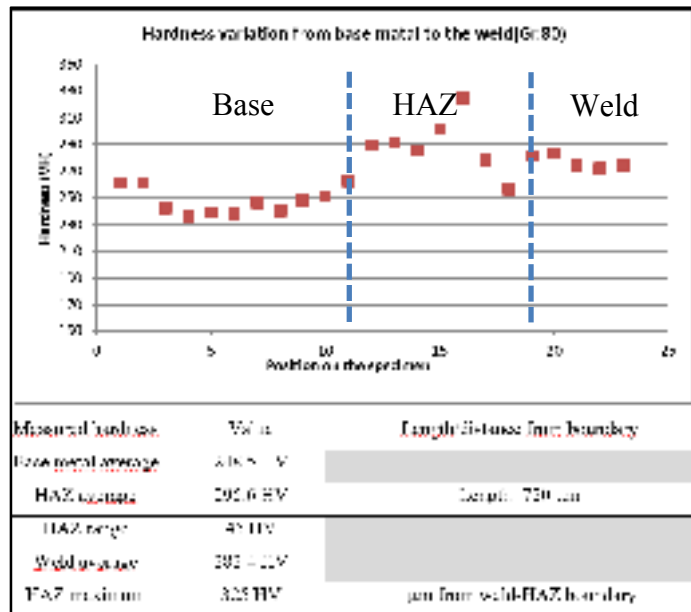


Figure 3.50 Hardness variation from base metal to the weld of Gr.80 (specimen: 80-4-3).

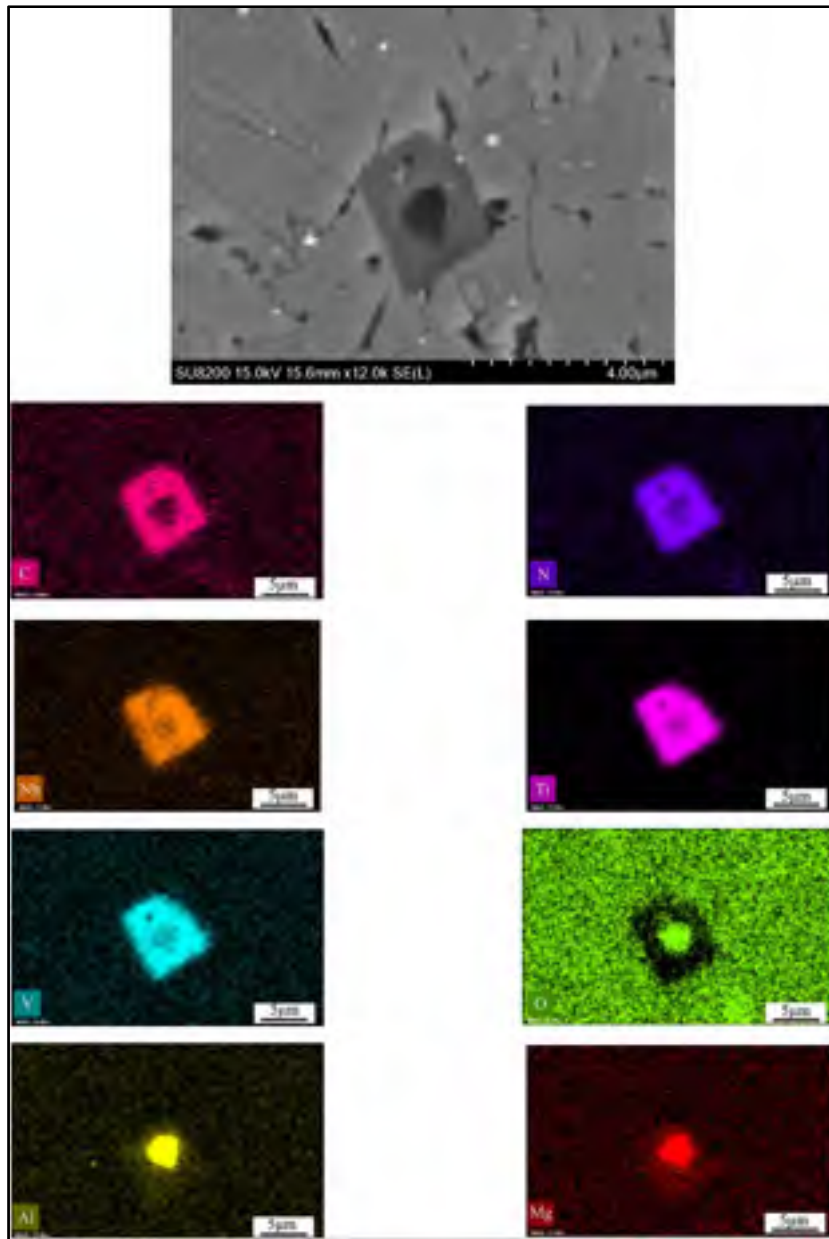


Figure 3.51 EDS analysis on complex carbonitrides of Gr.80 HAZ (specimen: BK2-2, hot etched).

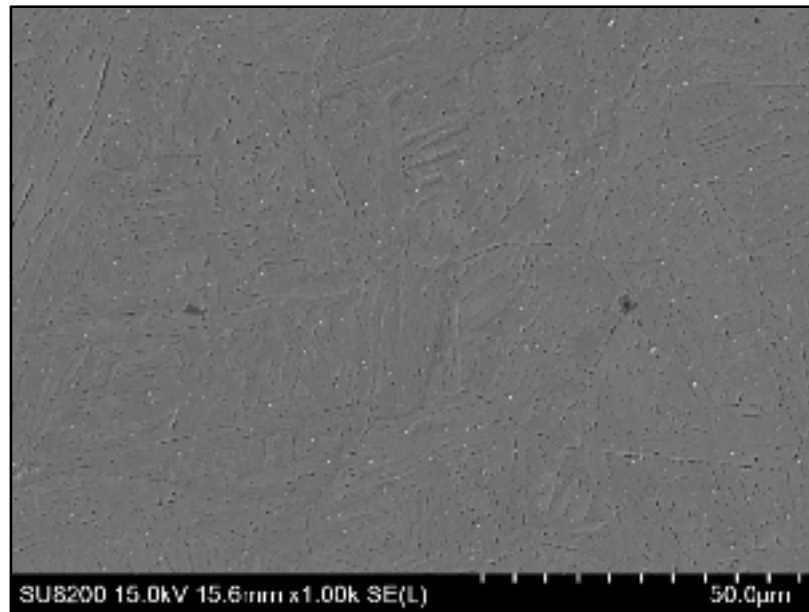


Figure 3.52 Complex carbonitrides distributed in HAZ of Gr.80 (specimen: BK2-2, hot etched).

3.5 Remedies and preventive actions

Hot cracking can appear in both micro and macro in size. It is not necessarily appearing on the weld surface. Equiaxed grains in weld surface can prevent crack propagation to the weld surface and therefore the crack remains invisible and even not detectable with not destructive tests. On the other hand, differentiating between microcrack and the sound meeting point of the solidification front at the centerline of the weld is sometimes impossible. Therefore, it is highly recommended to perform a comprehensive study on weld microstructure in the design phase. It helps to detect any susceptibility to weld defect before industrialization of the weld design.

As mentioned in technological strength theory explained in chapter 1, ϵ_{red} (safety margin) is equal to $P_{min} - (\epsilon_{int} + \epsilon_{ext})$. The nature of safety margin is strain which is described as remained strain that a specific weld can accommodate without cracking. The wider the safety margin is, the lower will be the probability of hot cracking. Accordingly there are two ways to increase the safety margin: 1) increasing the ductility of the weld metal in brittle

temperature range (BTR) which shifts the P(T) curve in Figure 1.27 to the right so the weld metal can accommodate higher deformations or 2) decrease the internal and external strains on the weld metal.

Table 3.8 summarizes the hot cracking root causes concluded from this work, their mechanisms and recommended remedies for each root cause. As discussed before, larger PDAS and therefore longer SDA are found to increase the hot cracking resistance at the centerline of Gr.50 welds. Although the length of PDAS in Gr.50 welds is due to the larger grains of HAZ, but increase in grain size cannot be recommended because of its detrimental effect on mechanical properties of HAZ. In order to increase the probability of formation of SDA, it can be recommended to decrease the ratio of temperature gradient (G) to velocity of solidification front (R) [70]. Preheating of base metal before welding can dramatically decrease the temperature difference between melt and the base metal during solidification and therefore makes an important decrease in G/R ratio. This leads the solidification mode to be changed from cellular to dendritic and therefore increases the probability of formation of SDA; thereby, reducing the susceptibility to centerline cracking.

As shown in Figure 3.4, microstructure of Gr.80 base metal is not fully recrystallized after rolling. Deformed grains contain high residual stresses due to high dislocations density. Although this residual stresses are expected to be completely released during weld thermal cycles in HAZ, but a portion of this residual stress can remain at the zones not affected by heating. Preheating will decrease the residual stresses in the base metal and therefore less stress can be applied on the centreline of the weld from the base metal [71].

Weld penetration is an important factor which increases the resistance of the weld to mechanical stresses. On the other hand, excess penetration leads to increase the sharpness of V-shape narrow area and produce more perpendicular dendrites to the centerline which increases the susceptibility of the weld metal to hot cracking. Excess penetration will also enhance the dilution from the base metal which induces more microsegregations at the centerline of the weld. Optimizing the heat input per unit length (H) by selecting proper

amperage as well as sticking to 45° welding angle is recommended to keep the excessive penetration height in a safe range of 1-2 mm. Using automatic technique is the best solution to keep constant welding angle. However, in some industrial cases automatic welding is not feasible due to the complexity of the welding path. Optimized heat input helps also to reduce the probability of microsegregation at the weld centerline. Using a filler metal with larger diameter can also be recommended due to its positive effect on decreasing the excessive penetration height. Reducing the CO₂ portion in shielding gas can also help to decrease the excessive penetration by lowering the thermal conductivity [24].

Lowering the welding speed can increase the convexity of the weld face and therefore reduce the stress concentration in the weld face [71]. However, the nucleation of hot cracks in the current work does not start from the weld face.

Welding equipment is another factor controlling the quality of the weld. Contamination in shielding gas, lack of sufficient protection, dirt on base metal, extending the wire far from the nozzle can cause gas porosities in weld metal [72]. As shown in Figure 3.31, hot cracking follows the gas porosities and therefore gas porosities increase the intensity of stress on the crack path and ease the crack propagation. Cleaning and using big enough nozzle, having enough gas flow, avoiding leakage (maintenance) and cleaning of nozzle can be recommended as process related remedies. It is recommended to not extend the wire more than ½ inch (12.7 mm) from nozzle. Lowering the welding speed to have more protection can also help avoiding gas porosities [72].

As shown in Table 3.8, the remedies can be classified in two categories: 1) design related remedies which propose fundamental changes in welding design in order to eliminate the risk of hot cracking, and 2) Process related remedies which propose some improvements to mitigate the risk of hot cracking. On this basis a probability-impact matrix for hot cracking has been developed and presented in Table 3.7. This type of matrix is widely used for risk analysis and decision making in industry. As an example Hameed, A et al. has analyzed the risk level of equipment's shutdown considering the criticality of equipment, production loss

and asset damage caused by the shutdown [73]. If weld cracking can lead to a catastrophic consequence during the service life of the part, design related remedies must be applied to eliminate the cracking risk completely. Even extremely rare possibility of hot cracking is not tolerable when the impact is catastrophic. Conversely major impact is when the hot cracking will not end up to a fracture or if ends up to fracture, no catastrophic consequence is expected. The major impact is defined as degradation of the product function when cracking or even fracture happens. When a major risk is present, only a rare possibility is tolerable, but for higher occurrence possibilities the hot cracking risk must be eliminated by design related remedies. Process related remedies are recommended only when the impact is minor or when the impact is major but the occurrence possibility is rare. The process related remedies can also be applied as complementary improvement beside the design related remedies.

Table 3.7 Probability-impact matrix for weld cracking.

Occurrence probability	Impact		
	Minor	Major	Catastrophic
Rare	Process related remedies	Process related remedies	Design related remedies
Moderate	Process related remedies	Design related remedies	Design related remedies
Likely	Process related remedies	Design related remedies	Design related remedies
Very likely	Process related remedies	Design related remedies	Design related remedies
Minor: Crack does not end up to fracture or fracture has minor effect on part functionality. Major: Fracture causes loss of functionality. Catastrophic: Fracture causes a catastrophic consequence.			

As the consequence of weld failure is often catastrophic or major, design validation tests plan including metallographic and mechanical tests must be in place before industrialization of the weld design. This is crucially important as the crack is not always visible on weld surface and also differentiation of cracked and sound centerline is not possible unless by applying metallographic studies.

Table 3.8 Hot cracking root cause analysis. Remedies are categorized in two groups: Design related remedies (D) and Process related remedies (P).

Root cause	Mechanism	Remedy	D	P
Short SDA	-SDA not locked	-Preheat	*	
Residual stress on base metal	-Stress increase in centerline	-Preheat	*	
Perpendicular PDA	-PDA not locked	-Preheat	*	
Excess penetration	-Perpendicular dendrites	-Heat input decrease -Filler metal with bigger diameter -Decreasing CO ₂ portion in shielding gas. -Proper welding angle -automatic welding	*	*
	-Dilution of tramp elements from base metal	-Heat input decrease	*	
Concavity of weld face	-Stress concentration on weld face surface	-Lowering welding speed	*	
Variation in arc and angle	-Variation of stress distribution in weld length	-Automatic welding -Proper welding angle -Pause between welds	*	*
Gas porosity	-Stress intensity at crack path	-Cleaning -Big enough nuzzle -Enough gas flow -Avoid leakage -Avoid excess extension -Low welding speed		*

CONCLUSION

- 1- Gr.80 welds are susceptible to hot cracking. Conversely Gr.50 welds show don't show susceptibility to hot cracking due to wider PDA and therefore longer SDA which are locked together and increase the resistance of the weld centerline to hot cracking.
- 2- Among the Gr.80 weld specimens those with excessive penetration have been cracked. Excessive penetration leads to formation of a perpendicular dendrites area which is susceptible to hot cracking.
- 3- It is recommended to keep the excessive penetration range below 2.5 mm to avoid hot cracking. However, a minimum excessive penetration height of 1mm should be considered to avoid lack of penetration.
- 4- Hot cracking initiates by formation of a void due to contraction of dendrites at V-shaped area simultaneously with the development of dendrites in adjacent zone.
- 5- Equiaxed grains are formed at weld face and make the crack invisible; therefore metallographic studies are recommended before industrializing the weld design.
- 6- Acicular ferrite is the predominant microstructure in weld metal. However, allotriomorphic and Widmanstätten ferrite are also exist. Increase in Ni and Mo content leads to higher volume fraction of acicular ferrite which in turn delays the propagation of Widmanstätten ferrite into the dendrites.

RECOMMENDATIONS

Hot cracking root causes have been analyzed and discussed in the current work alongside with proposed remedies. A comprehensive study has been developed based on metallographic and chemical analysis. However due to the limitations and scope of the current work there are still many investigations to be performed by future researchers.

Measurement of the temperature during the welding can help to correlate the mechanical and microstructural results with experienced temperature. Due to the limitations in current work the measured values of HAZ and weld metal temperature was not available. A study can be performed to explain the mechanical properties and microstructural evolutions by experienced temperature. It can be accompanied by simulated data for weld design and experienced temperature.

The microstructure of Gr.50 HAZ cannot be explained by the existing literature. The evolution of needle shape structure in HAZ need to be more investigated in future studies. Comprehensive studies using electron backscatter diffraction (EBSD) and transmission electron microscopy (TEM) to explain the microstructure of Gr.50 HAZ as well as more investigation on weld metal microstructure and its influence on weld defects is recommended for future studies.

The test plan in this work focused mostly on hot cracking root causes rather than evaluating the effectiveness of remedies. Another test plan can be designed to investigate the level of effectiveness for each proposed remedy such as decreasing CO₂ content in shielding gas mixture and preheating.

A comprehensive activity is recommended to be applied in industry for all the existing welds. It helps to have a clear idea about the resistance of the weld to defects. A risk analysis method like Probability-impact matrix can be applied to analyse the risk of weld defect in each weld design and a specific design validation plan can be developed for each case.

LIST OF BIBLIOGRAPHICAL REFERENCES

- [1] Davis, J.R., *Alloying, Understanding the basics*. 2001: ASM International.
- [2] Committee, A.I.H., *Properties and Selection-- Irons, Steels, and High-performance Alloys*. 10 ed. 2010: ASM International.
- [3] Singh, R., *Applied Welding Engineering: Processes, Codes, and Standards*. 2011: Butterworth-Heinemann.
- [4] Bramfitt, B.L. and A.O. Benscoter, *Metallographer's Guide: Practice and Procedures for Irons and Steels*. 2002: ASM International.
- [5] Davis, J.R., *Alloying: understanding the basics*. 2001: ASM international.
- [6] Committee, A.I.H. and G.F. Vander Voort, *ASM handbook*. Vol. 9. 2004: Asm International Materials Park, OH.
- [7] Russo Spena, P. and D. Firrao, *Thermomechanical warm forging of Ti-V, Ti-Nb, and Ti-B microalloyed medium carbon steels*. *Materials Science and Engineering: A*, 2013. 560: p. 208-215.
- [8] Hong, S.G., K.B. Kang, and C.G. Park, *Strain-induced precipitation of NbC in Nb and Nb-Ti microalloyed HSLA steels*. *Scripta Materialia*, 2002. 46(2): p. 163-168.
- [9] Kou, S., *Welding Metallurgy*. 2003: Wiley.
- [10] Kapoor, M., R. O'Malley, and G.B. Thompson, *Atom Probe Tomography Study of Multi-microalloyed Carbide and Carbo-Nitride Precipitates and the Precipitation Sequence in Nb-Ti HSLA Steels*. *Metallurgical and Materials Transactions A*, 2016. 47(5): p. 1984-1995.

- [11] Ghomashchi, R., W. Costin, and R. Kurji, *Evolution of weld metal microstructure in shielded metal arc welding of X70 HSLA steel with cellulosic electrodes: A case study*. *Materials Characterization*, 2015. 107: p. 317-326.
- [12] Babu, S.S., *The mechanism of acicular ferrite in weld deposits*. *Current Opinion in Solid State and Materials Science*, 2004. 8(3-4): p. 267-278.
- [13] Bose-Filho, W.W., A.L.M. Carvalho, and M. Strangwood, *Effects of alloying elements on the microstructure and inclusion formation in HSLA multipass welds*. *Materials Characterization*, 2007. 58(1): p. 29-39.
- [14] Pamnani, R., et al., *Evaluation of mechanical properties across micro alloyed HSLA steel weld joints using Automated Ball Indentation*. *Materials Science and Engineering: A*, 2016. 651: p. 214-223.
- [15] Zhang, T., et al., *Global progress on welding consumables for HSLA steel*. *ISIJ International*, 2014. 54(7): p. 1472-1484.
- [16] Madariaga, I. and I. Gutiérrez, *Role of the particle matrix interface on the nucleation of acicular ferrite in a medium carbon microalloyed steel*. *Acta Materialia*, 1999. 47(3): p. 951-960.
- [17] Bhole, S.D., et al., *Effect of nickel and molybdenum additions on weld metal toughness in a submerged arc welded HSLA line-pipe steel*. *Journal of Materials Processing Technology*, 2006. 173(1): p. 92-100.
- [18] Kim, S.H., C.Y. Kang, and K.S. Bang, *Weld metal impact toughness of electron beam welded 9% Ni steel*. *Journal of Materials Science*, 2001. 36(5): p. 1197-1200.
- [19] Wang, W. and S. Liu, *Alloying and microstructural management in developing SMAW electrodes for HSLA-100 steel*. *Welding Journal-New York-*, 2002. 81(7): p. 132-S.

- [20] Keehan, E., et al., *Microstructural and mechanical effects of nickel and manganese on high strength steel weld metals*. Trends in Welding Research, 2002: p. 695-700.
- [21] Shome, M., *Effect of heat-input on austenite grain size in the heat-affected zone of HSLA-100 steel*. Materials Science and Engineering: A, 2007. 445: p. 454-460.
- [22] Zhang, L. and T. Kannengiesser, *Austenite grain growth and microstructure control in simulated heat affected zones of microalloyed HSLA steel*. Materials Science and Engineering: A, 2014. 613: p. 326-335.
- [23] Cao, R., et al., *Micromechanism of Decrease of Impact Toughness in Coarse-Grain Heat-Affected Zone of HSLA Steel with Increasing Welding Heat Input*. Metallurgical and Materials Transactions A, 2015. 46(7): p. 2999-3014.
- [24] Groupe-Industry, C., *Welding for design engineers*. 2007, Mississauga: CWB.
- [25] Kou, S., *Solidification and liquation cracking issues in welding*. Jom, 2003. 55(6): p. 37-42.
- [26] Nissley, N., et al., *Development of the strain-to-fracture test for evaluating ductility-dip cracking in austenitic stainless steels and Ni-base alloys*. Welding in the World, 2002. 46(7-8): p. 32-40.
- [27] Kannengiesser, T. and T. Boellinghaus, *Hot cracking tests—an overview of present technologies and applications*. Welding in the World, 2014. 58(3): p. 397-421.
- [28] Stelling, K., et al., *Hot Cracks as Stress Corrosion Cracking Initiation Sites in Laser Welded Corrosion Resistant Alloys*, in *Hot Cracking Phenomena in Welds*. 2005, Springer. p. 165-182.
- [29] Kou, S., *A criterion for cracking during solidification*. Acta Materialia, 2015. 88: p. 366-374.

- [30] Leggatt, R.H., *Residual stresses in welded structures*. International Journal of Pressure Vessels and Piping, 2008. 85(3): p. 144-151.
- [31] Teng, T.-L., et al., *Analysis of residual stresses and distortions in T-joint fillet welds*. International Journal of Pressure Vessels and Piping, 2001. 78(8): p. 523-538.
- [32] Lippold, J.C., *Welding Metallurgy and Weldability*. 2014: Wiley.
- [33] Sarma, D.S., A.V. Karasev, and P.G. Jönsson, *On the role of non-metallic inclusions in the nucleation of acicular ferrite in steels*. ISIJ International, 2009. 49(7): p. 1063-1074.
- [34] Saida, K., et al., *Influences of phosphorus and sulphur on ductility dip cracking susceptibility in multipass weld metal of alloy 690*. Science and Technology of Welding and Joining, 2012. 17(1): p. 1-8.
- [35] Wolf, M., H. Schobbert, and T. Böllinghaus, *Influence of the weld pool geometry on solidification crack formation, in Hot Cracking Phenomena in Welds*. 2005, Springer. p. 245-268.
- [36] Melford, D., *Surface hot shortness in mild steel-study of influence of residual elements with aid of electron probe microanalyser*. Journal of the Iron and Steel Institute, 1962. 200(APR): p. 290-&.
- [37] Herman, J. and V. Leroy, *Influence of residual elements on steel processing and mechanical properties*. Iron & steelmaker, 1996. 23(12): p. 35-43.
- [38] Krishna Murthy, N. and G.D. Janaki Ram, *Hot cracking behavior of carbide-free bainitic weld metals*. Materials & Design, 2016. 92: p. 88-94.
- [39] Branza, T., et al., *Study and prevention of cracking during weld-repair of heat-resistant cast steels*. Journal of Materials Processing Technology, 2009. 209(1): p. 536-547.

- [40] David, S., et al., *Effect of rapid solidification on stainless steel weld metal microstructures and its implications on the Schaeffler diagram*. 1987, Oak Ridge National Lab., TN (USA).
- [41] Estes, C.L.T., P.W. , *dilution in multipass welding aisi 4130 to type 304 stainless steel* Welding J. (N.Y.), 1964. 43.
- [42] Melfi, T., *New code requirements for calculating heat input*. welding Journal, 2010. 6.
- [43] DuPont, J. and A. Marder, *Thermal efficiency of arc welding processes*. Welding Journal-Including Welding Research Supplement, 1995. 74(12): p. 406s.
- [44] Gucwa, M. and R. Bęczkowski, *The effect of heat input on the geometric properties of welded joints*. Archives of Foundry Engineering, 2014. 14.
- [45] Zondi, M.C., *Factors that affect welding-induced residual stress and distortions in pressure vessel steels and their mitigation techniques: a review*. Journal of Pressure Vessel Technology, 2014. 136(4): p. 040801.
- [46] Lan, L., et al., *Influence of microstructural aspects on impact toughness of multi-pass submerged arc welded HSLA steel joints*. Materials & Design, 2016. 90: p. 488-498.
- [47] Liu, W., et al., *Hybrid laser-arc welding of advanced high-strength steel*. Journal of Materials Processing Technology, 2014. 214(12): p. 2823-2833.
- [48] Yang, Z.B., et al., *Double-sided laser beam welded T-joints for aluminum aircraft fuselage panels: Process, microstructure, and mechanical properties*. Materials & Design, 2012. 33: p. 652-658.
- [49] Miller, D.K. and R. Funderburk. *Reviewing and Approving Welding Procedure Specifications*. in *The National Steel Construction Conference Proceedings*. New Orleans, AISC. 1998.

- [50] Alipooramirabad, H., et al., *Residual stress-microstructure-mechanical property interrelationships in multipass HSLA steel welds*. Journal of Materials Processing Technology, 2016. 231: p. 456-467.
- [51] Prokhorov, N. and N.N. Prokhorov, *Fundamentals of the Theory for Technological Strength of Metals while Crystallising During Welding*. Transactions of the Japan Welding Society, 1971. 2(2): p. 205-213.
- [52] Rappaz, M., J.-M. Drezet, and M. Gremaud, *A new hot-tearing criterion*. Metallurgical and materials transactions A, 1999. 30(2): p. 449-455.
- [53] Totten, G.E., *Steel heat treatment: metallurgy and technologies*. 2006: crc Press.
- [54] Talaş, Ş., *The assessment of carbon equivalent formulas in predicting the properties of steel weld metals*. Materials & Design (1980-2015), 2010. 31(5): p. 2649-2653.
- [55] Kou, S. and Y. Le, *Alternating grain orientation and weld solidification cracking*. Metallurgical Transactions A, 1985. 16(10): p. 1887-1896.
- [56] *ASTM A656/A656M-13 Standard Specification for Hot-Rolled Structural Steel, High-Strength Low-Alloy Plate with Improved Formability*. 2012. p. 2.
- [57] Frei, J., B.T. Alexandrov, and M. Rethmeier, *Low heat input gas metal arc welding for dissimilar metal weld overlays part I: the heat-affected zone*. Welding in the World, 2016. 60(3): p. 459-473.
- [58] Kluken, A. and Ø. Grong, *Mechanisms of inclusion formation in Al– Ti– Si– Mn deoxidized steel weld metals*. Metallurgical Transactions A, 1989. 20(8): p. 1335-1349.
- [59] Ricks, R., P. Howell, and G. Barritte, *The nature of acicular ferrite in HSLA steel weld metals*. Journal of Materials Science, 1982. 17(3): p. 732-740.

- [60] Mills, A., G. Thewlis, and J. Whiteman, *Nature of inclusions in steel weld metals and their influence on formation of acicular ferrite*. Materials Science and Technology, 1987. 3(12): p. 1051-1061.
- [61] You, D., et al., *Modeling of inclusion formation during the solidification of steel*. ISIJ International, 2016. 56(10): p. 1770-1778.
- [62] Wawszczak, R., et al., *Evolution of microstructure and residual stress during annealing of austenitic and ferritic steels*. Materials Characterization, 2016. 112: p. 238-251.
- [63] Peet, M., H. Hasan, and H. Bhadeshia, *Prediction of thermal conductivity of steel*. International Journal of Heat and Mass Transfer, 2011. 54(11): p. 2602-2608.
- [64] Karadeniz, E., U. Ozsarac, and C. Yildiz, *The effect of process parameters on penetration in gas metal arc welding processes*. Materials & design, 2007. 28(2): p. 649-656.
- [65] Reardon, A.C., *Metallurgy for the Non-metallurgist*. 2011: ASM International.
- [66] Rajamäki, P., *Fusion weld metal solidification: continuum from weld interface to centerline*. 2008: Lappeenranta University of Technology.
- [67] Di, X., S. Deng, and B. Wang, *Effect of pulse current on mechanical properties and dendritic morphology of modified medium manganese steel welds metal*. Materials & Design (1980-2015), 2015. 66, Part A: p. 169-175.
- [68] Tavares, S.S.M., et al., *Study of cracks in the weld metal joint of p91 steel of a superheater steam pipe*. Engineering Failure Analysis, 2015. 56: p. 464-473.
- [69] Cao, R., et al., *Micromechanism of decrease of impact toughness in coarse-Grain heat-affected zone of HSLA steel with increasing welding heat input*. Metallurgical and Materials Transactions A, 2015. 46(7): p. 2999-3014.

- [70] W. Kurz, D.J.F., *Fundamentals of solidification*. 4th rev. ed. ed. 1998, Uetikon-Zuerich, Switzerland Trans Tech Publications LTD. 305.
- [71] Foundation, T.J.F.L.A.W., *Weld cracking* An Excerpt from the fabricators and Erectors, Guide to welded steel constructions.
- [72] Lubieniecki, V., *Causes and cures for GMAW flaws*. *Welding Journal*, 2011. 90(7): p. 34-36.
- [73] Hameed, A., F. Khan, and S. Ahmed, *A risk-based shutdown inspection and maintenance interval estimation considering human error*. *Process Safety and Environmental Protection*, 2016. 100: p. 9-21.